CHEMOTAXIS IN MARINE BACTERIUM *VIBRIO ALGINOLYTICUS*

by

Li Xie

B.S. in Physics, Beijing Normal University, 2006

Submitted to the Graduate Faculty of

the Kenneth P. Dietrich School of Arts and Sciences in partial

fulfillment

of the requirements for the degree of

Doctor of Philosophy

University of Pittsburgh

2014

UNIVERSITY OF PITTSBURGH

KENNETH P. DIETRICH SCHOOL OF ARTS AND SCIENCES

This dissertation was presented

by

Li Xie

It was defended on

April 16th 2014

and approved by

Xial-Lun Wu, Department of Physics and Astronomy

Hanna Salman, Department of Physics and Astronomy

Walter I. Goldburg, Department of Physics and Astronomy

Daniel Boyanovsky, Department of Physics and Astronomy

Giovanni P. Galdi, Department of Mechanical Engineering and Materials Science

Dissertation Director: Xial-Lun Wu, Department of Physics and Astronomy

CHEMOTAXIS IN MARINE BACTERIUM *VIBRIO ALGINOLYTICUS*

Li Xie, PhD

University of Pittsburgh, 2014

We investigated the motility pattern and chemotaxis system of the polarly flagellated marine bacterium *Vibrio alginolyticus*. *V. alginolyticus* executes 3-step (run-reverse-flick) cycles which are distinctively different from the 2-step (run-tumble) pattern of *Escherichia coli*. This marine bacterium backtracks its forward swimming path and randomizes its moving direction by flicking its flagellum at the end of the backward swimming interval. *V. alginolyticus* has a similar chemotaxis system as *E. coli*, and our study showed that their chemotaxis networks respond to chemical cues in the same manner. However, at contrast to *E. coli*, in which the motor bias is regulate by the chemotaxis network, in *V. alginolyticus*, the switching rates of the flagellar motor is modulated so that swimming intervals in a favorable direction can be lengthened regardless of the motor rotation direction. As a result, despite their different motility patterns, both *E. coli* and *V. alginolyticus* use a biased random walk to migrate toward a nutrient source. To understand the effect of motility patterns on chemotaxis capacity, master equations similar to convection-diffusion equations were developed to describe the motion of these two bacteria in a chemical profile. It was found that by adopting the run-reverse-flick motility pattern, a 3-step swimmer has the same drift velocity but its diffusivity is reduced by half compared to a 2-step swimmer. As a result of the smaller diffusivity, the former localizes better around a nutrient source but does not explore as efficiently as the latter. We thus speculate that the 3-step motility pattern suits better for the marine environment where searching is unproductive and it is more important to exploit an existing, though transient, resource.

TABLE OF CONTENTS

LIST OF TABLES

LIST OF FIGURES

1.0 INTRODUCTION

Foraging is essential for the survival of almost all species when the supply of food is limited. In general, it involves sensing and locating a target, approaching it tactically, and finally taking advantage of it. Different organisms perform foraging in different ways depending on their physiology and environments. This thesis deals with chemotaxis, the foraging behavior of motile bacteria where they sense and taxis towards life-dependent nutrients. Due to their imperceptible size, chemotaxis in these microorganisms was not investigated until late 19th century by W.F. Pfeffer. This field was revitalized by J. Adler [1] in the middle of 1960s and subsequently advanced significantly by many researchers [32, 49, 14, 43, 75].

Chemotaxis enables bacteria to navigate through an environment to search for chemoattractant, such as nutrient, and avoid chemorepellent, such as harmful substance. For more than half a century, many scientists tried to understand how different bacteria carry out chemotaxis [71]. Among them the most studied microorganism is the enteric bacterium *Escherichia coli (E. coli)*, which has a typical size of 1-2 μm and has multiple flagella extending uniformly from its cell body, as seen in Figure 1(A) [26]. Its chemotaxis was first measured quantitatively in Ref. [2]. In short, a capillary tube containing solution of a certain chemical was pushed into a suspension of bacteria on a slide and incubated as illustrated in Figure 1(B). The tube creates a chemical gradient around its mouth and due to its relatively large size (about 25 μm in diameter) compare to that of *E. coli*, the bacteria can accumulate inside. If the chemical is a chemoattractant, such as aspartate, the bacteria are attracted to the opening of the tube forming a swarm around it as in Figure 1(C). After 1 hour, the tube is withdrawn and bacteria are flushed out of the tube and their number counted. If the count is higher than the background, i.e., the number of bacteria in the tube when the tube contains only the medium used to suspend the bacteria, the chemical is an attractant,

otherwise it is a repellent [76]. This assay also allows the sensitivity of bacteria to various chemicals at different concentrations to be quantified, simply by comparing the counts obtained using different chemical solutions.

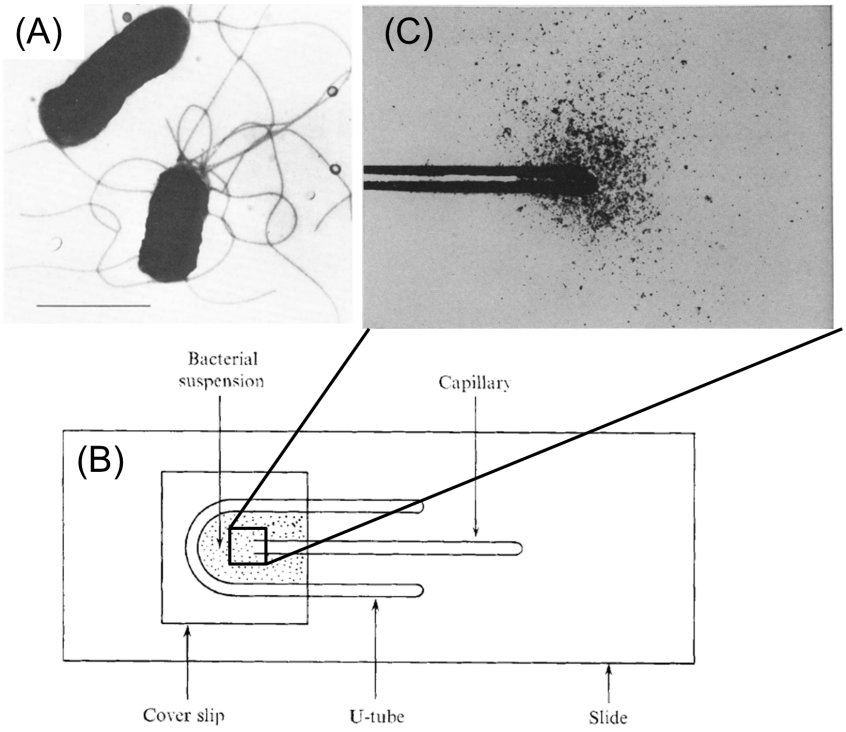

Figure 1: (A) Electron micrograph of intact cells of *E . coli* K12 strain RP487. The bar represents 1.0 μm. (B) Apparatus used in Adler's chemotaxis assay. The drawing is to scale except that the width of the capillary is exaggerated. (C) Photomicrograph showing attraction of *E. coli* bacteria to aspartate close to the tip of the capillary. The capillary tube (diamete ˜25 microns) contained aspartate at a concentration of 2×10^{-3} M. [Photomicrograph by Scott W. Ramsey; dark-field photography]. (A) is taken from Figure 2(A) of Ref. [26], (B) is taken from Figure 1 of Ref. [3], and (C) is taken from Figure 1 of Ref. [2].

1.1 CHEMOTAXIS SYSTEM OF *E. COLI*

1.1.1 The motility pattern of *E. coli*

To understand the mechanism underlying the observed chemotaxis behavior of *E. coli*, the first question is how does it generate motility. For bacteria living in aqueous environments, their motions are governed by hydrodynamics or the Navier-Stokes equation. A bacterium is usually a few microns in length l, and swims around $v \simeq 10 - 100$ μm/s. Water has a density ρ about 1 g/cm^3 and a shear viscosity $\eta \sim 10^{-2}$ g/cm·s. The dimensionless Reynolds number, which indicates the relative importance of inertia over viscous force for an object moving in a fluid, is $Re = lv\rho/\eta \sim 10^{-4}$ for a bacterium, while for a macroscopic animal, e.g. a scallop, whose $l \sim 10$ cm and $v \sim 10$ cm/s, $Re \sim 10^4$. Consequently, the same hydrodynamic equation that governs the motion of all objects in fluid takes very different forms when applied to a bacterium and a scallop. A scallop swims by slowly opening its shell then rapidly closing it. Since the large $Re \sim 10^4$ dictates that the inertia plays a much significant role in its motion, the scallop can coast after it closes the shell, thus generating motility. However, if the scallop shrinks down to a size comparable to that of a bacterium, its open-close scheme cannot get it anywhere since the low $Re \sim 10^{-4}$ prohibits it from coasting and it simply returns to its initial position after it opens and closes the shell. This phenomenon, named by E. Purcell as the "Scallop Theorem" [58], states that if a microscopic organism deforms its body in a reciprocal manner, like a scallop does by distorting its body in one way then reversing this distortion, it remains in the same place. E. Purcell noted that on the other hand a microorganism can move by deforming its body in a cyclic manner. To generate a cyclic motion, a lot of microorganisms have appendages such as cilia and helical flagella extending from their cell body. By undulating the cilia, a sperm can thrust itself. By rotating a flagellum, a bacterium can be either pushed or pulled through the fluid. *E. coli* has 3-5 left-handed lateral flagella which are ˜3-9 μm in length growing out from its body, as seen in Figure 1(A) [26]. Each flagellum is rotated by a molecular motor, either in counter-clockwise (CCW) or clockwise (CW) direction [13, 66]. The molecular motor is about 50 nm in diameter and very similar to an electric motor, consisting of a rotor and stators. When all

flagella rotate CCW, the left-handed flagella form a bundle, pushing the cell body forward. When one or more flagella rotates CW, the bundle flies apart and the cell moves erratically. When all the flagella rotate CCW again, the bundle re-forms and the motion resumes in a new random direction [47]. *E. coli* swimming, first discovered and characterized in 1972 using a tracking microscope [14], is therefore characterized by a run-tumble pattern, which is a cyclic 2-step process.

1.1.2 The chemotactic response of *E. coli*

The next phase of chemotaxis research tried to uncover how *E. coli* regulates its motion and its response to different chemicals. In the experiment by Larsen et al. [43], the cell is tethered to a cover slip at its hook, which is the flexible joint between the flagellum and the motor. The rotating state of the motor can thus be inferred from the rotation direction of the cell body. It was found that when an attractant is applied to the cell, the motor rotates CCW; if a repellent is applied, the motor rotates CW. It is then concluded that the response of the cell to chemical stimuli is manifested in modulating the rotating direction of the motor. When the response was quantitatively measured in Ref. [14, 75], it was found that when the cell is moving up an attractant gradient or moving down a repellent gradient, it suppresses CW rotation of the flagella so that the run is lengthened. When the cell descends a sharp attractant gradient, the cell tumbles more frequently and the run intervals are shortened. Thus *E. coli* carries out chemotaxis by executing a biased random walk so that the motion toward a favorable direction is enhanced and that toward an unfavorable direction is repressed.

This response is similar to the sensory reception in higher species albeit a bacterium can only sense the environment at its immediate proximity. However, bacteria were able to discern if they are going up or down a chemical gradient. For a moving instrument to measure the gradient of a field, say a chemical concentration profile $c(x)$, there are two common ways. One is spatial comparison by computing the instantaneous spatial gradient $\partial c(x)/\partial x$, the other is temporal comparison by computing the total time derivative of $c(x(t))$ in the moving frame of the instrument, $dc(x(t))/dt = v\frac{\partial c(x)}{\partial x}$, where v is the speed of the instrument. For a

bacterium to obtain the instantaneous $\partial c(x)/\partial x$, it can compare the chemical concentrations measured at one end of the cell poles to the other. Experiments showed that in a linear serine profile where $|\partial c/\partial x|/c_0 = 1/20$ mm^{-1}, the cells at $c_0 = 1$ μM can respond by migrating up the gradient [49]. In this case, the chemical concentration difference measured at c_0 by spatial comparison is $l|\partial c/\partial x| \sim 10^{-4}$ μM, if the cell length l is taken to be 2 μm. On the other hand, assuming the instrument measures c_0 by counting the number of molecules within its cell volume l^3, the uncertainty of this counting is $\sqrt{c_0/l^3} \sim 10^{-2}$ μM. In this back-of-envelope estimation, the signal-to-noise ratio in computing $\partial c(x)/\partial x$ is only ~ 0.01, indicating that spatial comparison is not reliable in detecting the chemical gradient for such a small organism and temporal comparison should be a better strategy. In this case, the cell computes $[c(x(t_2))-c(x(t_1))]/(t_2-t_1)$, where $t_2 > t_1$ and if this quantity is positive, it is going up the gradient. To distinguish between these two scenarios, R. Macnab et al. carried out an experiment in which bacteria are subjected to a sudden elevation in attractant concentration, while the attractant profiles are kept uniform [49]. If bacteria employ instantaneous spatial sensing they would not respond since they are still in a uniform chemical profile, whereas if they utilize the temporal sensing, they would respond as if they are in a gradient by extending their run lengths. The results confirmed the latter hypothesis that bacteria employ temporal sensing because after the elevation in attractant concentration the run intervals are remarkably increased. At any instant the cell senses only a single value inferred from the chemical profile, compares this value with that obtained earlier. If the comparison indicates that it is moving up an attractant gradient, tumbling is suppressed so that the bacterium is able to migrate toward regions with higher attractant concentration through the biased random walk.

1.1.3 The chemotaxis sensory network of *E. coli*

Around the same time when the chemotaxis response was characterized, biologists also started to investigate the molecular events that relays the chemical cues to the flagellum regulation. First, it was demonstrated in Ref. [2] that the chemotactic response of *E. coli* to galactose, which is a sugar, does not depend on whether or not galactose is transported into

the cell or metabolized, indicating that the chemotactic behavior is generated by recognizing the chemical itself. Later, chemoreceptors, which recognize and bind specific chemicals, were indeed identified [32]. However, these receptors were not clustered around the flagellar basal ends or the motors, suggesting that the signal is not transmitted via physical contact but mediated by other components [27]. Subsequent research on signal transduction systems over decades established the chemotaxis network as the paradigm of signaling pathways, known as the two-component regulatory system, that are ubiquitous in all kingdoms of biology. The chemotaxis system of *E. coli* comprises a chemosensing system that detects external chemical cues, a chemotaxis network that relays the information from the receptors to the flagellar motor, and a motor complex that converts this information into regulation of the frequency of tumbling. In the system, signal is transmitted via protein-protein interactions, which will be further discussed in Chapter 4. A receptor can assume two conformations, active and inactive. Once bound by an attractant molecule, the receptor becomes inactive and the change in its activity propagates through the chemotaxis network, resulting in a change in the concentration of the messenger protein CheY-P, which is the active form of the chemotaxis protein CheY. CheY-P interact with the motor and induces CW rotation, thus a change in CheY-P concentration regulates the flagellum rotation and modulates the run length of the cell. Working coherently, these three modules enable the bacterium to carry out chemotaxis efficiently to maximize its nutrient uptake from the environment.

Over the last half a century *E. coli*'s chemotaxis system has been characterized extensively [17]. The accumulated experimental data on details of biochemical interactions among proteins spawned numerous mathematical modelings that describe the system quantitatively, which in turn revealed many novel properties of the chemotaxis system. It was found that on one hand, this bacterium is very sensitive to chemical stimuli because of the cooperativity among its chemoreceptors [16], and on the other hand, it can adapt to a wide range of chemical concentrations robustly thus has a large dynamic range [9]. Controlled by the chemotaxis system, the bacterial chemotaxis strategy optimizes the cell's ability to migrate up an attractant gradient as well as to localize around it's source [64]. These insights can also be applied to other signal pathways, greatly enhancing our understanding on various biochemical systems.

1.2 CHEMOTAXIS IN OTHER BACTERIA

Bacteria make up more than half of the biomass of the earth ecology system [79]. They have all different kinds of morphologies, metabolic requirements, and use their own unique niches to prosper. In terms of how they carry out chemotaxis, although mechanisms involved in *E. coli*'s chemotaxis system are applicable, different microorganisms have their distinct chemotaxis systems optimized to suit their habitats. This topic, although scarcely studied, has important academic implications as well as potential practical applications. Understandings and insights to this topic could shed light on topics like protein evolution, system biology, micro ecology and more [71]. With the knowledge gained from these fundamental researches, novel technologies could be developed to improve human life greatly. For example, as an alternative to antibiotics, new techniques targeting at inhibiting bacterial chemotaxis can be developed to treat disease caused by bacteria, since it is known that chemotaxis is closely related to the process through which pathogens infect the host [78]. Also for bioremediation, which is the practice of using bacteria to remove the pollutants and toxins from the environment, understanding how these bacteria carry out chemotaxis can greatly enhance their performance [52], especially in projects that deal with polluted underground water system where it is essential that the bacteria can locate the pollutant quickly to destroy them.

So far, genome sequences of a lot of bacteria are available and comparative analysis shows that different bacteria seem to share the core components of *E. coli*'s chemotaxis genes. While it is obvious that they cannot have chemotaxis networks identical to that of *E. coli*'s, it is not clear how different bacteria adapt a similar protein network to control very different motility devices and to optimize their performance in different habitats. For example, in contrast to *E. coli*, which has multiple flagella, a large class of bacteria possess a single polar flagellum driven by a flagellar motor that rotates either in CCW or CW direction. Marine bacterium *Vibrio alginolyticus* (*V. alginolyticus*), which is the subject of this study, is a member of this class. While *E. coli* is capable of randomizing its swimming direction by rotating one or more of its flagella in CW direction, this is not the case for *V. alginolyticus*. When a single polar flagellum alternates between CCW and CW rotations, this motion is reciprocal; the low *Re* hydrodynamics dictates that when *V. alginolyticus*

reverses the rotation direction of its flagellum, it simply backtracks its previous trajectory. Thus it was thought that *V. alginolyticus* cannot perform chemotaxis efficiently because they cannot randomize their swimming direction actively, which is required for searching and chemotaxis. However, when a micropipette filled with 0.5 mM attractant serine is introduced into *V. alginolyticus* culture, similar to that shown in Figure 1(B, C), the bacteria are able to form a very tight cluster around the tip 2 minutes after the insertion of the micropipette, as shown in Figure 2(A), which is much tighter compared to that formed by *E. coli* under the same condition after 6 minutes, as shown by Figure 2(B). This indicates that contrary to the previous perception, *V. alginolyticus* can perform chemotaxis quite efficiently. It must have a unique tactic to randomize its swimming direction as well as a compatible chemotaxis network to accommodate its motility pattern. Quantitative studies on these interesting issues form the body of this thesis.

There are several reasons to choose *V. alginolyticus* as the model organism for studying bacterial chemotaxis. To carry out efficient chemotaxis, active searching is crucial. The motility patterns of bacteria are constrained by low *Re* hydrodynamics and the patterns of flagellation on the cell body. In order to be competitive, bacteria need to have different strategies that are compatible with their motility patterns. Thus to understand chemotaxis in bacteria with a single polar flagellum, *V. alginolyticus* is a more relevant model than *E. coli*. Also, microhabitats in ocean and in animal guts are drastically different, and marine bacteria face challenges that are not present for enteric bacteria. The scheme used by *V. alginolyticus* to execute chemotaxis might very well be employed by other marine microorganisms because they all have to survive in a turbulent environment where nutrient are scarce and transient due to constant dispersion.

Using *E. coli*'s chemotaxis system as a guidance, different aspects of chemotaxis in marine bacterium *V. alginolyticus* are studied quantitatively in this thesis. First, we investigated the motility pattern of *V. alginolyticus*, particularly on how it actively changes its swimming direction. Next, we observed its trajectories in a chemical profile created by a point source of nutrient as shown in Figure 2(A) to understand their chemotaxis response, i.e., their behaviors when going up and down the gradient. Comparing the chemotaxis responses between *V. alginolyticus* and *E. coli*, we realized that their flagellar motors must be regulated by

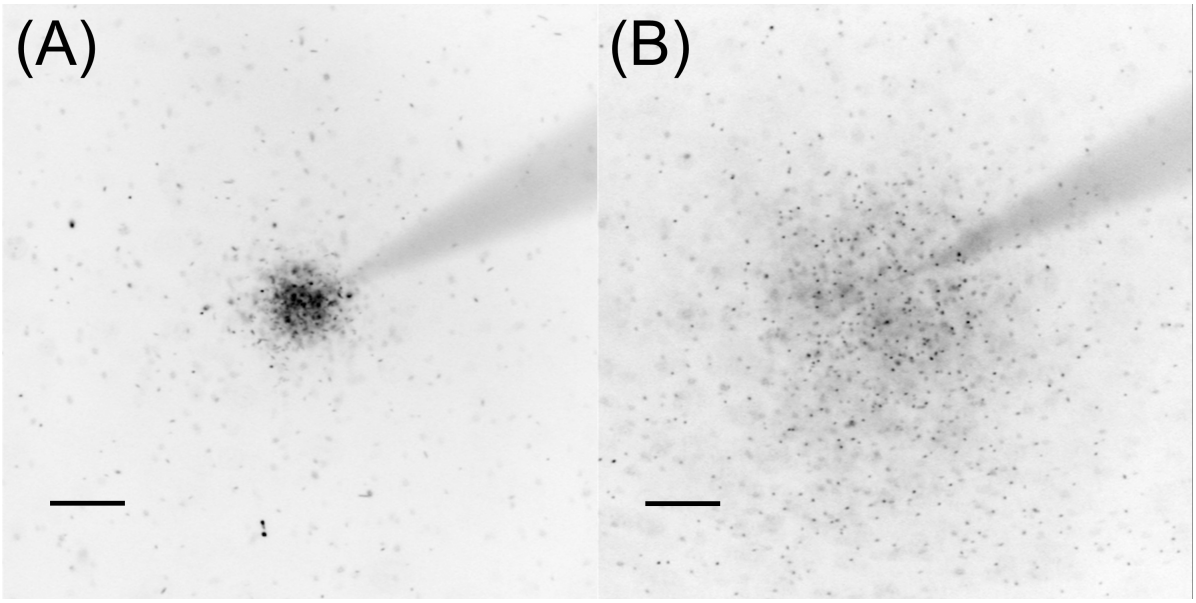

Figure 2: Swarming of (A) *V. alginolyticus* and (B) *E. coli* around a micropipette tip containing 0.5 mM serine. The triangular shape at the upper right corner is the micropipette with an opening of less than 1 μm so bacteria cannot get inside. The bars in both (A, B) are 100 μm. The bacteria are initially uniformly distributed and the snap shots (A) and (B) are taken 2 and 6 minutes after the insertion of the micropipette, respectively.

the messenger protein CheY-P in very different manners. In Chapter 3, we characterized the behavior of the flagellar motor of *V. alginolyticus* under different CheY-P concentration, studied the fluctuations in time durations of CCW and CW rotation of the flagellar motor, and proposed a model to describe how this marine bacterium regulates its motor. In Chapter 4, the bacterium's response to chemical stimulations is quantitatively measured, followed by an analysis on how the chemotaxis network functions compared to that of *E. coli*. Finally master equations similar to convection-diffusion equations are derived to describe the chemotactic strategies of *V. alginolyticus* and *E. coli* in a chemical gradient. Using the solutions of these equations, we analyzed the swarm formation dynamics observed in Figure 2 and speculated the advantage that *V. alginolyticus* can take by adopting its chemotaxis strategy to navigate in oceans.

2.0 THE MOTILITY PATTERN OF *V. ALGINOLYTICUS*

A large class of bacterial species possess a single polar flagellum with a bi-directional motor similar to *E. coli*. Being single polarly flagellated, low Reynolds-number (*Re*) hydrodynamics dictates that, aside from random thermal motions, the bacterium can only backtrack its trajectory when the motor reverses. This raises an interesting question concerning how this type of cells performs chemotaxis. Studies of motility patterns of single polarly flagellated bacteria *Pseudomonas citronellolis* (*P. citronellolis*) showed that the bacteria change the swimming direction by a brief reversal between two long runs. From the published trajectories [72], each reversal typically results in a small change in cell orientation, and thus several reversals appear to be necessary for a significant change in the swimming direction. Backtracking was also observed in a number of single flagellated marine bacteria such as *Shewanella putrefaciens*, *Pseudoalteromonas haloplanktis* (*P. haloplanktis*), and *V. alginolyticus*, which execute the so called run-reverse steps when following attractants released from porous beads and from algae [8, 45]. A pioneering experiment in *V. alginolyticus* revealed that the time reversal symmetry in the run and the reverse intervals is broken when the cell swims near a surface. In such a case, although the forward swimming remains more-or-less straight, the backward trajectory is remarkably curved and often forms a tight circle a few bacterial lengths in diameter [51]. This asymmetry in swimming can be explained by a hydrodynamic interaction with the surface that produces a turning (yawing) moment on the cell body [31]. A recent experiment also demonstrated that hydrodynamic interactions between a swimming cell (*Caulobacter crescentus*) and a surface can amplify thermal fluctuations, causing more efficient randomization of swimming trajectories [44]. These observations together suggest that single polarly flagellated bacteria may perform chemotaxis effectively only near surfaces.

However, when we observe the motility behavior of *V. alginolyticus* in a chemotaxis buffer

far from the surface, we found that the bacteria employ a novel cyclic 3-step (forward-reverse-flick) swimming pattern for chemotaxis; they regulate both forward and backward swimming times according to a given chemical profile. The time-reversal symmetric trajectories in the forward and the backward swimming are randomized by the last step, where the flick steers the cell to a new direction. Our experiment shows that the flagellum at the base is flexible and is actively involved in the directional change. We also found that while the flicking angle θ appears to be random, it has the highest probability at $\theta \approx 90^o$, which maximally randomizes the swimming trajectory. Below we unfold the details of the motility pattern of *V. alginolyticus* with more quantitative analysis.

2.1 THE STEADY-STATE MOTILITY PATTERN OF *V. ALGINOLYTICUS* IS A CYCLIC 3-STEP PROCESS

We conducted our measurements (see Materials and Methods) using a *V. alginolyticus* strain YM4 that possesses a single left-handed polar flagellum and a flagellar motor powered by Na^+ ions [36]. The handedness of the flagellum dictates that when the flagellar motor rotates in the CCW direction, it pushes the cell body forward but when the motor reverses, it pulls the cell body backward. We found that the bacterial swimming trajectories, even far from surfaces (>500 μm), are not smooth but interrupted by sharp kinks and bends. Figure 3(A) displays such a quasi-two-dimensional bacterial swimming trajectory in a motility medium TMN. Because the surface is sufficiently far, the observation suggests that the bacteria are actively involved in changing swimming directions. A study of a large number of trajectories (˜800) shows that the abrupt change in the swimming direction $\Delta\theta$ is always associated with motor reversal, and belongs to one of the two categories, those that change with a large angle $\Delta\theta \approx 180^o$ and those that change with an intermediate angle $0^o < \Delta\theta < 180^o$. Figure 4 is a plot of the probability density function (PDF) $P(\Delta\theta)$, which displays a bimodal distribution with a sharp peak centered at $\Delta\theta \approx 180^o$ and a broader peak around $\Delta\theta \approx 90^o$. This bimodal distribution indicates the existence of two distinct processes responsible for changes in the swimming directions.

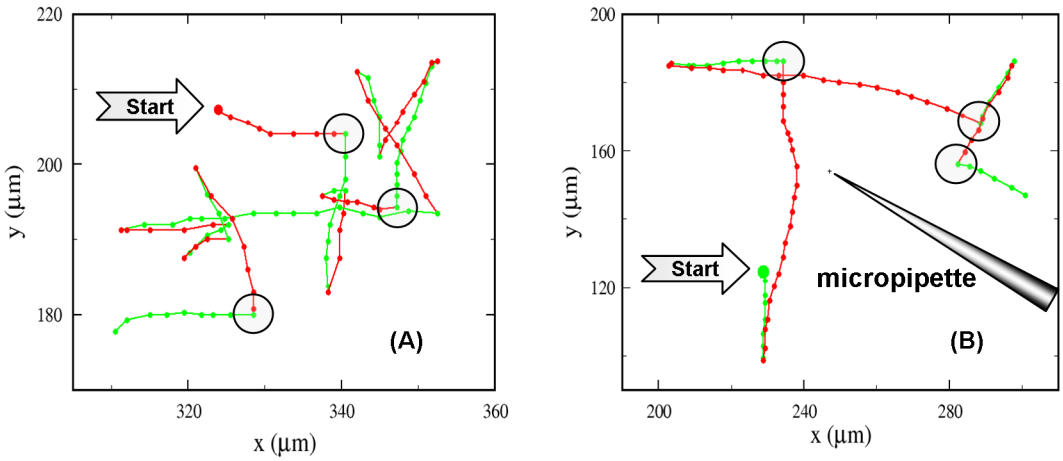

Figure 3: Bacterial trajectories in a motility medium TMN (A) and in a steep chemical gradient created by a micropipette filled with 1 mM serine (B). The big solid circles are the starting points of the bacterial tracks and the small solid circles represent the positions at an equal time interval of 0.067 s. The green and the red segments correspond to the forward and the backward trajectories, respectively. The large open circles marked the flicking events; for clarity, not all flicking events are marked in (A).

In an effort to clarify in details the motion of the bacteria, particularly the orientation of the flagellum with respect to the cell body during the transient period of the directional change, we used fast video imaging and fluorescence microscopy to record bacterial swimming in TMN. The fluorescence labeling renders the flagellum visible under the microscope so that the swimming directions can be determined. We found that $\Delta\theta$ can be divided into two groups. The large directional change ($\Delta\theta \sim 180^o$) is always associated with the transition from forward to backward swimming, which gives rise to the distinctive, cusp-like segments in bacterial trajectories as displayed in Figure 3. The transitions from backward to forward swimming, on the other hand, always result in more varied turning angles $\Delta\theta$ and are responsible for the broad peak in Figure 4. Since a forward run must be preceded by a backward run and vice versa, it follows that the steady-state motility pattern of the bacterium is a 3-step process, which we call the run-reverse-flick process. The last step allows the cell to veer to a new direction, and the 3-step process ensues. This is in contrast with the motion of *E. coli*, which cycles through a 2-step (run-tumble) process, and the directional randomization occurs during the CW period .

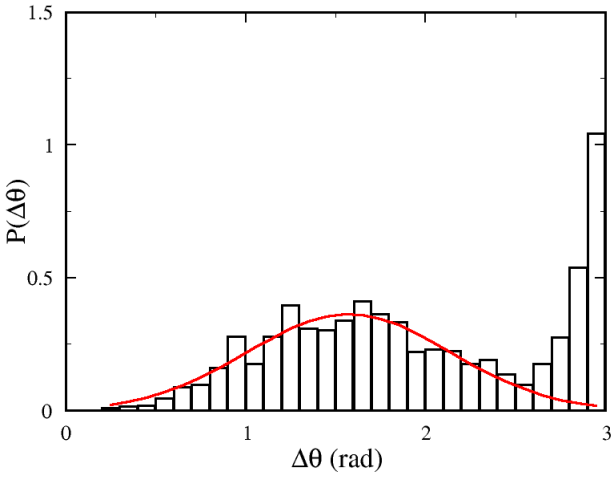

Figure 4: Distribution of abrupt changes in the swimming direction $\Delta\theta$ in a homogeneous medium. The distribution contains two peaks, a broad one at $\Delta\theta \approx \pi/2$ and a narrow one at π. The solid lines in the figures are fittings using a Gaussian function.

2.2 THE BACTERIAL FLAGELLUM IS ACTIVELY INVOLVED IN RANDOMIZING SWIMMING DIRECTIONS

The change in the swimming direction can be achieved either by spontaneous rotational diffusion of the cell body or by a thrust force generated by the flagellum. It is evident from a mathematical analysis of swimming in low Re ($\tilde{}10^{-4}$) that a sharp change in the swimming direction ($\Delta\theta \sim 90^o$) cannot be accomplished if the flagellum and the cell body remain coaxial. Nor can it be achieved via a simple cyclic movement of the flagellum with respect to the cell body, since such one-degree-of-freedom motion at low Re always recovers the bacteriums starting configuration [58]. Inspections of fast video images (100 fps) showed that the transitions from forward to backward swimming are rapid, within $\tilde{}1/30$ s, but the transitions from backward to forward swimming take a longer time, up to $\tilde{}1/10$ s. Approximating the bacterial cell body as an ellipsoid with a semi-major axis $a = 1.5\,\mu$m and a semi-minor axis $b = 0.5\,\mu$m, the rotational diffusion coefficient about its minor axis is $D_{r2} = \frac{3k_BT}{8\pi\eta a^3}(\ln\frac{2a}{b} - \frac{1}{2}) = 0.19\,\text{rad}^2/\text{sec}$, where $\eta = 10^{-3}\,\text{N}\cdot\text{s/m}^2$ is the dynamic viscosity coefficient, k_B is the Boltzmann factor and $T = 300$ K is the temperature [11]. Thus, the typical angular variation is $\delta_{rdiff} = \sqrt{4D_{r2}\Delta t} = 0.16$ rad during $\Delta t = 33$ ms and $\delta_{rdiff} = \sqrt{4D_{r2}\Delta t} = 0.28$ rad during $\Delta t = 0.1$ s . We noticed that the former agrees rather well with the width of the sharp peak in Figure 4, but the latter is about a factor of six smaller than the center position ($\sim \pi/2$) of the broad peak in Figure 4. In other words, $P(\Delta\theta)$ in Figure 4 cannot be accounted for by the passive rotational diffusion of the cell body and its broadness suggests that the distribution of the flicking angle may be spatially uniform given by $\frac{1}{2}\sin(\Delta\theta)$. However, experimentally we found that a Gaussian distribution fits our data better as illustrated by the solid line in the figure. The fitting procedure yields a mean of 89^o and a standard deviation of 30^o.

We also conducted measurements using fluorescence microscopy, where *V. alginolyticus* were labeled with dye Nano Orange (see Materials and Methods). Figure 5 displays a labeled cell whose flagellum is discernible. However, because of its rapid rotation, the fine helical structure is blurred. Careful analyses of fluorescence video images such as these ones showed that upon switching to forward swimming, the flagellum and the cell body are not coaxial,

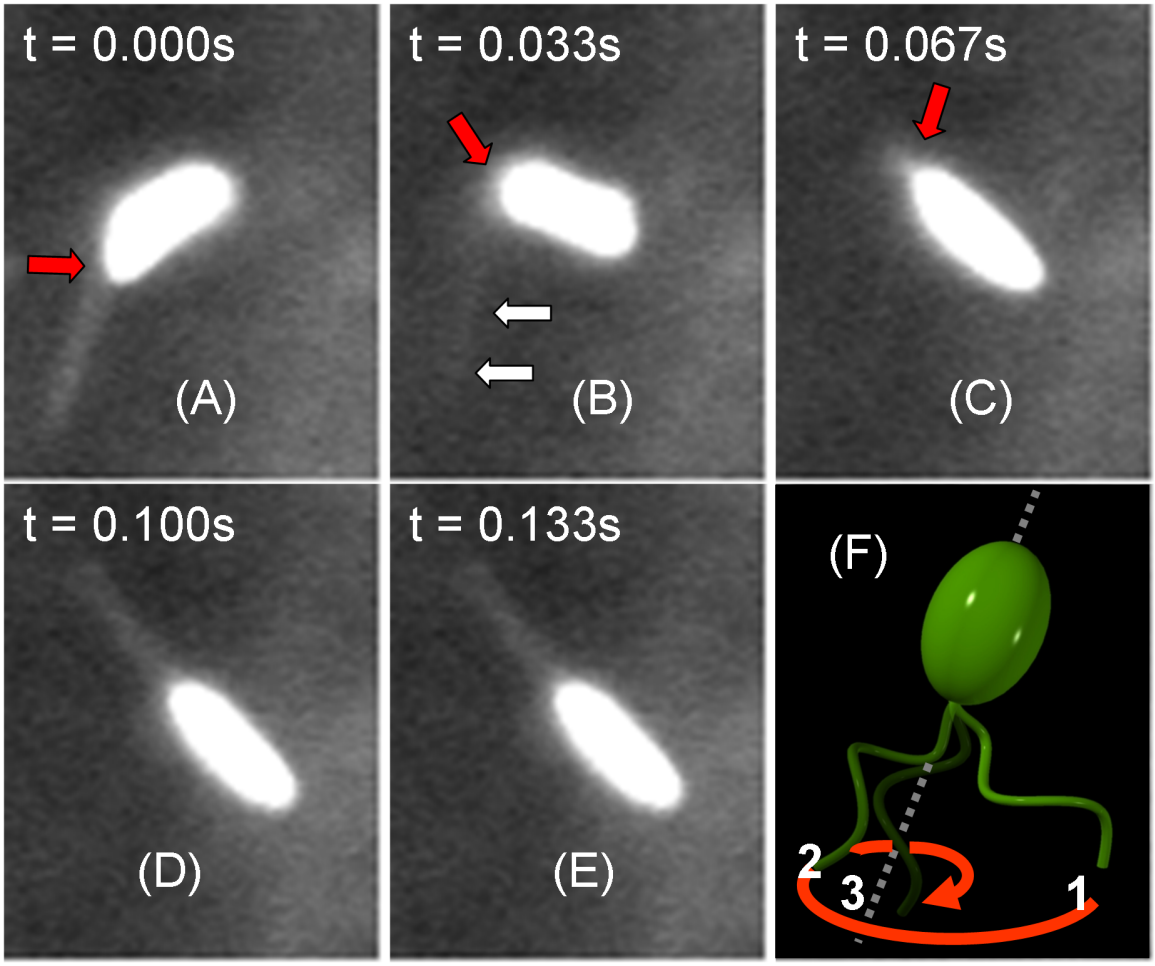

Figure 5: Fluorescent images of a swimming cell of *V. alginolyticus*. In (A-E), the bacterium is labeled with Nano Orange dye. The flagellum is visible when it is in the focal plane. A bend at the base of the flagellum is discernible and becomes amplified over time as indicated by the red arrows. However, when the flagellum flicks, it moves out of the focal plane and becomes blurred; such as the one indicated by double arrows in (B). The time interval between the images is 1/30 s and the cell body length is ˜ 3 μm. The 3D drawing in (F) depicts the relative positions of the flagellum to the cell body at the last stage of flicking. Specifically, to align with the cell-body axis, the tip of the flagellum starts from position 1, traces out a hyperbolic spiral, and ends at position 3. The forward swimming ensues.

and a small kink forms between them (see Figure 5(A)). This small kink is rapidly amplified by the CCW rotation of the flagellar motor that pushes the cell body at an angle. As shown in Figures. 5(B, C), the angular amplification is rapid and efficient, i.e., the cell rotates by ˜90^o in less than 0.1 s while its center of mass translates only ˜1/2 of its body length. After the new direction is selected, the flagellum aligns with the cell body axis via a large swing with its tip tracing out a hyperbolic spiral. This last step in the flicking process is depicted schematically in Figure 5(F). As one can see, the flicking employs both bending and rotation of the flagellum, bypassing the limitation of the scallop theorem. We show below that for an initial bending angle $\theta_0 \geq 10^o$, it is possible to account for the fast kinetics of this angular amplification based on the thrust force generated by the flagellar motor. Also, the torque required for the realignment of the flagellum is ˜10^4 PN·nm, which is of the same order of magnitude as the measured stalling torque of the flagellar motor [68].

For simplicity, we assume that the cell body rotates around its center of mass. The equation of motion for the cell-body rotation is given by

$$\gamma_2 \frac{d\theta}{dt} = aF \sin\theta \tag{2.1}$$

where $\gamma_2 = \frac{k_B T}{D_{r2}}$ is the rotational drag coefficient of the cell body. F is the thrusting force which can be estimated by $F = A_1 v$, $A_1 = 4\pi\eta a/(\ln(\frac{2a}{b}) - \frac{1}{2})$ being the linear drag coefficient for the cell body and v the swimming speed. This equation can be integrated with the result

$$\theta(t) = \cos^{-1}\left(\frac{C_0 \exp(-t/\tau) - 1}{C_0 \exp(-t/\tau) + 1}\right) \tag{2.2}$$

where $\tau = \gamma_2/2aF$ and $C_0 = (1 + \cos\theta_0)/(1 - \cos\theta_0)$. One can then evaluate the time t it takes for $\theta(t)$ to reach $\pi/2$ and this time t is plotted as a function of θ_0 in Figure 6. As expected t increases rapidly as θ_0 decreases. For $\theta_0 = 10^o$, $t = 0.06$ s, which is about two video frames and is consistent with our observation in Figure 5(A-E). This suggests that no other active element may be required to produce the rapid turning movement of the cell body seen in our experiment. However, in some of our video images, θ_0 as large as 40^o were observed, suggesting that the initiation of flicking may not be totally passive and may be assisted by an active element or by the release of the elastic energy stored in the motor-flagellum complex during the backward swimming interval. In such a case rotating by 90^o

takes less than 0.03 s. We found that the above calculation does not strongly depend on the assumption about the location of the rotation axis. For instance, by assuming that the cell rotates about a fixed axis at the front end of the cell body, t only changes by about 15% and thus will not significantly alter our above conclusion.

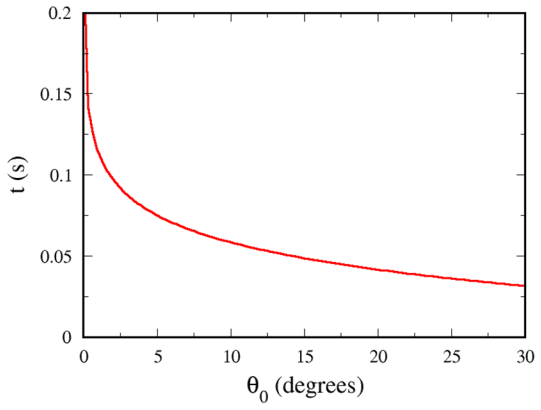

Figure 6: The time t required for the cell body to rotate 90^o as a function of the initial bending angle θ_0. The calculation shows that as long as $\theta_0 \geq 10^o$, t depends weakly on θ_0 and is typically less than 0.05 s, which is consistent with our observations.

It is remarkable that after flicking, the flagellum realigns itself swiftly with the cell-body axis, and the bacterium resumes its forward swimming. While it is unclear how this last step is accomplished at a molecular level, we wish to know if the torque involved is within the limit of the flagellar motor of *V. alginolyticus*. As depicted in Figure 5(F), the motion of the flagellum at this step is rather complex. It involves the whole flagellum swinging about the cell-body axis with the tip of the flagellum tracing out a hyperbolic spiral. The sweeping angular frequency ω_R based on our fluorescence microscopic measurements is $\omega_R/2\pi \approx 30$ Hz. A full hydrodynamic calculation of the torque is difficult, and in the following we seek a simpler calculation using the resistive force theory.

We assume that in the lab coordinates (x, y, z) the cell body is along the z axis, and the flagellum rotates about the x axis with a constant angular velocity ω_R. At the end of rotation it aligns with the body axis as depicted in Figure 7. We assign a fixed local coordinate (x', y', z') on the flagellum, and within this coordinate system the flagellum can

be parametrized as

$$\overrightarrow{h}(s) = (R\cos ks,\ R\sin ks,\ \sqrt{1-k^2R^2}s) \tag{2.3}$$

where R is the radius of the helix, k is the wave number measured along the contour and s is the contour length along the flagellum. Without losing generality, let x' axis be parallel to the rotation axis x at all times and z' axis coincide with y axis at $t = 0$ as depicted in Figure 7. We will calculate the torque based on this instantaneous configuration, but the result holds for other angular positions of the flagellum. Assuming for simplicity that the flagellum does not rotate about its own symmetry axis z', the velocity of the flagellar segment located at s to $s + ds$ in the local coordinates can be readily calculated as

$$\overrightarrow{v}(s) = \overrightarrow{\Omega} \times \overrightarrow{h}(s) = (0,\ \sqrt{1-k^2R^2}\omega_R s,\ \omega_R R\sin ks) \tag{2.4}$$

where $\overrightarrow{\Omega} = (\omega_R,\ 0,\ 0)$ is the angular velocity. This velocity can be decomposed into the tangential component $\overrightarrow{v_t}$ and the normal component $\overrightarrow{v_n}$ with the result

$$\begin{aligned} \overrightarrow{v_t}(s) &= (\overrightarrow{v}(s)\cdot\hat{t}(s))\hat{t}(s) \\ &= \sqrt{1-k^2R^2}\omega_R R(-ks\cos ks + \sin ks)(-Rk\sin ks,\ Rk\cos ks,\ \sqrt{1-k^2R^2}) \end{aligned} \tag{2.5}$$

$$\overrightarrow{v_n}(s) = \overrightarrow{v}(s) - \overrightarrow{v_t}(s) \tag{2.6}$$

where $\hat{t}(s) = (-Rk\sin ks,\ Rk\cos ks,\ \sqrt{1-k^2R^2})$ is a unit vector along the tangential direction of the flagellum. The tangential and the normal force on the segment can be obtained from Eq. 2.5 and 2.6:

$$\overrightarrow{F_t}(s)ds = C_t\overrightarrow{v_t}(s)ds \tag{2.7}$$

$$\overrightarrow{F_n}(s)ds = C_n\overrightarrow{v_n}(s)ds \tag{2.8}$$

where $C_t = \frac{2\pi\eta}{\ln(2\Lambda/r)-1/2}$ and $C_n = 2C_t$ are respectively the tangential and the normal viscous coefficient. In the above, r is the radius of the flagellar filament and Λ is the pitch. The net

force per unit length is given by $\overrightarrow{F}(s) = \overrightarrow{F_t}(s) + \overrightarrow{F_n}(s)$, and the torque per unit length about the rotation axis x is then given by $d\overrightarrow{N_R} = \overrightarrow{h}(s) \times \overrightarrow{F}(s)$. The total torque on the flagellum is obtained by integrating s from 0 to L, the contour length of the flagellum

$$\overrightarrow{N_R} = \int_0^L \overrightarrow{h}(s) \times \overrightarrow{F}(s) ds \tag{2.9}$$

The result of this integral consists of terms proportional to L^3 and $O(L^2)$ terms. It is clear that the $O(L^2)$ terms are due to fringe fields, and for a long helix the leading term is

$$\overrightarrow{N_R} = (\frac{1}{3} C_n L^3 \beta [1 - \frac{1}{2}(1-\beta)(1-\gamma_k)]\omega_R,\, 0,\, 0) \tag{2.10}$$

where $\beta = 1 - k^2 R^2$ and $\gamma_k = C_t/C_n = 1/2$.

Using the measured geometric parameters tabulated in Table. 1, we found $N_R \approx 10^4$ pN·nm. This value is about three times greater than the stalling torque, $N_{max} = 3 \times 10^3$ pN·nm, measured by Sowa et al [68]. Considering the approximation made about the movement of the flagellum in the calculation, the discrepancy between the measurement and the calculation may not be considered significant. Hence, it is likely that the flagellar motor alone may be sufficient in powering the sweeping motion seen in the experiment. However, it remains a possibility that a part of energy driving the flicking motion may be stored as elastic energy in the motor-flagellar complex when the flagellum is off axis with respect to the cell body. The sweeping motion of the flagellum then may be interpreted as an instability that allows the stored elastic deformation to be released, causing the flagellum to realign with the cell-body axis. We would like to emphasize that presently nothing is known about the molecular components that are responsible for the flicking movement. Our calculation simply shows that the energy or the torque required is compatible with what we know about the flagellar motor. The calculation certainly cannot rule out the possibility that this important process is driven by another independent power source.

We also observed that the flicking of the flagellum is correlated with the bacterial swimming speed. In de-energized cells, either by reducing Na^+ ions from the motility medium or by oxygen depletion, the bacteria abolish the last flicking step altogether. Likewise, increasing the viscosity of the motility medium has the effect of slowing down motor rotation as

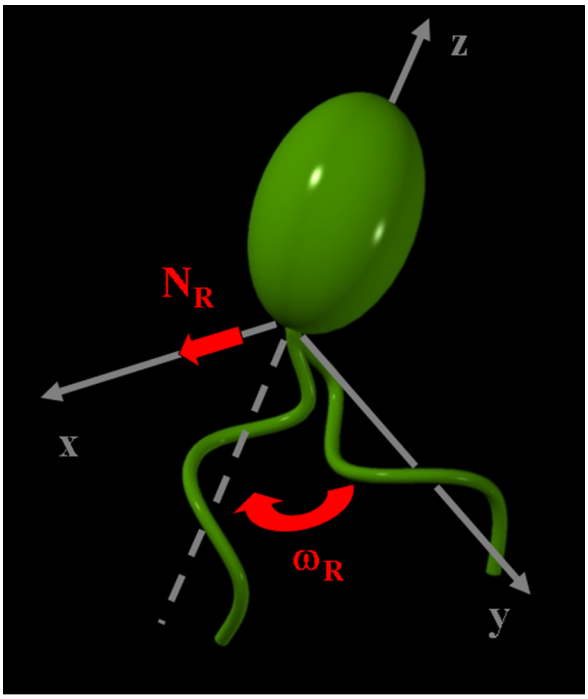

Figure 7: A simplified flagellum movement at the end of the flicking process. In contrast to Figure 5(F), here in order to facilitate the calculation we assume that the flagellum is initially along the y axis, and it rotates about the x axis until it aligns with the bacterial cell-body, or z axis. The rotational angular frequency is $\omega_R/2\pi \approx 30$Hz, and the torque $N_R \approx 10^4$ pN·nm is calculated using the resistive force theory.

a, μm	b, μm	Ψ, ^{o}	L, μm	Λ, μm	R, nm	r, nm
1.5(0.5)	0.5(0.1)	36.2(0.5)	4.59(1)	1.49(0.02)	140(1)	16

Table 1: The geometric parameters of *V. alginolyticus* given in this table are determined using fluorescence microscopy [19] and TEM [50]. Here a and b are the semi-major and semi-minor axes of the cell body, Λ, Ψ, L, and R are respectively the pitch, the pitch angle, the contour length and the radius of the helical flagellum. The numbers in the brackets are standard errors of the means. The filament radius r was measured using TEM and its value is given in Ref. [50]

well as inhibiting flagellar flicking. These observations together suggest that these two processes, active swimming and flicking, are linked, supporting the idea that the same propulsion apparatus is used for both types of movements.

2.3 THE 3-STEP MOTILITY PATTERN CAN ALSO BE OBSERVED IN OTHER BACTERIA

In order to verify that the 3-step process is an intrinsic swimming pattern adopted by *V. alginolyticus*, we also studied two additional strains, VIO5 with a single polar flagellum and 138-2 (wild type) [41]. The bacterium 138-2 is capable of expressing both polar and lateral flagella. However, when grown in a liquid medium, only the polar flagellum is expressed. VIO5 is a mutant strain of *V. alginolyticus* that expresses a single polar flagellum. Our observations showed that both bacterial strains execute the 3-step cycles identical to YM4.

In an earlier work exploring rapid chemotactic response of *P. haloplanktis*, it was reported that *P. haloplanktis* displayed a remarkable chemotactic advantage over *E. coli* [70]. According to a computer model, the investigators concluded that the higher swimming speed increases the chemotactic advantage of *P. haloplanktis*, but to a smaller degree than observed in the experiments. They speculated that the bacteria rely on additional behavioral strategies, which was attributed to the run-reverse swimming pattern of *P. haloplanktis*. Since similar to *V. alginolyticus*, *P. haloplanktis* has a single polar flagellum, we were curious about whether *P. haloplanktis* also adopt the 3-step strategy. Since these bacteria swim at a higher speed and for a longer time before a reversal, tracking is more difficult as they easily get out of the field of view or become defocused. As a result, presently we do not have extensive statistics about how *P. haloplanktis* swim. However, based on our limited data, it is evident that *P. haloplanktis* incorporate flicks into their motility. Using the $40\times$ objective, we can resolve their body orientations; it is commonly observed that the long axis of the cell body reorients by as much as 90^o from one frame to the next within 1/30 s. Examining the motility pattern of *P. haloplanktis* carefully, we found that the bacterial trajectories also consist of intermediate angular changes similar to those flicking angles observed in *V. alginolyticus*.

We also obtained several bacterial tracks (see Figure 8) that seem to be 3-step cycles, although we are unsure whether all cells exhibit the same pattern or whether the flick occurs during the transition from backward to forward swimming or vice versa. It remains an intriguing possibility that the flicking step in *P. haloplanktis* could be on-demand, namely, the cell flicks only when necessary. This would represent a more advanced chemotactic strategy than the cyclic 3-step process we found in *V. alginolyticus*. It certainly would require more components and perhaps more sophisticated chemotactic regulation. This important issue can be clarified only when more controlled experiments are carried out. One thing that can be concluded from all these observations, however, is that backtracking and flicking are important for bacteria living in oceans where nutrients appear and disappear rapidly.

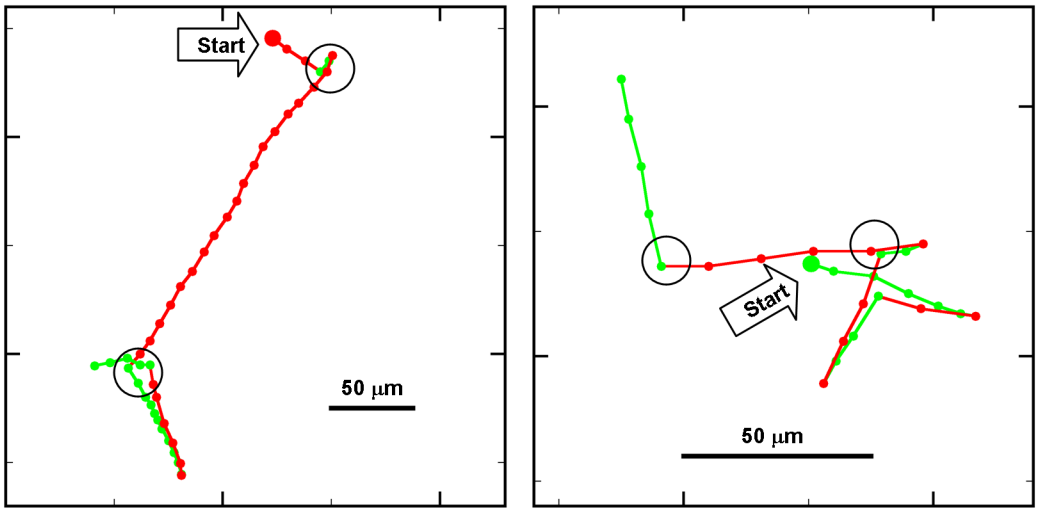

Figure 8: Swimming trajectories of *P. haloplanktis* in sea water. The scale bars in both figures are 50μm. The big solid circles are the starting points of the tracks. The green and red lines represent putative forward and backward swimming segments, respectively. These colors were assigned according to the 3-step motility pattern of *V. alginolyticus*, i.e., a flick is always followed by forward swimming. The large open circles marked the flicking events, but not all flicks were marked for clarity.

2.4 SWIMMING BEHAVIOR OF *V. ALGINOLYTICUS* IN MOTILITY MEDIUM

The stochastic motion of *E. coli* in the medium can be approximated as a random walk, since smooth runs are interrupted by tumbles which randomizes the cell-body orientations. It was also measured that the lengths of run(CCW) interval Δ_{CCW} and of tumble(CW) intervals Δ_{CW} are both of exponential distributions, namely $P(\Delta_{CCW}) \propto \exp(-\Delta_{CCW}/\tau_{CCW})$ and $P(\Delta_{CW}) \propto \exp(-\Delta_{CW}/\tau_{CW})$, where τ_{CCW} and τ_{CW} are mean run length and tumble length [14]. Since $\tau_{CW} = 0.14 \pm 0.19$ s while $\tau_{CCW} = 0.86 \pm 1.18$ s [14], assuming each run is straight, the diffusivity of *E. coli*'s motion can be calculated as

$$D_E = \frac{v^2 \tau_{CCW}^2}{3(1-\alpha)(\tau_{CW} + \tau_{CCW})} = \frac{l^2}{3(1-\alpha)(\tau_{CW} + \tau_{CCW})} \tag{2.11}$$

where $\alpha = \langle \cos\theta \rangle$ is the average of the directional cosine of the trajectories and l is the mean net displacement in a run. For *E. coli*, it was measured that $\alpha \approx 1/3$. Assuming swimming speed $v \approx 20$ μm/s, it yields that $D_E \approx 180$ μm^2/s [11]. This is a very large diffusivity compared to that of a non-motile cell, which is ˜0.2 μm^2/s. In isotropic and neutral chemical environments, *E. coli* swims in such a random walk pattern to explore for food efficiently.

For *V. alginolyticus*, although the 3-step forward-reverse-flick cycle is deterministic and has been observed in nearly all bacteria in the population as long as they swim with a normal speed, the bacterial swimming pattern is also stochastic in that the forward and the backward intervals, Δ_f and Δ_b, as well as the flicking angle θ, fluctuate from moment to moment. Figure 9(A) displays a scattered plot of the measured pairs of forward and backward swimming times (Δ_f, Δ_b) between two flicks for an ensemble of ˜800 bacteria. The uniform distribution of the data points on the graph indicates that there is little correlation between Δ_f and Δ_b. We also calculated PDFs of Δ_f, Δ_b, and $\phi_{CW} = \Delta_b/(\Delta_f + \Delta_b)$ (or equivalently $\phi_{CW} = \Delta_{CW}/(\Delta_{CCW} + \Delta_{CW})$), which are displayed in Figures. 10(A, D) and Figure 12(A). There is no significant difference between the distributions of Δ_f and Δ_b, or equivalently between the forward and the backward swimming distances. This is also evident in $P(\phi_{CW})$, which has a mean of 0.56 and is more or less symmetric with respect to $\phi_{CW} = 0.5$. This raise

the question whether the chemotaxis network of *V. alginolyticus* differentiates forward from backward swimming in a steady state. A prominent feature of $P(\Delta_f)$ and $P(\Delta_b)$ is that they are both peaked at short times, 0.2 and 0.37 s, respectively. It is only for long time intervals that the data display an exponential behavior (see the inset) with the characteristic times of 0.40 and 0.27 s for $P(\Delta_f)$ and $P(\Delta_b)$, respectively. Thus, Δ_f and Δ_b of *V. alginolyticus* are not exponentially distributed. Interestingly, however, we found that the difference in the time intervals $|\Delta_f - \Delta_b|$ does with a characteristic time of 0.31 s, as displayed in Figure 11(A). Thus the mean net displacement in one cycle for *V. alginolyticus* can be calculated as $l = v|\tau_f - \tau_b|$, where $\tau_f = \langle\Delta_f\rangle$ and $\tau_b = \langle\Delta_b\rangle$. Since on average it takes $\tau_f + \tau_b$ for *V. alginolyticus* to move a distance of l, Eq. 2.11 should be modified as

$$D_V = \frac{v^2(\tau_f - \tau_b)^2}{3(1-\alpha)(\tau_f + \tau_b)} = \frac{l^2}{3(1-\alpha)(\tau_f + \tau_b)} \tag{2.12}$$

As shown in Figure 13(A), the flicking angle θ peaks at $\theta \approx \pi/2$, leading to $\alpha \approx 0$. Let $v = 45$ μm/s, $\tau_f - \tau_b = 0.3$ s, and $\tau_f + \tau_b \approx 1$ s, we have $D_V = 66$ μm^2/s, which is much less than D_E. This compares rather well with the direct measurement $D_V = 58 \pm 30$ μm^2/s, which is obtained by measuring the mean-square displacements from bacterial tracks. Further more, for the 2-step process the net displacement in a cycle is $v\Delta_{CCW}$ and is always positive. However, for the 3-step process this quantity is $v|\Delta_f - \Delta_b|$; it can be positive or even be zero depending on $|\Delta_f - \Delta_b|$. Thus, the bacteria executing the 3-step cycle have the potential to regulate the CW and CCW intervals to significantly increase or decrease its diffusivity; the former is preferred for migration in a chemical gradient and the latter is required for localization.

2.5 *V. ALGINOLYTICUS* CARRIES OUT CHEMOTAXIS BY MODULATING THE MOTOR SWITCHING RATES

The motility patterns of both *E. coli* and *V. alginolyticus* resemble random walks in the motility buffer. For *E. coli*, once it is in an attractant gradient, it changes the trajectory from a random walk to a biased walk to migrate toward the source of the attractant by

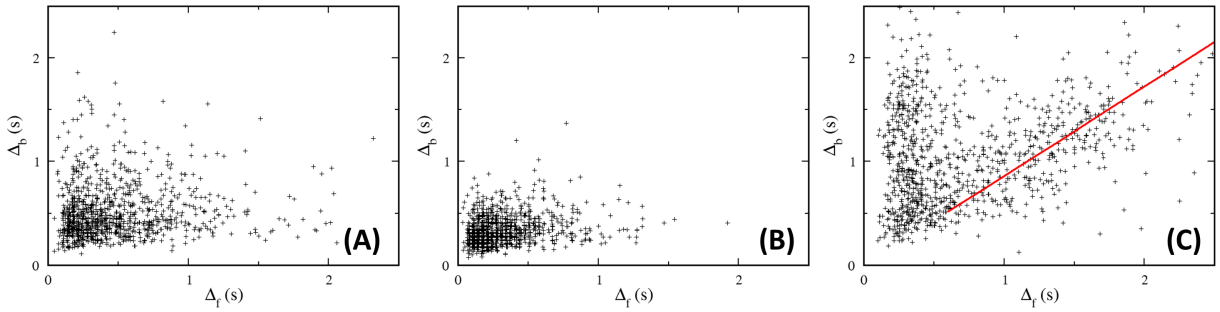

Figure 9: Pairs of consecutive Δ_b vs. Δ_f between two flicks in (A) motility buffer TMN, (B) motility buffer with 10 mM phenol, which is a repellent, and (C) near a micropipette tip filled with 1 mM serine, which is an attractant. Random shifts of less than 0.02 s are applied to avoid data points overlapping. In the homogenous medium, there is no correlation between Δ_f and Δ_b while in the attractant gradient there is a strong correlation between them. The biological cause of such a correlation is discussed later and in Figure 15. The red line in (C) is a linear fit to the data points with large Δ_f and has a slope of 0.86.

modulating the motor bias ϕ_{CW}. Specifically, when the cell climbs up an attractant gradient, ϕ_{CW} decreases to lower its tumbling probability so that runs in the favorable directions (toward attractants and away from repellents) get extended, resulting in net movement toward preferred environments [69, 76]. On the other hand, when the cell moves in an unfavorable direction, ϕ_{CW} increases so that the cell tumbles and reorients more frequently to explore into other directions. Besides biased random walk, bacteria have other ways to maneuver in an environment. One of them is changing the swimming speed, which is the tactic *E. coli* used to aggregate around the optimum temperature [23]. Another is modulating the directional angle between two adjacent runs, which is also observed in *E. coli* [60]. To understand how *V. alginolyticus* performs chemotaxis, we carried out another two tracking experiments. One of them is in the motility buffer containing 10 mM phenol, which is a repellent to *V. alginolyticus*. The other is near a micropipette tip filled with 1 mM serine, which is an attractant. We investigated the interval lengths, Δ_f and Δ_b, the corresponding swimming speeds, v_f and v_b, as well as the flicking angle θ, to infer the parameters tuned by

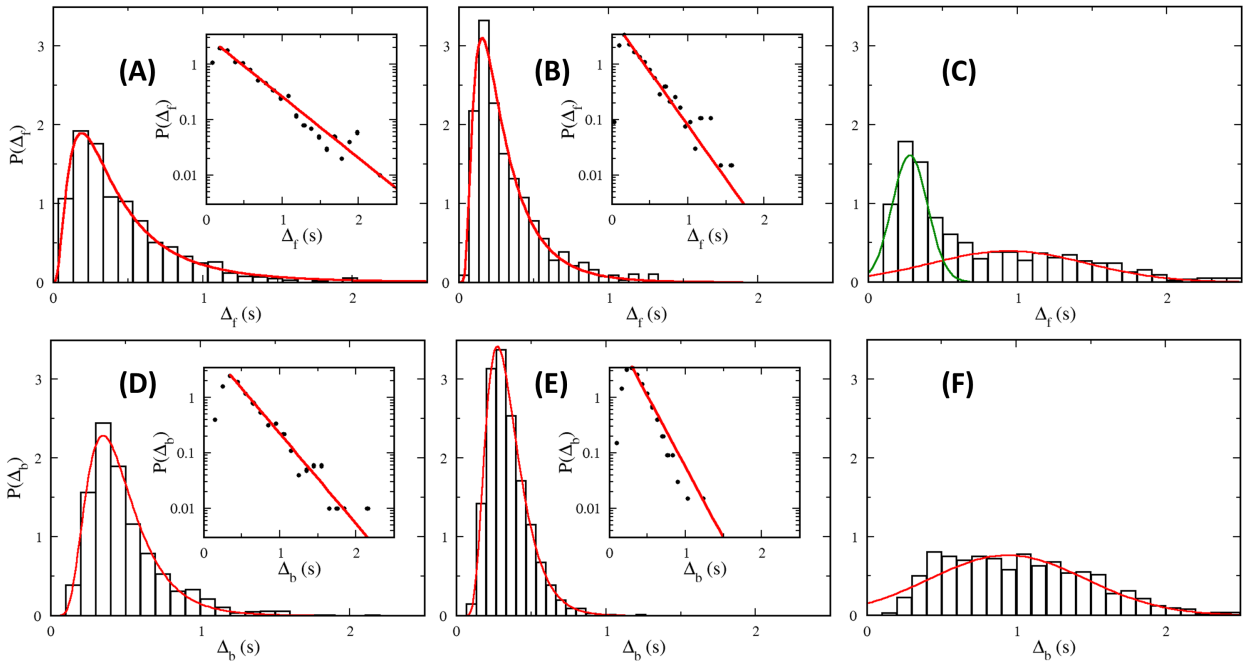

Figure 10: $P(\Delta_f)$ (A-C) and $P(\Delta_b)$ (D-F) measured in: (A, D) homogeneous motility buffer TMN, (B, E) homogeneous motility buffer with phenol and (C, F) inhomogeneous chemical profile created by a micropipette tip filled with 1 mM serine. The red lines in the main figure of (A, B, D and E) are fittings to an inverse Gaussian function. The insets in these four subplots are semilog plots of the same data sets as in the main figures. The red lines are exponential fits to the tail parts of the data. The good agreement between the data and the fits shows that for large Δ_f and Δ_b the PDFs are exponential. The red line in (F) is a Gaussian fit. The same fitting curve was rescaled and replotted in (E) as the red line. The green line in (C) is a Gaussian fit to the short-time peak of $P(\Delta_f)$.

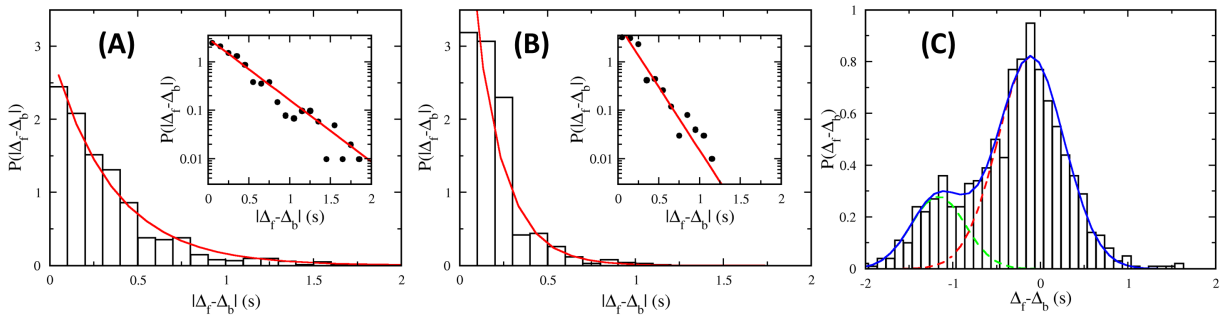

Figure 11: $P(|\Delta_f - \Delta_b|)$ measured in (A) motility buffer, (B) motility buffer with phenol and $P(\Delta_f - \Delta_b)$ measured around a tip filled with serine. In (A, B), the red lines are exponential fittings with characteristic times of 0.31 s and 0.17 s, respectively. The insets are the semi-log plot of the same data. In (C), the distribution consists of two peaks, which we modeled using two Gaussian functions and plotted as red and green dashed lines. The sum of the two was plotted as the blue solid line, which mimics our measured PDF well.

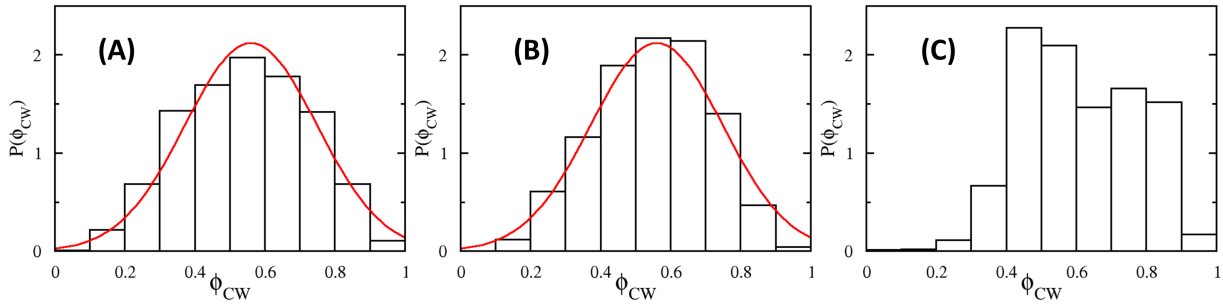

Figure 12: $P(\phi_{CW})$ were constructed from ~1000 pairs of consecutive Δ_b and Δ_f between two flicks measured in (A) motility buffer TMN, (B) motility buffer containing 10 mM phenol, and (C) near a micropipette tip filled with 1 mM serine. The red line in (A, B) is a normal distribution with a mean of 0.56 and a standard deviation of 0.19.

V. alginolyticus during chemotaxis.

For each experiment, we tracked the cells to get ˜1000 data points and the resulting statistics were presented in Figure 9-14. In Figure 13, instead of plotting all angular changes $\Delta\theta$, only the flicking angle θ were presented. It is evident that $P(\theta)$ hardly change, even in an inhomogeneous environment, indicating that the flicking angle is not actively regulated. In Figure 14, although the speeds in the motility buffer is about 10% higher than those in phenol and around the tip, the discrepancy can be attributed to the reduction in Na^+ concentration due to addition of phenol or serine solution. Also, if v_f and v_b were actively regulated, the shapes of $P(v_f)$ and $P(v_b)$ in the inhomogeneous environment around the tip are expected to be different from those in the homogeneous environment, like TMN with or without phenol. However as shown in Figure 14, all PDFs are qualitatively the same, suggesting that *V. alginolyticus* does not perform chemotaxis by modulating its swimming speed.

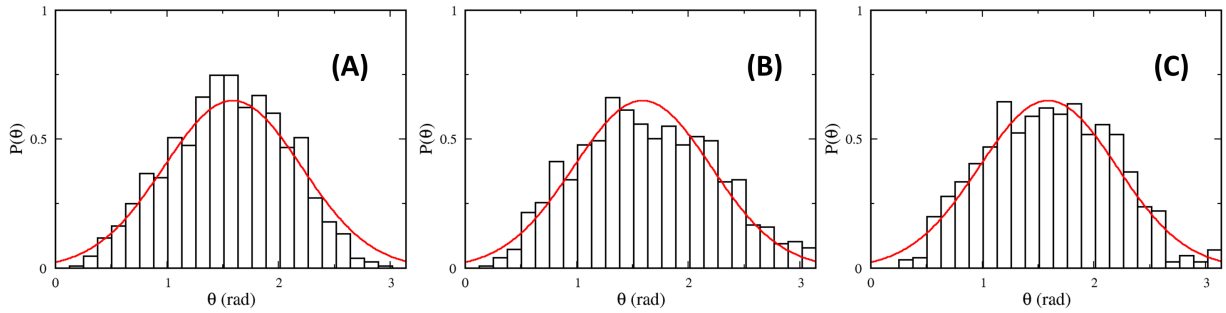

Figure 13: $P(\theta)$ were constructed from ˜1000 flicking angles θ measured in (A) motility buffer, (B) motility buffer containing 10 mM phenol, which is a repellent, and (C) near a micropipette tip filled with 1 mM serine, which is an attractant. The red line in (A-C) is a normal distribution with a mean of 1.59 rad and a standard deviation of 0.61 rad.

Distributions of Δ_f and Δ_b under different experimental conditions are presented in Figure 9-11. It is evident that these PDFs differ significantly from each other. When the cells are in a homogeneous medium with repellent, i.e., motility buffer containing 10 mM phenol, the cell still moves in a forward-backward-flick pattern, but with shorter Δ_f and Δ_b, as shown in Figure 10(B, E). $P(\Delta_f)$ in (B) and $P(\Delta_b)$ in (E) become significantly narrower

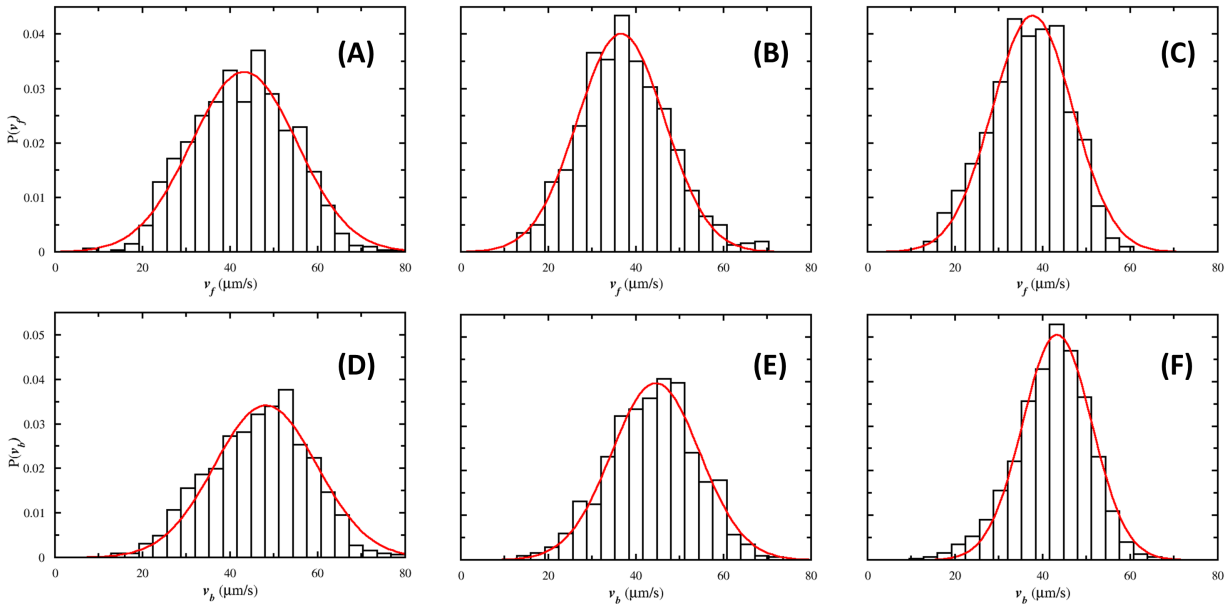

Figure 14: $P(v_f)$ (A-C) and $P(v_b)$ (D-F) measured in (A, D), homogeneous motility buffer TMN, (B, E) homogeneous motility buffer containing 10 mM phenol and (C, F) near a micropipette tip filled with 1 mM serine. ˜1000 forward and backward swimming intervals were tracked and corresponding mean speeds were calculated. The red lines are fittings using normal distributions with mean (μm/s)$\pm$std (μm/s) as (A): 43 ± 12, (B): 37 ± 10, (C): 38 ± 9, (D): 48 ± 12, (E): 44 ± 10, (F): 43 ± 8.

and peak at a shorter time, 0.17 s and 0.26 s, respectively. However, $P(\Delta_f)$ and $P(\Delta_b)$ still have the same shape and can be fitted using the inverse Gaussian function. Also, as shown in the scatter plot Figure 9(B), although the pairs concentrate around a shorter time scale, there is little correlations between Δ_f and Δ_b. Further more, similar to the result obtained in motility buffer, despite the fact that neither $P(\Delta_f)$ nor $P(\Delta_b)$ are exponential, $|\Delta_f - \Delta_b|$ does distributed exponentially with a characteristic time of 0.17 s, which is about half of that of $P(|\Delta_f - \Delta_b|)$ measured in the motility buffer. Thus in a homogeneous medium with repellent, *V. alginolyticus* still execute the 3-step cycle, resulting in random-walk-like trajectories, but with a smaller mean net displacement l in each cycle. Applying Eq. 2.12 with $v = 45$ μm/s, $\tau_f - \tau_b = 0.17$ s, and $\tau_f + \tau_b = 0.66$ s and $\alpha \approx 0$, we have $D_V = 29.6$ μm^2/s, about half of D_V measured in the motility buffer, which is $D_V = 66$ μm^2/s. It is known that when *E. coli* is subjected to repellent, it also reduces the diffusivity by increasing ϕ_{CW}. With larger ϕ_{CW}, the cell spent more time tumbling and $l = v\Delta_{CCW}$ is reduced. However, for *V. alginolyticus*, it reduces diffusivity by reducing both Δ_f and Δ_b, while keeping $P(\phi_{CW})$ about the same. As shown in Figure 12(B), $P(\phi_{CW})$ measured in the medium with 10 mM phenol can be mimicked adequately by the same normal distribution used to fit $P(\phi_{CW})$ measured in the motility buffer. Therefore, it seems that *E. coli* and *V. alginolyticus* both respond to repellent by decreasing the diffusivity, but *E. coli* achieves this goal by increasing ϕ_{CW}, while *V. alginolyticus* by increasing the switching rates to shorten both Δ_f and Δ_b.

In the tip experiment, we found that cells of *V. alginolyticus* can rapidly swarm around the tip, forming a compact cluster in a few tens of seconds. We followed the trajectories of ˜700 cells, and found that the bacteria still exhibit the 3-step swimming pattern near the point source, which is shown in Figure 3(B). Figure 9(C) is a scattered plot of Δ_b and Δ_f between two flicks. In contrast with Figure 9(A, B), where Δ_f and Δ_b are uncorrelated in homogeneous medium, strong correlations emerge between Δ_f and Δ_b when a sharp gradient is present. The data fall into two groups; those with very short Δ_f but relatively long Δ_b, and those with Δ_b being proportional to Δ_f, i.e., $\Delta_b \propto \Delta_f$ with a proportionality constant of 0.86 as delineated by the red line in Figure 9(C). This constant, which deviates slightly from unity, may be attributed to a small bias in the swimming speeds, i.e., for *V. alginolyticus* the backward swimming speed v_b was found to be ˜10% higher than the forward speed v_f.

Thus, the forward and backward displacements in a cycle are about the same, $v_f\Delta_f \sim v_b\Delta_b$, leading to a small net displacement l. The other branch, where Δ_f is much smaller than Δ_b, corresponds to a correction response, which will be discussed below.

The above peculiar correlations between Δ_f and Δ_b can be best illustrated by the simple physical picture depicted in Figure 15(A), which is supported by the measured trajectories in Figure 15(B). Imagine that a bacterium traverses a region of radius R containing attractant, and the region outside R is devoid of attractant. Suppose initially the bacterium swims backward, and at the edge of the boundary, the cell flicks and randomly picks a new direction as depicted by 1-2 or 1*-2* segments in the figure. For a sufficiently large radius R, ˜50% of the flicking events will reorient the cell to point outside R and the subsequent forward swimming interval (or the distance) will be short, which is indicated by segment 3 in the drawing. This contributes to the sharp peak in $P(\Delta_f)$ in Figure 10(C). On the other hand, the other 50% of the flicking events will reorient the cell to point inside R as depicted by segment 3* in the figure. The cell swims forward for a long distance until it reaches the boundary on the other side, it then backtracks over the same distance, and flicks again at the boundary. In this case, the backward swimming interval (segment 4*) is strongly correlated with the forward interval (segment 3*). Since the flicking angle is random, different lengths are generated inside R as illustrated in Figure 15(B). This yields a broad distribution in both $P(\Delta_f)$ and $P(\Delta_b)$ as displayed in Figure 10(C, F) and gives rise to the strong correlation between pairs of Δ_f and Δ_b in Figure 9(C).

From the above experiments, it is evident that like *E. coli*, *V. alginolyticus* also modulates the motor rotation or lengths of the swimming intervals to carry out chemotaxis. For *E. coli*, since only CCW rotation of the flagella can generate motility, it mainly regulates the run length during chemotaxis and modulates ϕ_{CW} according to external chemical cues [65]. However, for *V. alginolyticus*, this logic brings the cell down the gradient if the cell is climbing the gradient with a pulling CW-rotating flagellum, since if the cell reduces ϕ_{CW} it is more likely to reverse the motor and shorten the current migration up the gradient . It seems that for *V. alginolyticus*, since both CCW and CW rotation of the motor produce motility, Δ_f and Δ_b should be regulated in a similar fashion. This is indeed observed. In the motility buffer TMN, $P(\Delta_f)$ and $P(\Delta_b)$ took similar shapes and in the presence of the repellent phenol,

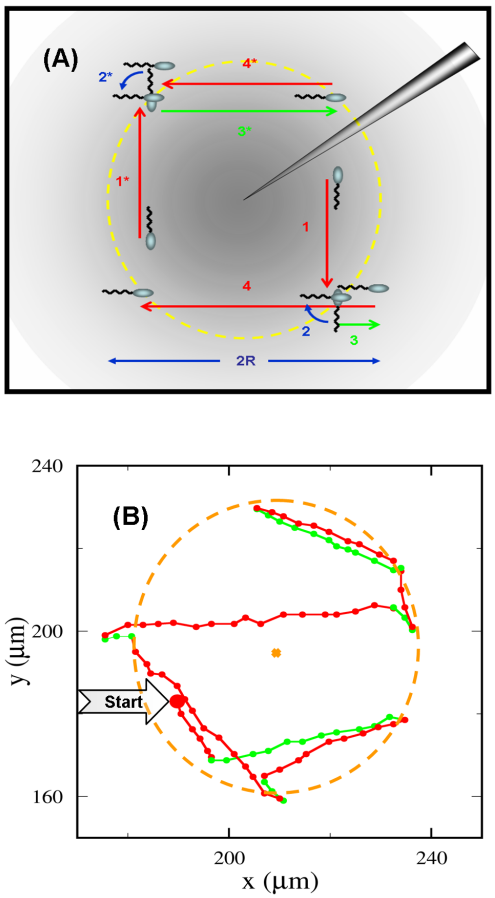

Figure 15: Bacterial chemotactic behaviors in a chemical gradient created by a micropipette tip filled with attractant. (A) Localization of bacteria near a sharp chemical gradient. A serine-filled micropipette tip introduces a quasi-stationary concentration gradient in a liquid medium. The bacterium carries out chemotaxis as described in the text. Near the point source of attractant, there are two different scenarios depicted at the left upper corner and the lower right corner. Here, Δ_f and Δ_b are correlated for the upper-left trajectories, but anti-correlated in the lower-right trajectories, i.e. a short forward swimming segment is most likely to be accompanied by a long backward swimming segment. (B) A measured *V. alginolyticus* trajectory near a micropipette tip. The cross at the center is the location of the pipette tip filled with 1 mM serine, and the circle (dashed line) is approximately the outer edge of the swarm. The large solid circle is the starting position of the bacterial track, which consists of forward (green) and backward (red) swimming segments. The small dots represent the positions of the bacterium at an equal time interval of 0.067 s.

both Δ_f and Δ_b are reduced resulting in a much smaller diffusivity. When the cell is exposed to a chemical gradient, both Δ_f and Δ_b can be increased to move the cell up the attractant gradient. However, due to the flicking at the end of the backward swimming interval, $P(\Delta_f)$ and $P(\Delta_b)$ took very different forms when the cells are close to the micropipette tip, as shown in Figure 10(C, F), and $P(\phi_{CW})$ biased strongly toward large ϕ_{CW} as shown in Figure 12(C). All these responses we observed are consistent with the following strategy: decrease the motor switching rates during the swimming interval in the favorable direction while increase the switching rate if the cell is running in the unfavorable direction, regardless whether it is a forward or backward swimming interval. In the next chapter, we explore how the flagellar motor of *V. alginolyticus* is regulated by the chemotaxis network so that the cell can regulate the motor switching rates in such a way to take advantage of the 3-step motility pattern.

3.0 THE FLAGELLAR MOTOR OF *V. ALGINOLYTICUS*

In this chapter, we studied how the flagellar motor of *V. alginolyticus* is regulated by CheY-P, which is the output of the chemotaxis network. As an introduction, we first presented the motor bias and switching rates as a function of CheY-P concentration measured in *E. coli* by P. Cluzel et al [20]. To explain the chemotaxis behavior of *V. alginolyticus* we observed in Chapter 2, we hypothesized that the switching rates of the motor of *V. alginolyticus* during both forward and backward swimming intervals should increase as the concentration of CheY-P increases. This proposal is then confirmed in the experiments where the bias and switching rates of the motor are quantitatively measured when CheY-P concentration is systematically varied. Based on the above measurement as well as $P(\Delta_f)$ and $P(\Delta_b)$ measured in different circumstances, we constructed a model to describe how CheY-P interacts with the flagellar motor of *V. alginolyticus* to regulate its switching rates.

3.1 BEHAVIOR OF THE FLAGELLAR MOTOR IN *E. COLI* AS A FUNCTION OF CHEY-P CONCENTRATION

The motion of *E. coli* in a chemical profile is directly determined by the rotating directions of its flagellar motors, which is regulated by CheY-P, the active form of chemotaxis protein CheY [25]. CheY-P interacts with the motor switch at the base of the motor though binding and unbinding. The more CheY-P in the cell, the more CheY-P binds to the motor switch and the longer the motor persists in the CW state. By regulating the CheY-P concentration, the chemosensory system directs the rotation of the motor, enabling *E. coli* to carry out chemotaxis through a biased random walk. Quantitatively, the average CW bias of the

motor (or the probability that the motor rotates in the CW direction) ϕ_{CW} is a function of CheY-P concentration [YP] as shown in Figure 16(A) [20]. A striking feature of $\phi_{CW}([YP])$ is that it rises rapidly over a narrow range from 0 to 1, indicating that the motor is very sensitive to CheY-P. $\phi_{CW}([YP])$ can be fitted to a Hill function as in Eq. 3.1,

$$\phi_{CW}([YP]) = \frac{1}{1 + (\frac{K_m}{[YP]})^H} \tag{3.1}$$

where $K_m = 3.1$ μM is the dissociation constant and H $\sim$10 is the Hill coefficient, which indicates the sharpness of the transition from 0 to 1 [20]. With $H \sim 10$, increasing [YP] from $K_m = 3.1$ μM by 10% to 3.4 μM can increase $\phi_{CW}(K_m) = 0.5$ by 50%. Such a sensitive motor enhances the responsiveness of the motor to small changes in [YP] and therefore the chemotactic response to external stimuli. In wild type cells, [YP] is maintained at such a level so that the cell typically runs for $\sim 1 - 2$ s and interceded by a short tumbling interval $\sim 0.1 - 0.2$ s [12]. When the cell moves up an attractant gradient, the chemotaxis network lowers [YP] to lower ϕ_{CW}, so that the cell swims smoothly, persisting in the current direction. When the cell descends an attractant gradient, [YP] rises and high ϕ_{CW} makes the cell tumble more frequently to swim in new directions. Thus the logic of *E. coli*'s chemotaxis response, in short, is: if goes up the attractant gradient→[YP] low→Motor CCW; if goes down the attractant gradient→[YP] high→Motor CW.

This logic, however, as discussed in the last paragraph of Chapter 2, would not benefit *V. alginolyticus*, since instead of run-tumble, *V. alginolyticus* executes the run-reverse-flick cycle and swims when motor rotates in either CCW or CW direction. Rather, for *V. alginolyticus*, a better logic should be: if goes up the attractant gradient→motor persists in the current state; if the cell goes down the attractant gradient→motor reverses. This is applicable to both CW and CCW motor rotations. It thus seems to us that for a microorganism executing the run-reverse-flick motility pattern, modulating switching rates is more advantageous than modulating the rotation bias of the motor. Observation of its chemotactic behavior near a serine-filled micropipette tip in the previous chapter is consistent with this picture, i.e., reversal of the motor always happen when the cell is about to leave the region of high serine concentration.

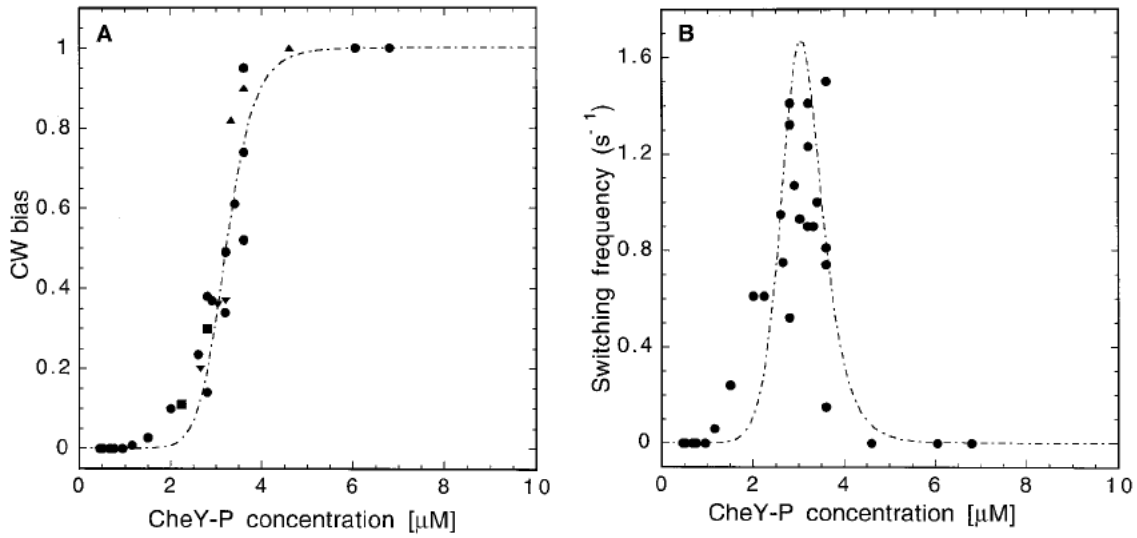

Figure 16: The characteristic response of *E. coli* motors as a function of CheY-P concentration. In (A), each data point describes a simultaneous measurement of the motor bias and the CheY-P concentration in an individual bacterium. Different legends are experimental data obtained from different individual cells. The dashed line shows the best fit obtained with a Hill function Eq. 3.1. (B) Switching frequency measured from the same cells as in (A). The switching frequency was defined as the number of times that a motor switched its direction of rotation divided by the duration of the recording. The dashed line gives the first derivative of the Hill function from (A) with respect to [YP]. This figure is taken from Figure 2 of Ref. [20] and captions are modified to leave out details of the experiments.

For *V. alginolyticus* to modulate the motor's switching rate, it cannot simply inherit the chemotaxis system of *E. coli* and modifications are necessary. There are two possibilities. (i) CheY-P still increases ϕ_{CW} of the flagellar motor, but [YP] is controlled in a different way by the chemotaxis network of *V. alginolyticus*. (ii) [YP] still lowers when the cell goes up an attractant gradient and rises when the cell goes down an attractant gradient, but CheY-P controls the motor of *V. alginolyticus* in a different way.

If scenario (i) is true, in *V. alginolyticus* [YP] must be regulated based on the rotation state of the motor: If the motor is rotating CCW when the cell climbs up the gradient, [YP] should be reduced; if the cell is running up the gradient when the motor is rotating CW, [YP] should be elevated. In this fashion, the cell can move in the favorable direction regardless of the motor rotation state. If [YP] is indeed regulated in this fashion, there must be a feedback mechanism to report the motor rotation state to the chemotaxis network. No such feedback loop has been reported so far in any bacterial chemotaxis network. Moreover, if such a feedback exists, it would require additional chemotaxis protein(s), which is also unknown to us. As a result, we believe that hypothesis (ii) is more plausible.

3.2 BEHAVIOR OF THE FLAGELLAR MOTOR IN *V. ALGINOLYTICUS* AS A FUNCTION OF CHEY-P CONCENTRATION

In a study in 2007 by M. Kojima etc. [40], it was found that *V. alginolyticus* swims forward all the time if its *cheY* gene is deleted, indicating that the motor rotates CCW exclusively in this $\Delta cheY$ mutant. However, when CheY protein is overexpressed, it was reported that the cells "showed more frequent reorientations". Later, when we deleted *cheA* gene, which is necessary to convert CheY into CheY-P, the resulting phenotype is the same as that of the $\Delta cheY$ mutant, namely the motor rotates exclusively CCW. On the other hand, in the wild-type cells, long forward swimming is observed when they are exposed to very high concentration of attractant, while frequent reorientation is observed when they are exposed to 10 mM repellent phenol. These experimental results suggest that in *V. alginolyticus*, attractant stimulation results in low [YP] while repellent stimulation results in high [YP], same as in

E. coli. Consequently, the flagellar motors of *V. alginolyticus* and *E. coli* must respond differently to CheY-P. Compared to *E. coli*, whose CCW rotation interval is shortened but CW rotation interval is lengthened as [YP] increases, *V. alginolyticus* should shorten both CCW and CW rotation intervals as [YP] increases. In other words, higher [YP] results in a higher CW bias in *E. coli*'s flagellar motor but a higher switching rate in *V. alginolyticus*'. We thus hypothesize that the flagellar motor of *V. alginolyticus* behaves like a toggle switch. Similar to the bias switch of *E. coli*, behavior of the toggle switch is also affected by CheY-P binding, but instead of biasing the switch into CW state, more CheY-P binding results in more frequent flip between CCW and CW states. Below, we attempt to verify whether this picture is correct by measuring the switching rate of the polar flagellar motor in *V. alginolyticus* as a function of [YP] inside the cell.

My adviser and I spent the last two years learning molecular biological techniques to knock out chromosomal genes in *V. alginolyticus*. To date, a whole set of *che*-gene mutants is nearly completed. In this experiment we used the mutant strain YM4-Δ*cheY*. This strain is constructed by deleting *cheY* gene from the genome of the *V. alginolyticus* strain YM4, which is considered wild type. The *cheY* gene was then placed under control of a *lac* promoter on a plasmid so that its expression level can be modulated by adding different amount of the inducer IPTG to the growth medium. The CheY protein concentration inside the cell increases as the induction level increases, and its effect on the motor can then be assessed by recording motor switching events in individual cells and in a population by video microscopy.

To estimate the expression level of CheY, the gene of the fluorescent protein Venus was inserted downstream of *cheY*. *cheY* and *Venus* genes are transcribed together so that even though the CheY and Venus proteins are translated separately, their expression levels should be proportional, i.e., $[\mathrm{Y}] \propto I$, where [Y] is the concentration of CheY and I is the fluorescence intensity of the cell. Unfortunately, no technique is currently available to measure the concentration of CheY-P, denoted as [YP]. However, based on what we know about *E. coli*'s chemotaxis network, it is reasonable to assume that [YP] is proportional to [Y]. Since $[\mathrm{Y}] \propto I$, we assume $[\mathrm{YP}] = y_0 I$, where y_0 is a constant. At each induction level, average [YP] over a population of cells is represented by the fluorescence intensity I measured from 3 mL bacte-

rial culture in a fluorometer (see Materials and Methods for details). Since a *V. alginolyticus* cell alternates between forward and backward swimming, there are two switching rates, k_f and k_b, which are the rates at which the motor switches from CCW to CW rotation, and from CW to CCW rotation, respectively. For an individual cell, under the approximation that the motor switches from CCW to CW in a Poissonian fashion, k_f can be calculated as $k_f = 1/\langle \Delta_f \rangle$, where $\langle \Delta_f \rangle$ is the average of Δ_f measured in this cell. In our experiment, this average is obtained from up to five Δ_fs (more details in Materials and Methods). k_b for an individual cell is obtained in the same way. Corresponding to each [YP], or each I, k_f and k_b from 20 cells were measured and the results are presented in Figure 17.

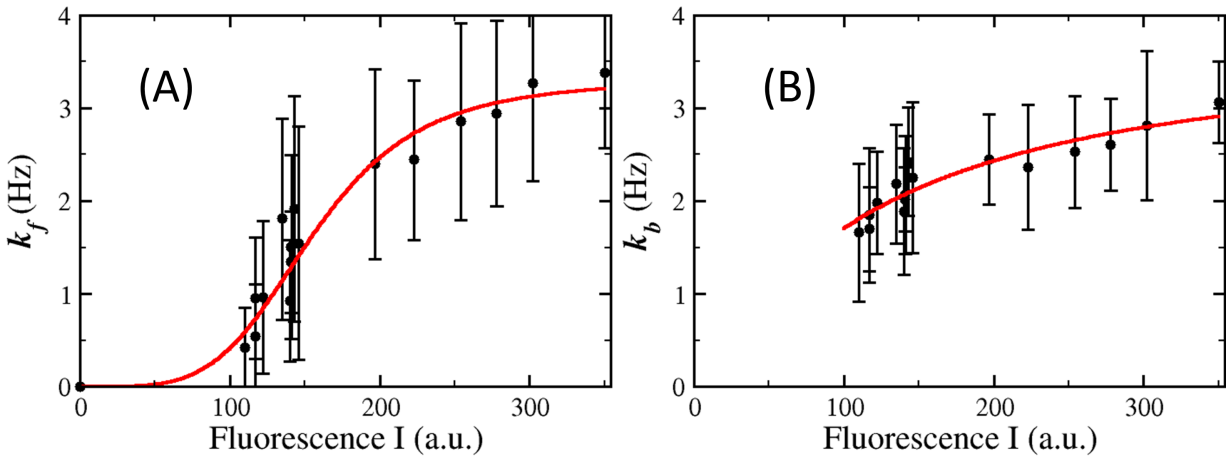

Figure 17: The forward and backward switching rates, k_f and k_b, as a function of fluorescence intensity I. For each I, 20 k_f were measured from 20 cells. The mean and standard deviation of these 20 measured values were represented by the dot and error bars respectively in (A). k_b as a function of I is presented in the same fashion in (B). For YM4-Δ*cheY*, [YP]=0 and $I = 0$, $k_f = 0$ since cells swim forward exclusively. This is represented by the dot at the origin in (A). Correspondingly, k_b is taken to be ∞ and not presented in (B). For small $I \to 100$, instead of approaching 0, as k_f does, k_b stays above 1.5 Hz. The red lines are fittings to the Hill function.

Despite the large uncertainty, it is evident that the curves in Figure 17 are qualitatively different from that in Figure 16(B), since as the expression level of *cheY* gene increases, both

k_f and k_b increases. However, we found that the motor bias also increases as [Y], or [YP] increases. At $I = 0$, corresponding to [YP]=0, $k_f = 0$ and all cells swim forward smoothly without reversing, as observed in Ref. [40]. Thus the CCW and CW rotation of the motor are not strictly equivalent, and the CCW is the default state of the motor in the absence of CheY-P, so that $\phi_{CW}([YP] = 0) = 0$. At low induction level, the forward duration Δ_f can be as long as tens of seconds while the backward duration Δ_b are relatively short and rarely exceeds 2 seconds. Thus at low [YP], $\phi_{CW} \ll 1$. At a high induction level, Δ_f and Δ_b both become shorter with $\Delta_f \approx \Delta_b$ so that ϕ_{CW} approaches 0.5, which is shown in Figure 18. This dependence of ϕ_{CW} on [YP] is due to the asymmetry between forward and backward swimming, where the former is favored or a default state. This asymmetry is also reflected in the fluctuations of Δ_f and Δ_b. Compared to Δ_f or k_f, the fluctuations in Δ_b or k_b are significantly smaller as indicated by the smaller error bars in Figure 17(B). This is particularly true at low [YP]. In the experiment where no IPTG was added and *cheY* was expressed at a low base level, $P(\Delta_f)$ is much broader than $P(\Delta_b)$ and the standard deviation of Δ_b is about 6 times smaller than that of Δ_f. Also for the same cell, Δ_f can vary from a fraction of a second to tens of seconds, while Δ_b rarely gets above 2 seconds. As [YP] increases, fluctuation in both k_f and k_b becomes smaller, and the forward and backward swimming intervals become more alike. In wild type cells, as shown in Figure 10, $P(\Delta_f)$ and $P(\Delta_b)$ have similar shapes when they are in the homogeneous motility buffer. As [YP] increases when phenol is added to the medium, $P(\Delta_f)$ and $P(\Delta_b)$ become narrower but their shapes are still conserved.

Similar to Eq. 3.1, k_f and k_b can be fitted with the Hill function, as

$$k(I) = k([YP]/y_0) = k_{max}\frac{1}{1 + (\frac{K_m}{y_0 I})^H} \tag{3.2}$$

For k_f, it was found that $k_{max} = 3.30\pm0.26$ Hz, $K_m/y_0 = 156.4\pm10.3$ and $H = 4.38\pm0.92$ while for k_b, $k_{max} = 3.70 \pm 1.49$ Hz, $K_m/y_0 = 115.2 \pm 75.4$ and $H = 1.17 \pm 0.88$ as shown by the red lines in Figure 17. First, the Hill coefficient for k_f is much larger than that for k_b, indicating that when the motor is rotating CCW, it is more sensitive to [YP] fluctuations. Second, k_{max}, which is the mean asymptotic switching rate, is about the same for k_f and k_b. Thus at high [YP], the CCW and CW rotations of the motor are symmetric, as observed

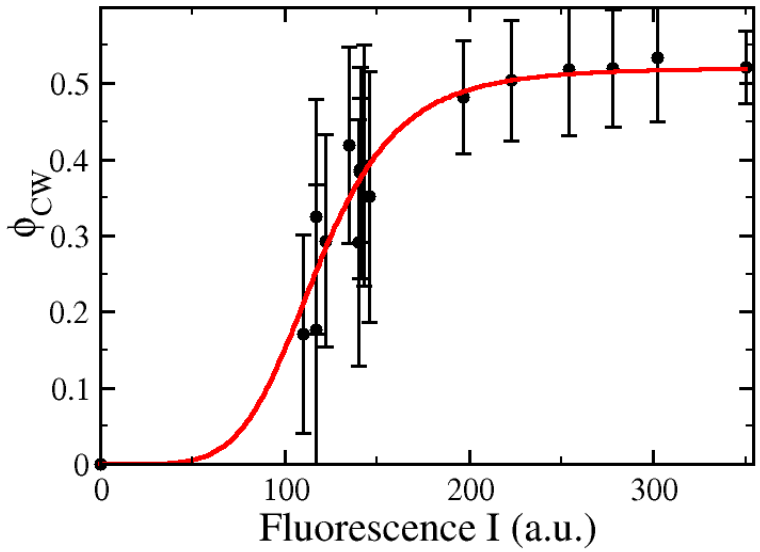

Figure 18: The CW bias ϕ_{CW} vs. the fluorescence intensity I. The mean and standard deviation of CW bias calculated from 20 cells at each I are displayed. The red curve is the fitting using the Hill function.

when wild-type YM4 cells are exposed to 10 mM phenol. We note that the result presented in Figure 17 is obtained from an ensemble of cells, yielding the H value that can be significantly lower than if H is measured in individual cells. For *E. coli*, the H value for an ensemble of cells was 3.5-5.5 [62] whereas in individual cells, H was found to be ˜10 [20]. In the experiment with a high induction level, we sometimes observed cells switching at a frequency as high as ˜5-6 Hz, but the asymptotic k_{max} is less than 4 Hz. It is thus possible that the flagellar motor of *V. alginolyticus* is also very sensitive, but further investigation requires a better technique enabling observing individual cells for a long time.

To factor out cell-to-cell variations in [YP] and to better illustrate the correlation between k_f and k_b, (k_f, k_b) pairs measured from ˜300 individual cells at different induction levels are plotted in Figure 19. It is evident that k_b is positively correlated with k_f and the correlation coefficient c can be calculated as

$$c = \frac{\sum_i (k_{f,i} - \overline{k_{f,i}})(k_{b,i} - \overline{k_{b,i}})}{\sqrt{\sum_i (k_{f,i} - \overline{k_{f,i}})^2}\sqrt{\sum_i (k_{b,i} - \overline{k_{b,i}})^2}} = 0.63,$$

where $\sum_i$ is the summation over all (k_f, k_b) pairs with a finite k_b. In contrast to the positive correlation between k_f and k_b of *V. alginolyticus*' flagellar motor, in *E. coli* k_b decreases as k_f increases, as shown in Figure 19 by the green line. Thus the flagellar motors of *E. coli* and *V. alginolyticus* are regulated by CheY-P very differently. Although both motors behave similarly at low [YP] because the default state for both are CCW, the contrast between their behavior becomes more prominent at high [YP]. For *E. coli* motor, $\phi_{CW} = 1$ while the switching rate from CW to CCW goes to zero. For *V. alginolyticus* motor the switching rate approaches maximum while ϕ_{CW} is held at a constant ~ 0.5.

Interestingly, ϕ_{CW} shows a similar dependence on I as k_f and k_b and $\phi_{CW}([YP])$ can also be characterized by the Hill function

$$\phi_{CW}(I) = \phi_{CW}(y_0[YP]) = \phi_0 \frac{1}{1 + (\frac{K_m}{y_0 I})^H} \tag{3.3}$$

where $\phi_0 = 0.52 \pm 0.01$, $K_m/y_0 = 118.5 \pm 3.1$ and $H = 5.42 \pm 1.07$. Compared with $k([YP])$, $\phi_{CW}([YP])$ has an even larger Hill coefficient, indicating that the bias is more sensitive to [YP] than the switching rates does. In Chapter 2, $P(\Delta_f)$ and $P(\Delta_b)$ were

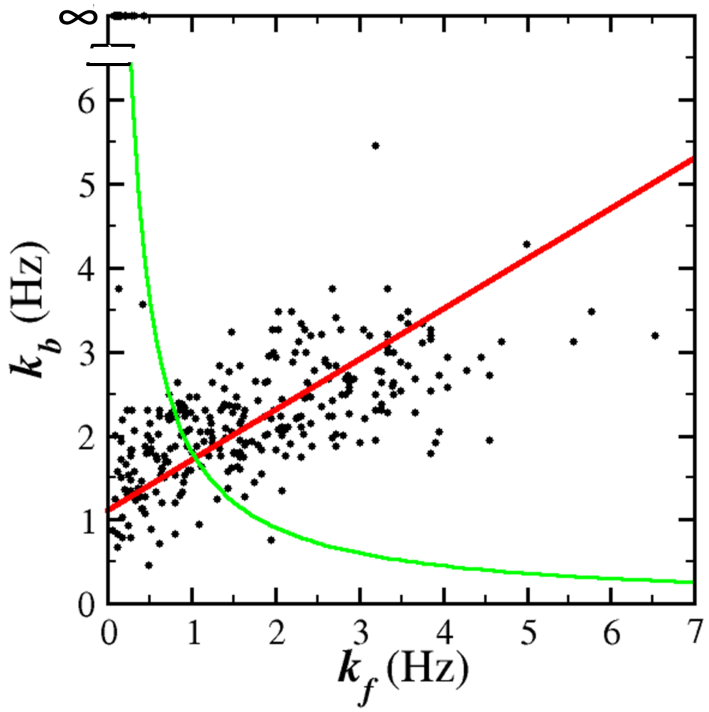

Figure 19: The scatter plot of k_b vs. k_f from ˜300 cells expressing different amount of CheY protein or with different [YP]. At low I, some cells swim froward all the time so that $k_b = 1/\Delta_b = \infty$. The red line is $k_b = 0.6k_f + 1.1$ Hz. The green line is the measured k_b vs. k_f for *E. coli* adapted from Figure 11 of Ref. [42], where it was found that $k_f \cdot k_b = 1.82$

measured for the wild type *V. alginolyticus,* and it was found that over the ensemble, $\tau_f (\equiv \langle \Delta_f \rangle) \simeq 0.5$ s and $\tau_b (\equiv \langle \Delta_b \rangle) \simeq 0.47$ s. This yields $k_f \approx 2$ Hz, $k_b \approx 2.1$ Hz, $\phi_{CW} \approx 0.48$ and corresponds to $[YP] \approx 175 y_0$ as shown in Figure 18. When the cell is exposed to repellents, such as phenol, [YP] increases so that both τ_f and τ_b decreases while $\tau_b \approx \tau_f$. When the cell detects attractant, [YP] drops and both k_f and k_b drops. However, as shown in Figure 17, the range of variation of k_b is much smaller than that of k_f. If [YP] is in the vicinity of $[YP] \approx 175 y_0$, $\tau_b \approx \tau_f$ still holds. If [YP] drops further to $[YP] \approx 120 y_0$, which happens when the cell is climbing up a steep attractant gradient or when the attractant concentration around the cell is very high, $\tau_f \gg \tau_b$. It seems that *V. alginolyticus* do extend τ_b so that it can move toward the area with higher concentration of attractant, as observed in Figure 15 where the cell is exposed to a serine gradient created by a point source. However, when it needs to migrate over a long distance, forward swimming is preferred.

From the physiology point of view, forward swimming is more advantageous than backward swimming, since the flagella of two backward swimming cells are more likely to get entangled as shown in Figure 20. When the cell swims backward, the flagellum pulls at the cell body and this force is balanced by the drag on the cell body, corresponding to a force dipole in which the flagellum and the cell body act on the fluid in the direction toward the cell, which is represented by two arrows pointing toward a dot in Figure 20(A). When two such dipoles are close to each other as shown in 20(B), they are attracted to each other. As they move toward each other and their CW-rotating left-handed helical flagella thread through each other, they become tied up together. With a mutant strain NMB102 that always swims backward [37], not only did we find cell pairs like Figure 20(E), we also observed a lot of bundles containing more than two cells, indicating that multiple bacteria can get entangled together. The more bacteria get tied together when they swim backward, the more complicated this flagellar knot becomes and it is more difficult for them to detach when their motors switch into CCW rotation.

When a cell powered by a helical polar flagellum is swimming backward, it is like a screw being driven into a medium. Thus in general a backward-swimming cell is more likely to get caught into a mesh, regardless of the chirality of the flagellum. This might be the reason why forward swimming is favored over backward swimming for long distance migrations so that

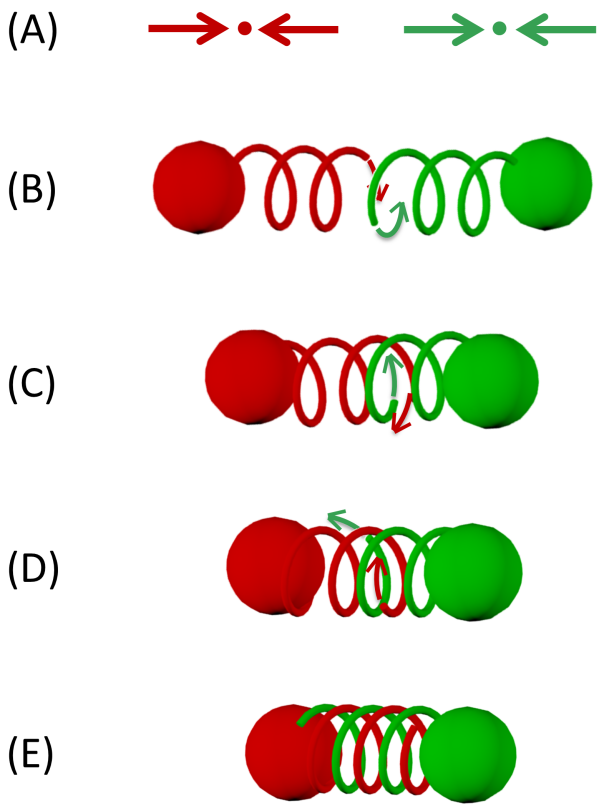

Figure 20: The flagella of two backward-swimming cells get intertwined together. (A) two force dipoles corresponding to the flow field generated by two backward-swimming cells. When such two cells are close to each other like in (B), their CW-rotating, left-handed helical flagella thread through each other as depicted in (B-D), and the two cells become interlocked.

the cell does not get trapped by its own flagellum. Besides *V. alginolyticus*, the motility patterns of other bacteria that are driven by a single flagellum were also characterized. The bacterium *Pseudomonas citronellolis* has a single polar left-handed flagellum, similar to *V. alginolyticus*. Its motility pattern consists of forward runs followed by a brief reversal to change the swimming direction. When the bacterium experienced a sudden increase in attractant concentration, the flagellar motor biased toward CCW rotation so it swims forward for a long time without reversal [72]. The bacterium *Rhodobacter sphaeroides* has a single right-handed lateral flagellum which is driven by a motor that rotates exclusively in the CW direction. It carries out the run-stop motility pattern and the cell orientation is altered by rotational diffusion during the stop phase. During the run, the motility of the cell is generated by a pushing flagellum so the cell runs forward [7]. Although motility patterns of other bacteria are not well characterized, it seems that in most bacteria forward runs pushed by flagella are favored over the backward runs pulled by flagella, regardless of the default rotation state of the motor.

3.3 FLUCTUATION ANALYSIS OF THE ROTATION OF THE MOTOR SWITCH

The most extensively studied flagellar motor of *E. coli* is a very delicate nano-machine consisting of a stator and a rotor. The stator anchors to the cell wall and utilizes the proton flux to generate torque to rotate the rotor, which is a set of rings up to 45 nm in diameter. One end of the rotor is connected to the flagellar filament by a flexible hook and power the flagellum to rotate in the same direction as itself; the other end is called the switch complex, which upon binding and unbinding of CheY-P controls the rotation direction of the motor. The switch complex consists of $\sim$ 35 FliM and $\sim$140 FliN proteins. Every one FliM and four FliN proteins make up a motor switch subunit and these 35 subunits form a ring, as shown in Figure 21(A). Each subunit exists in two distinct conformations, active and inactive. CheY-P controls the motor direction by binding to these subunits as shown in Figure 21(B), biasing them toward the active conformation. It is believed that all 35

subunits are able to switch between these two conformations coherently, so that when all of them are active (or inactive), the motor rotates CW (or CCW), as seen in Figure 21(C) [61].

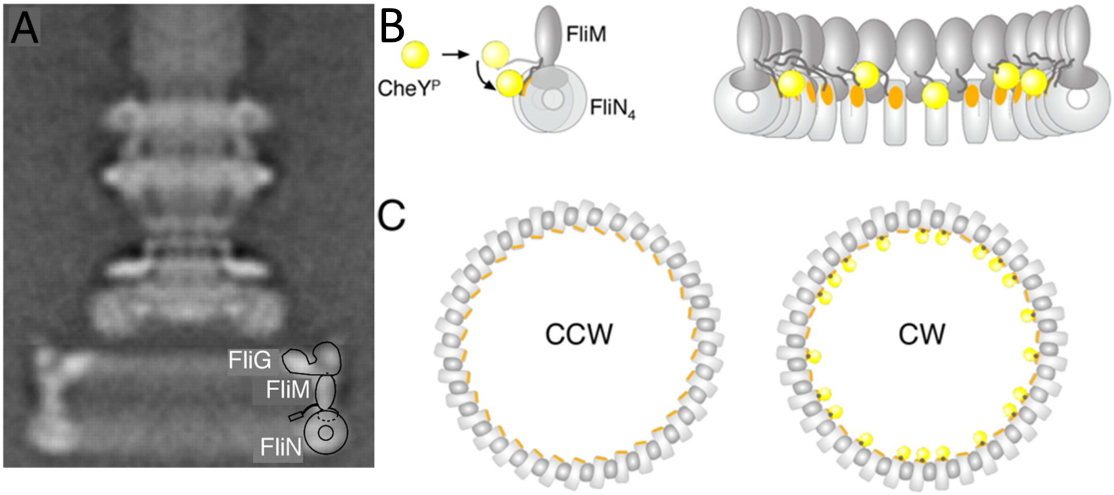

Figure 21: Structure of the flagellar motor of *E. coli*. (A) Electron microscopic images of the flagellar basal body. A current working hypothesis for the locations of FliG, FliM, and FliN is shown. The inward-pointing extension on FliM represents the N-terminal segment that is known to interact with CheY-P. (B) (Left) Model of CheY-P-induced flagellar motor switching. CheY-P (yellow) interacts initially with the N-terminal segment of FliM, subsequently binds to a site on FliN (orange). (Right) A view showing multiple FliM-FliN subunits forming a ring, and the binding of multiple CheY-P molecules. (C) Hypothesis for switching in all of the subunits, shown in top view. CheY-P molecules are yellow and binding sites are orange; the black dot signifies the N-terminal segment of FliM sandwiched between CheY-P and FliN. This figure is reproduced from Ref. [61]; (A) is from Figure 1, and (B, C) are from Figure 5.

As can be expected from the structure shown in Figure 21, switching of the motor between CCW and CW is highly stochastic. Besides fluctuations in [YP], molecular events such as binding and unbinding of CheY-P to the subunits and conformational change of each subunit are always subject to thermal fluctuations. As a result, unlike a man-made motor, the bacterial flagellar motor switch is noisy and requires a large amount of sampling in any measurement. Statistical fluctuations, on one hand complicate the analysis but on the other

hand can reveal useful information about the underlying microscopic process that might not be able to be studied directly.

Since the motor alternates between CCW and CW rotations, the simplest description is the two-state model where the motor switches between the states stochastically in a Poisson fashion. This process can be described by two constants, k_{CCW} and k_{CW}, which are the rates at which the motor exit CCW or CW rotation state, respectively (k_{CCW} and k_{CW} are thus equivalent to k_f and k_b in the previous section). This model describes the switching behavior of *E. coli*'s flagellar motor very well in several experiments, where both rotating durations Δ_{CCW} and Δ_{CW} are found to be exponentially distributed [42, 62]. However for *V. alginolyticus*, as seen in Chapter 2 Figure 10, $P(\Delta_f)$ and $P(\Delta_b)$ constructed from ~1000 (Δ_f, Δ_b) pairs collected from ~800 bacteria have peaks at ~0.3 second. Deviations of the PDFs from exponential distribution indicates that the switching process between CCW and CW states are not only driven by thermal fluctuations. Since this is an ensemble measurement, it is possible that the peaks are due to variability among the cells. We then tracked 5 bacteria each for ~10 mins to study the behavior of individual motors. However, due to technical reasons, this set of measurements is performed with a camera running at 24 frames per second, resulting in a lower resolution of the motor switching moments. Thus before constructing $P(\Delta_f)$ and $P(\Delta_b)$, we tried to test the two-state model by counting statistics, which is commonly employed in the study of quantum particles [30]. In those experiments, a simple measurement of the particle arrival times at a detector can yield surprisingly rich information about the quantum nature of the particles. If the particle arrival events are bunched together, they are bosons; if the events are anti-bunched, they are fermions and if the events are Poissonian, the particles are independent and non-interacting. For a homogeneous Poisson process where events happen at a constant rate k, the probability that n events happen in time interval T is

$$P(n,T) = \frac{(kT)^n}{n!}\exp(-kT)$$

It is easy to show that the mean N and variance σ^2 of the number of events happened during time interval T are both kT, yielding the Fano factor, defined as $F = \sigma^2/N$, to be unity. If the particles are bosons and the arrival events are bunched, the Fano factor is

larger than 1 while for anti-bunched fermions, the Fano factor is smaller than 1. A significant advantage of this approach over constructing the PDFs of waiting times between two arrivals is that it doesn't require accurate determination of particle arrival moments, since only the number of events happened during a time interval matters.

Taking each motor reversal as a particle arrival event, we can use the same approach to see if the switching events happen in a Poisson fashion. If the CCW-to-CW and CW-to-CCW reversals of the motor happen alternatively at constant rates k_{CCW} and k_{CW}, it can be shown that for $T \gg 1/k_{CCW}$ and $1/k_{CW}$, the Fano factor $1 \leq F = 2(k_{CCW}^2 + k_{CCW}^2)/(k_{CCW} + k_{CW})^2 < 2$. To measure the Fano factor of the switching events of individual *V. alginolyticus*' motor, each 10-minute track is segmented into consecutive intervals of length T. Numbers of motor reversals during each intervals were counted to compute $\sigma^2(T)$ and $N(T)$. In Figure 22 we plot $\sigma^2(T)$ vs. $N(T)$ and the Fano factors for all five cells are below 1, which is indicated by the black dashed line. This proves that the motor switching cannot be described by Poisson processes. There might be correlations between consecutive switching events, or at least one of $P(\Delta_{CCW})$ and $P(\Delta_{CW})$ is not exponential, or both. Below we investigate in detail the distribution of the dwell time, $P(\Delta_{CCW})$ and $P(\Delta_{CW})$ (or equivalently $P(\Delta_f)$ and $P(\Delta_b)$).

3.3.1 $P(\Delta_f)$ and $P(\Delta_b)$ measured in *V. alginolyticus* are not exponential

Motivated by the above observation of the Fano factor, we studied $P(\Delta_f)$ and $P(\Delta_b)$ in a more detailed and systematic way. First, we obtained more statistics of Δ_f and Δ_b for wild type cells in swimming buffer TMN, in absence of chemical stimulants. From the 5 long tracks used for counting statistics above, $P(\Delta_f)$ and $P(\Delta_b)$ for individual cells over a long period of measurement time are constructed and presented using different colored symbols in Figure 23, where their average is delineated by the green lines. $P(\Delta_f)$ and $P(\Delta_b)$ are also constructed from ~5000 Δ_f and Δ_b collected from ~2000 cells, and shown in Figure 23 by black lines. As can be seen, ensemble PDFs constructed from ~5000 data points is qualitatively the same as those constructed from ~1000 data points as seen in Chapter 2. Also different sets of data are in good agreement with each other, indicating that the temporal

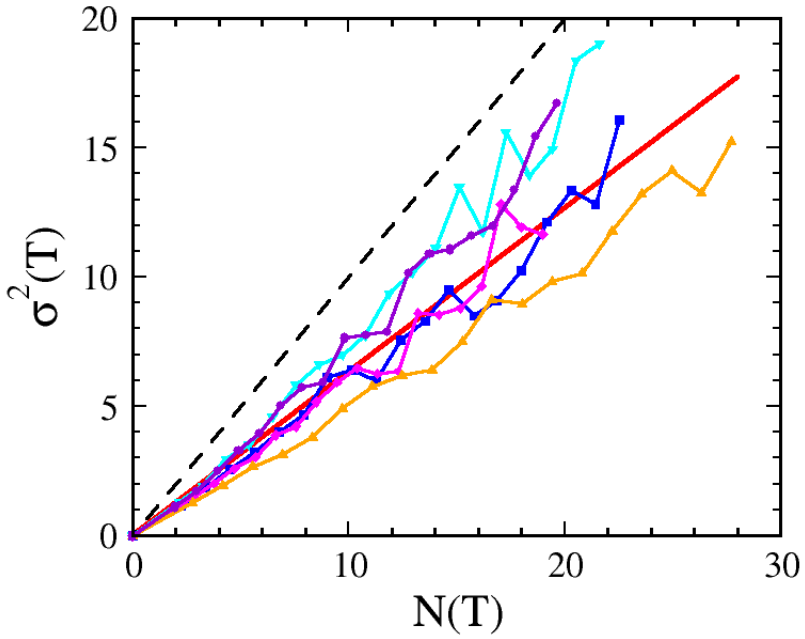

Figure 22: σ^2 vs. N for five long bacterial trajectories. The data from the five bacteria are represented by purple dots (cell #1), blue squares (cell #2), magenta diamonds (cell #3), orange triangles (cell #4), and cyan inverted triangles (cell #5). The dashed black line corresponds to $\sigma^2/N = 1$. Assuming that σ^2 vs. N is linear, a linear regression using the data from the five cells yields a straight line with a slope (or Fano factor) of 0.63, which is represented by the red line.

average of individual bacterium and the ensemble average of many bacteria are qualitatively the same in this marine species. For all PDFs, instead of decreasing monotonically, they peak at ˜0.3 second before decaying exponentially. The tails of both $P(\Delta_f)$ and $P(\Delta_b)$ can be fit by exponential functions as evident in the semilog plots of Figure 23. Also, the peak position for $P(\Delta_f)$ is always smaller than that of $P(\Delta_b)$, suggesting that a forward swimming bacterium is more readily to switch direction than its backward counterpart.

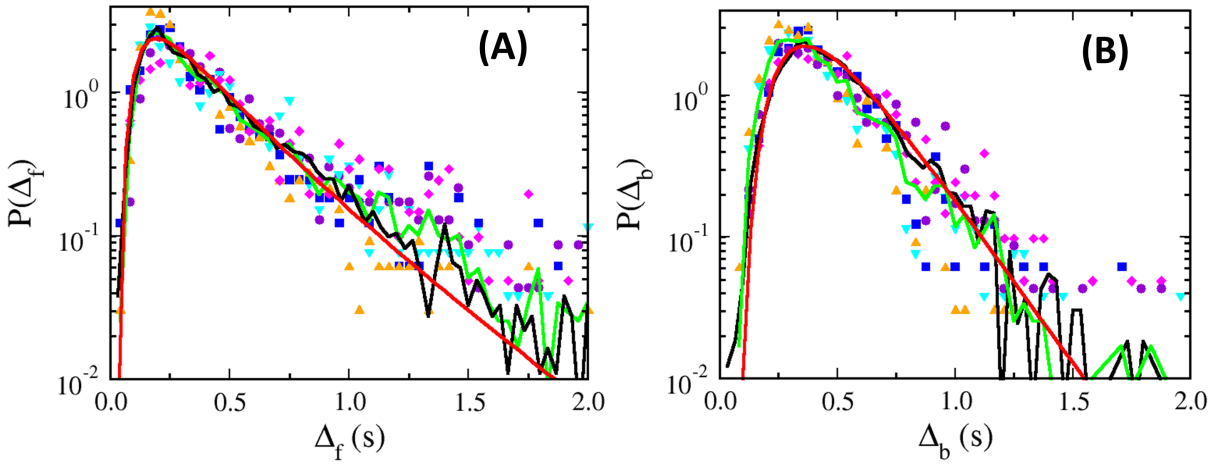

Figure 23: (A) $P(\Delta_f)$ and (B) $P(\Delta_b)$ of YM4 in TMN. The data collected from five cells (#1-5), each tracked for 10 min, are plotted using the same color scheme as in Figure 22. The averages resulting from the five cells are plotted by the green lines. The ensemble PDFs are plotted by the black lines. We fit the ensemble averaged data using the inverse Gaussian distribution (see text for details), and the fitting results are presented by the red curves.

Besides the PDFs measured from wild type cells, we also studied the dwell time statistics under three different CheY concentration. For low CheY concentrations, corresponding to average $k_f \sim 0.5$ Hz and average $k_b \sim 1.5$ Hz, we collected ˜800 Δ_f and Δ_b to construct the PDFs as shown in Figure 24(A, B). At medium CheY expression level, the average k_f, $k_b \sim 2$ Hz, comparable to the switching rates of the wild type cell in the homogeneous motility buffer TMN. The measured PDFs in Figure 24(C, D) are very similar to those in Figure 23. With the highest induction, k_f and k_b go beyond 3 Hz, similar to what we observed when there is 10 mM phenol in the swimming buffer and the PDFs shift even more toward small times, as

shown in Figure 24(E, F).

While $P(\Delta_b)$ doesn't vary much at different CheY concentration, $P(\Delta_f)$ changes significantly. At a low CheY expression level, $P(\Delta_f)$ has a very fat tail since a lot of cells go forward most of the time and some swims forward exclusively. At high induction, the PDF is much narrower and decay much more sharply at large times. This is consistent with the measurement of k_f and k_b, where k_f is a lot more sensitive to changes in CheY concentration than k_b is. Comparing the PDFs measured in wild type cells and in cells whose CheY concentration are set at different values, features observed in Figure 23 are similar to Figure 24: all the PDFs peak at a finite value before decay exponentially. Moreover, $P(\Delta_f)$ always peak at a slightly smaller time than $P(\Delta_b)$ does.

In an effort to construct a model to interpret all these PDFs we measured in *V. alginolyticus*, which are quantitatively different from those measured in *E. coli*, we first sought for a distribution function that can be applied to all the data. Among different non-monotonic distribution functions, we found that the inverse Gaussian distribution fits all our data very well, as evident in Figure 23 and Figure 24, and even for $P(\Delta_f)$ measured under a low CheY concentration, resulting in a PDF whose shape is distinct from others. Below we try to derive a microscopic model inspired by the inverse Gaussian distribution, which appears to have been first derived by Schrodinger in 1915 as the first passage time of a Brownian motion.

3.3.2 Modeling the motor switch of *V. alginolyticus*

A reasonable motor switch model for *V. alginolyticus* should be consistent with most of the knowledge learned in *E. coli* since majority of chemotaxis and motor proteins are conserved between these two species. However, since the motor of *V. alginolyticus* responds very differently when CheY concentration is varied, as shown in Figure 19, the model from *E. coli* will be modified to a minimal extent to be adapted to the *V. alginolyticus* system.

3.3.2.1 Model for *E. coli*'s flagellar motor switch The motor switch in *E. coli* exhibits two novel properties. First, despite thermal noise, all 35 subunits can switch collectively between two conformations, so that the motor can switch rotation direction rapidly.

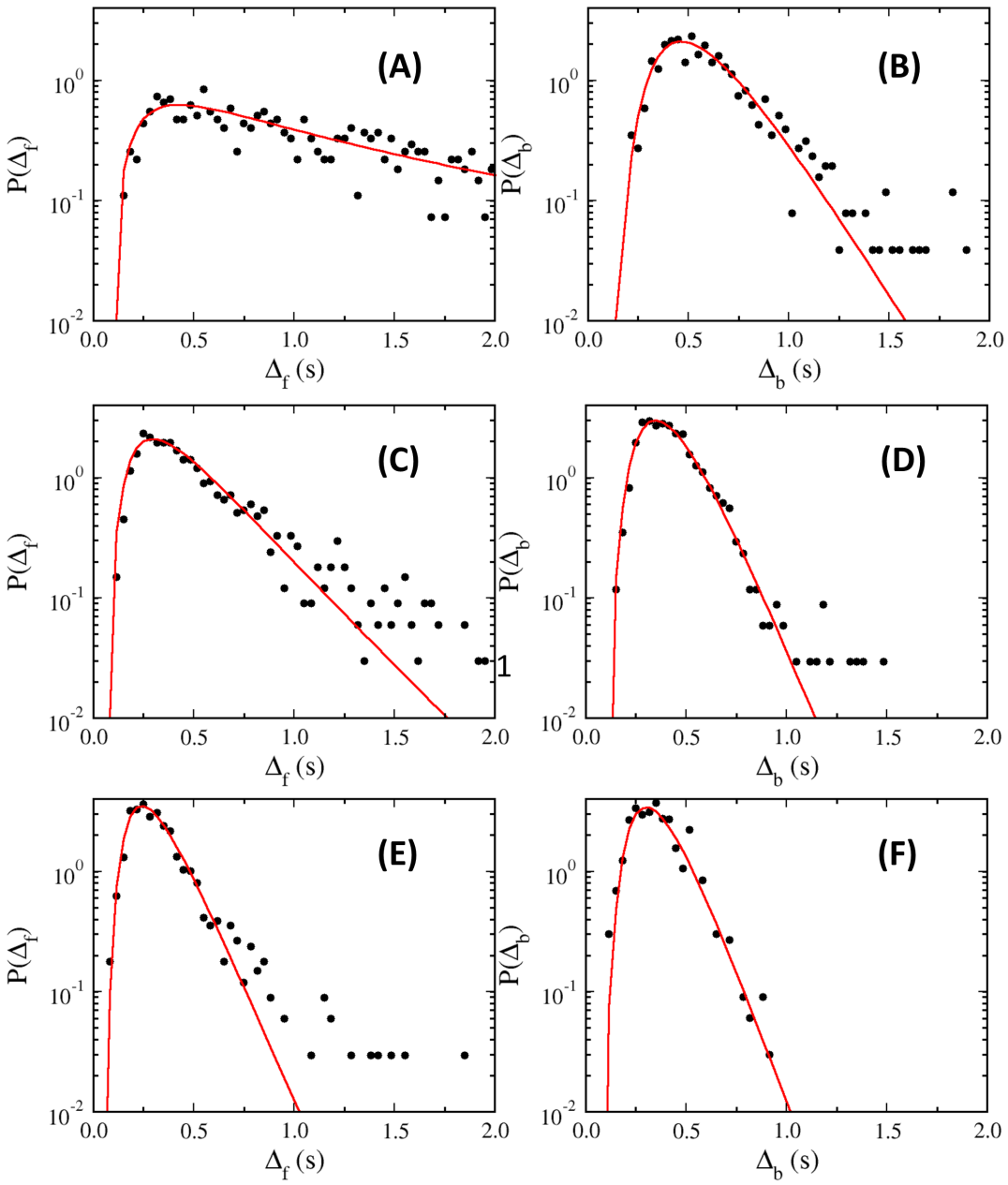

Figure 24: $P(\Delta_f)$ and $P(\Delta_b)$ obtained from an ensemble of cells where CheY was expressed at low (A, B), medium (C, D) and high (E, F) levels. The black dots are the measured data and the red curves are fittings using inverse Gaussian using parameters listed in Table 2. The scales of all PDFs are the same for easy comparison.

Second, this switch is ultra sensitive to the CheY-P concentration and ϕ_{CW} rises from 0 to 1 sharply during a very narrow range of [YP], as shown in Figure 16. These two properties are also observed in other biochemistry systems consisted of identical subunits, where each subunit, usually referred to as a protomer, can have two different conformations. For example, the chemoreceptors, instead of operating as independent units, usually cluster at cell poles to form an array. By interacting with each other, chemical signals get significantly amplified [16]. Cooperativity is thus a very important ingredient of a model that can explain both coherence and sensitivity of the motor switch. Since the motor switch ring has two conformations, and the binding of CheY-P makes the CW conformation favorable, this system can be very well mapped to the one-dimensional random field Ising ring model, in which cooperativity can be accounted for by the coupling between adjacent spins. In this model the conformation of a protomer corresponds to the state of a spin s_i and binding of CheY-P acts like a random magnetic field B_i. Taking $k_BT = 1$, the Hamiltonian can be written down as

$$H = \frac{1}{2}\sum_{i=1}^{N_0=35} -E_J s_i s_{i+1} - E_A B_i s_i - E_L B_i \tag{3.4}$$

where the spin $s_i = 1(-1)$ denotes the conformation of the single protomer, active or inactive; the random magnetic field $B_i = 1(-1)$ indicates whether a CheY-P protein binds or not [24]. The first term in Eq. 3.4 accounts for the cooperativity between protomers. The second term indicates that binding of CheY-P to a protomer stabilizes its active conformation and destabilizes the inactive conformation. The last term indicates that the fraction of protomers bound by CheY-P depends on CheY-P concentration [YP]. Here, $E_L = \ln([YP]/K_D)$ can be interpreted as the chemical potential, where K_D is a dissociation constant. This term does not exist in a standard Ising model but under the physiological condition, [YP] fluctuates around K_D so that E_L can be assumed to be 0. Although the kinetics of this model is difficult to be studied analytically, H can be significantly simplified under the condition that $E_J \gg 1$. In this case, the protomer ring can only exist in two conformations, $s = 1$ or $s = -1$ so the number of energy states of the system reduces to $2N_0$ and each states can be characterized by two parameters $\{s, n\}$, where n is the number of CheY-P binding to the ring. This assumption also ignores the conformation fluctuation on the ring due to finite E_J

so that transition between $s = \pm 1$ can be described by a rate constant. If the binding and unbinding of CheY-P are Poisson processes, the system can be delineated by Figure 25 (A).

In short, if the motor switch is in any state $\{s, n\}$, it can either transit into $\{s, n+1\}$ state at a rate $k_+(s,n)$, or into $\{s, n-1\}$ at a rate $k_-(s,n)$, or into $\{-s, n\}$ at a rate $\omega(s,n)$. At a steady state, if the system operates at equilibrium and detailed balance is satisfied, the system is driven by thermo fluctuations and there is no energy dissipation. It can be proved that the PDF of the dwell times, $P(\Delta_{CCW})$ and $P(\Delta_{CW})$ (or equivalently $P(\Delta_f)$ and $P(\Delta_b)$), should be monotonically decaying as a sum of exponential functions. This prediction is consistent with the measurement in Ref. [62, 42]. In Ref. [24], a Monte-Carlo simulation is carried out using Eq. 3.4 with $E_L = 0$, $E_A = 1$ and $E_J = 4$. When the conformational switching frequency of a single protomer is $\sim 10^4$ Hz, the CheY-P binding and unbinding frequency is ~ 10 Hz, the simulation output indeed agrees the experimental results very well.

3.3.2.2 A plausible model for the motor switch of *V. alginolyticus* Similar to *E. coli*, the conformational change of the motor switch of *V. alginolyticus* is controlled by the signal molecule CheY-P through binding and unbinding, and the kinetics should be determined by E_L. Also, the protomers interact with each other so that all of them can change conformations in concert. Applying the same simplification that all protomers are of the same conformation due to large E_J, there are only $2N_0$ states for the motor switch of *V. alginolyticus*. However, the second term in Eq. 3.4, which adjusts the relative energy difference between the two conformations of the motor switch in *E. coli*, is not valid in *V. alginolyticus*. In the marine bacterium, instead of stabilizing the active conformation and destabilizing the inactive conformation, binding of CheY-P *destabilizes* both active and inactive conformations of the protomers. CheY-P thus lowers the energy barrier between these two states. Also, since the measured $P(\Delta_{CCW})$ and $P(\Delta_{CW})$ is non-monotonic as shown in Figure 23-24, irreversibility needs to be introduced to break the detailed balance among states. The model therefore requires energy dissipation to keep the system away from equilibrium at the steady state [59].

Since the PDFs of $P(\Delta_f)$ and $P(\Delta_b)$ can be very well described by the inverse Gaussian distribution, we tried to relate the motion of a Brownian particle under a constant external

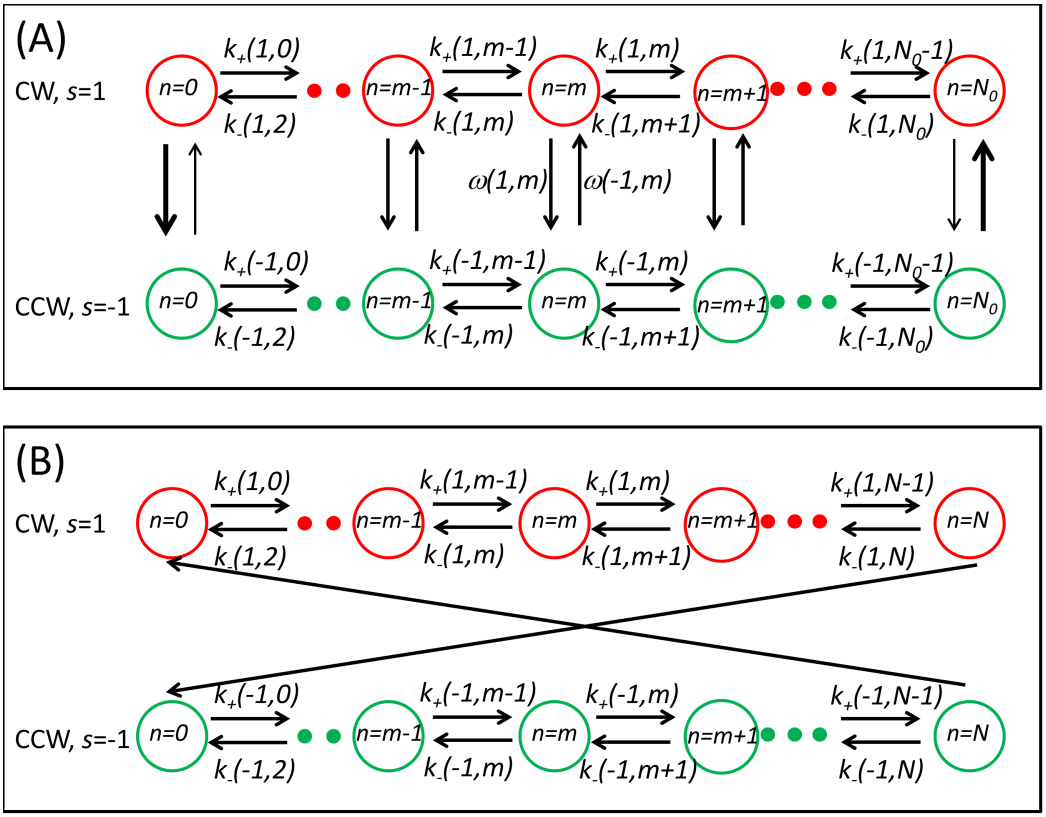

Figure 25: The kinetic model of the motor switch of (A) *E. coli* and (B) *V. alginolyticus*. Each circle represents a state of the motor, described by s, the rotation direction and n, number of CheY-P binding to the motor switch. To simplify Eq. 3.5 which describes the motor switch of *V. alginolyticus*, it is assumed that $k_{\pm}(s, n)$ are independent of n. Also note that in the model for *V. alginolyticus*, transitions from {1, N} to {-1, 0} and from {-1, N} to {1, 0} are irreversible.

force to the transitions of the system through different states driven by the chemical potential from [YP]. In short, to trigger a motor reversal, CheY-P binds and unbinds stochastically to the switch ring until a certain critical number is reached. Once this happens, the motor reverses its direction along with the dissociation of all CheY-P molecules, and a new rotation state ensues as depicted in Figure 25(B). In this model, CheY-P binding and unbinding are determined by the chemical potential, or E_L, similar to the model for *E. coli*. However, here binding of CheY-P lowers the energy barrier between two conformations so that once the barrier is below a critical threshold, the transition occurs irreversibly.

Phenomenologically, we model the above dynamic process using a one-dimensional adsorption model. When the motor switch is in one of the conformations s, let $p_n(t)$ be the probability that n CheY-P occupy the ring of length N_0 at time t. The master equation for $p_n(t)$ is given by,

$$\frac{dp_n(t)}{dt} = k_+ p_{n-1}(t) + k_- p_{n+1}(t) - (k_+ + k_-)p_n(t), \tag{3.5}$$

where k_+ and k_- are rates of adding and subtracting a CheY-P from the ring. A motor reversal takes place whenever n equals $N(\leq N_0)$, and N can take different values for $s = 1$ and $s = -1$. In general, k_+ and k_- depend on n, s and CheY-P concentration [YP](t). The dwell time is the first passage time of a Brownian particle moving under a position-dependent external force, which is rather complicated. Since $P(\Delta_f)$ and $P(\Delta_b)$ measured under various conditions can be well described by the inverse Gaussian distribution, below we seek a simple solution assuming that both k_+ and k_- are independent of n. This corresponds to the situation when the adsorbed CheY-P form a single domain on the ring and extends like a polymer. For large N, the above equation may be written in the continuum limit,

$$\frac{\partial p(x,t)}{\partial t} + V\frac{\partial p(x,t)}{\partial x} = D\frac{\partial^2 p(x,t)}{\partial x^2}, \tag{3.6}$$

where $\Delta x = N^{-1}$, $V = (k_+ - k_-)/N$, and $D = (k_+ + k_-)/2N^2$. For the given biophysical process, it is anticipated that $k_+ = k_{on}$[YP] and $k_- = k_{off}$, where k_{on} and k_{off} are the second and first order rate constants, yielding the equilibrium constant $K_D = k_{off}/k_{on}$. As can be seen, for $k_+ > k_-$ (or [YP]$/K_D > 1$), n increases ($V > 0$), and for $k_+ < k_-$ (or [YP]$/K_D < 1$), n decreases ($V < 0$). Since *V. alginolyticus* has a constant switching rate

$\simeq 2\,\mathrm{Hz}$ in the steady state, this model implies that [YP] is greater than K_D since otherwise the bacterium will be locked in one of the rotation states. The first-passage time PDF of Eq. 3.6 is given by the inverse Gaussian distribution [21, 56]

$$P(t) = \left(\frac{t_D}{2\pi t^3}\right)^{1/2} \exp\left[-\frac{(1-t/t_P)^2}{2(t/t_D)}\right], \tag{3.7}$$

where $t_P = 1/V$ and $t_D = 1/(2D)$ characterize domain growth and diffusion, respectively. The function $P(t)$ cuts off as $\exp(-1/t)$ for small t and $\exp(-t)$ for large t. The mean time of the distribution is $\langle t\rangle = t_P$. The parameters t_D and t_P also determine the peak position $t_{max} = (\gamma t_D/2)\left(\sqrt{(3\gamma)^2+4} - 3\gamma\right)$ and the width $\sigma_w = \gamma^{1/2} t_P$ of the PDF, where $\gamma \equiv t_P/t_D$. In particular for $\gamma \ll 1$, $t_{max} \simeq t_P$, and for $\gamma \gg 1$, $t_{max} \simeq t_D/3$. Differing from the equilibrium model [24], in our case there is a constant probability flux passing through each microscopic state and its magnitude is proportional to the difference $k_+ - k_-$. It is expected that as the flux gets larger, the switching decision becomes more deterministic and can be measured by the dimensionless width of the distribution $\sigma_w/\langle t\rangle = \gamma^{1/2} = 1/\sqrt{N(k_{on}[YP] - k_{off})/(k_{on}[YP] + k_{off})}$. We observed that when [YP]$\to\infty$, this sets the ultimate precision of the "device" to $\sigma_w/\langle t\rangle \to N^{-1/2}$. However, if little energy is used to maintain the flux, [YP]$\to K_D$, we found $\sigma_w/\langle t\rangle \to \infty$ since in this case the variance is no longer defined.

Despite its simplicity, as seen in Figure 24, this model allows us to fit our experimental data well with only two parameters, t_P and t_D. The fitting results for various PDFs are listed in Table 2.

As discussed above, non-monotonic dwell time PDFs indicate that the dynamics of transitions between CCW and CW states violates the detailed balance. Energy is thus required to maintain this non-equilibrium steady state. Unfortunately, the total energy expenditure is not directly measurable in our current experiment. However, the master equation (Eq. 3.6) itself implies elements of thermodynamic irreversibility and can be evaluated. For a non-equilibrium steady state, the probability flux is defined as

$$J(x) = Vp(x) - D\frac{\partial p(x)}{\partial x}. \tag{3.8}$$

Table 2: Fitting parameters for PDFs in Figure 24. $P(\Delta_f)$ and $P(\Delta_b)$ are measured from cells with low, medium and high cellular CheY concentration and fitted using inverse Gaussian with parameters t_D and t_P listed below. The uncertainties of t_P and t_D are calculated from the estimated covariance matrix.

CheY concentration	t_D (s)	t_P (s)	t_D (s)	t_P (s)
	Forward ($s = 1$)		Backward ($s = -1$)	
Low	1.34 ± 0.05	2.00 ± 0.09	3.9 ± 0.2	0.58 ± 0.08
Medium	1.45 ± 0.05	0.48 ± 0.06	3.2 ± 0.1	0.42 ± 0.04
High	1.65 ± 0.07	0.32 ± 0.04	2.7 ± 0.3	0.37 ± 0.09

Since V is constant, one can introduce a potential function $U(x) = -Fx$ and a fictitious viscosity coefficient η such that $V = -\frac{1}{\eta}\frac{\partial U}{\partial x} = F/\eta$, where F is constant. Based on the fluctuation-dissipation theorem, one expects $D = k_B T/\eta$. If one interprets $J(x)/p(x)$ as a fluctuating speed, the total energy dissipated toward making the transition is given by $W_{dis} = \eta \int_0^1 dx J(x)/p(x)$ [59]. Integrating by parts,

$$W_{dis} = k_B T \left(\frac{V}{D} - \ln p(x) \Big|_{x=0}^{x=1} \right). \tag{3.9}$$

We observed that energy dissipation consists of two parts. One part, $\ln p(x)$, is related to the boundary condition. For the ideal absorbing boundary at $x = 1$, which is assumed in our model, $-\ln p(1) \to \infty$. The other part accounts for energy dissipation for the domain growth and is well defined, $W_{dis} = k_B T(V/D) = (2t_D/t_P)k_B T$. This latter part may be considered as the minimum energy requirement for the transition. Since the average interval length is t_P, the dissipation rate $\dot{W}_{dis} = W_{dis}/t_P = (2t_D/t_P^2)k_B T$.

For *V. alginolyticus* with different cellular CheY concentrations, we calculated the energy dissipation rate for both the forward and backward intervals, and the results are shown in Table 3. We observed that for a given CheY concentration, W_{dis} and $\dot{W}_{dis}$ during the backward interval are considerably greater compared to those for the forward intervals. They also change little as CheY concentration increases, indicating that Δ_b is more strongly

enforced. The excess energy is essential in reducing spontaneous switches in short times. This may be significant for the 3-step swimmer since after switching from CW to CCW direction, *V. alginolyticus* veers in a new, random direction. The bacterium therefore may be more "cautious" in making a decision during this interval.

Table 3: Energy dissipation as a measure of motor irreversibility during forward and backward intervals at different CheY expression level. The uncertainties are calculated by error propagation.

CheY concentration	Dissipation rate$\dot{W}_{dis}$ (k_BT/s)		Dissipation W_{dis} (k_BT)	
	Forward	Backward	Forward	Backward
Low	0.67±0.09	23±7.6	1.34±0.1	13±2.5
Medium	13±3.6	36±8.0	6.0±1.0	15±1.9
High	32 ± 9.4	39 ± 23	10±1.7	15 ± 5

Based on our investigation, the unique feature of *V. alginolyticus* flagellar motor is its switching logic, behaving like a molecular toggle switch, and the existence of a refractory period immediately after a switch. The bacterium uses considerable amounts of energy (see Table 3) to suppress spontaneous motor reversal. This is different from *E. coli*, which upon switching to a new state can immediately switch back with a high probability. Protection of a nascent state is commonly seen in digital electronics. Since high fidelity in execution of a program is so important, the "dead" time after a switch is built into logical gates of a circuit. For marine bacteria that execute the 3-step motility pattern, the "dead" time can be biologically significant. We believe that this is microorganism's means of combating noise, ensuring that its switching decision is not overwritten by stochastic noise in a short time. All indication suggests that *V. alginolyticus* regulates its backward swimming interval more stringently than its forward counterpart. Consequently, $P(\Delta_b)$ is more narrowly distributed than $P(\Delta_f)$. This phenotype may be understood by the fact that for the 3-step swimmer, the forward intervals is followed by backtracking, allowing the same space to be revisited. However, such bootstrapping is absent for the backward interval, and the bacterium enforces its swimming decision more judiciously for the last step of its swimming cycle.

For the marine bacterium, it may be asked why the protection of the nascent state is important, particularly for the backward intervals? The answer may very well be in the fine structures of nutrient patches in the ocean environment. Despite stochasticity of turbulence, dispersion of a scalar quantity in small scales has time scales that are more-or-less deterministic, obeying the physics law of mixing. The existence of a mixing time allows the bacteria to develop an anticipatory response, which can explain what we observed.

To illustrate the idea, we take the typical energy dissipation rate of turbulence near the surface layer of ocean to be $\epsilon \simeq 0.1\,\mathrm{cm}^2/\mathrm{s}^3$ and the viscosity $\nu \simeq 0.01\,\mathrm{cm}^2/\mathrm{s}$ [46]. An important spatial scale of turbulence is the Kolmogorov scale, $\ell_\eta = (\nu^3/\epsilon)^{1/4}$, which marks the termination of the inertia dominated flow and the beginning of a viscous subrange. For the given ϵ and ν, we find $\ell_\eta \simeq 0.06\,\mathrm{cm}$. Marine bacteria live in a world in which the typical length scale, determined by the product of rotation diffusion time and the swimming speed, they sense is less than ℓ_η.

Consider now a nutrient patch that is dispersed by turbulence. If for the scales $\ell < \ell_\eta$ the nutrient is uniformly distributed, the bacteria may just give up chemotaxis because searching has no benefit. However, owing to the molecular diffusivity D_0 of small nutrient molecules being typically several thousand times smaller than the kinematic viscosity ν of sea water, the nutrients are not distributed uniformly, but rather in patches and striations similar to stirred milk in a coffee cup. Turbulence causes these spatial inhomogeneities to thin and eventually dissolve at a scale $\ell_C = (\nu D_0^2/\epsilon)^{1/4}$, which is known as the Batchelor scale [10]. A back-of-the-envelope calculation for small amino acids, such as serine ($D_0 \simeq 900\,\mu\mathrm{m}^2/\mathrm{s}$), shows $\ell_C \simeq 17\,\mu\mathrm{m}$. Thus over a range of spatial scales $\ell_C < \ell \leq \ell_\eta$ (or $20 < \ell < 600\,\mu\mathrm{m}$ for the present case), known as the viscous-diffusion subrange, the marine bacteria can benefit from non-uniform distribution of nutrients if an appropriate chemotactic strategy is used. We note that since $\ell_C \propto \epsilon^{-1/4}$, the higher the turbulence intensity the smaller the dissolving scale ℓ_C. Moreover, because of the small (1/4) exponent, the ϵ dependence is weak, and we expect that $\ell_C \simeq 20\,\mu\mathrm{m}$ should not change much under different conditions. Thus, it is reasonable that for a bacterium to follow changes in a nutrient field, it has to swim the minimal distance ℓ_C because otherwise the chemical landscape is featureless. Because the typical swimming speed of a marine bacterium is $v_{sm} \simeq 100\,\mu\mathrm{m/s}$ [55], it follows that the

persistent swimming time should be ~ 0.2 s. This agrees rather well with the peak positions of the dwell time PDFs, $P(\Delta_f)$ and $P(\Delta_b)$, seen in our experiment. The biological and ecological implication of the above observation is significant and should be studied in future experiments.

4.0 THE CHEMOTACTIC RESPONSE OF *V. ALGINOLYTICUS*

In this chapter, we evaluate the chemotactic response of *V. alginolyticus* quantitatively. Since the chemotaxis network of *V. alginolyticus* will be modeled based on what we know about *E. coli*, we start by discussing the chemotaxis network in *E. coli* with more details together with a concise mathematical model developed by Y. Tu [77]. To determine if this model can be applied to *V. alginolyticus*, we compared the chemotaxis network of *V. alginolyticus* to that of *E. coli* by studying the behavior of different mutants lacking different chemotaxis genes. Since it appears that the chemotaxis networks in these two bacteria are very similar, the equations describing the change of [YP] due to chemical stimuli in *E. coli* are applied to the case of *V. alginolyticus*. Using the result obtained in Chapter 3, i.e. the dependence of $k_f(t)$ and $k_b(t)$ on [YP], $k_f(t)$ and $k_b(t)$ after a chemical stimulation in *V. alginolyticus* can be quantitatively described. This model for *V. alginolyticus*, adapted from *E. coli*, is then applied to an experiment where $k_f(t)$ and $k_b(t)$ of *V. alginolyticus* cells are measured after a certain amount of attractant is suddenly released to the motility medium.

4.1 CHEMOTAXIS SYSTEM OF *E. COLI*

E. coli's chemotaxis system comprises three modules as shown in Figure 26. In this system, activity of the chemoreceptor is modified when it is bound by chemoeffectors. This change propagates through the chemotaxis network via protein-protein interactions and is converted into an output signal that regulates the flagellar motor. Chemotaxis network of *E. coli* consists of six proteins: CheA, CheW, CheB, CheR, CheY and CheZ.

Two types of protein-protein interactions are involved in the signal transduction process.

The first is the phosphorylation reaction involving a kinase protein, which is an enzyme that modifies other proteins by chemically adding phosphate groups to them. Phosphorylation usually results in a functional change of the target protein by altering its enzyme activity or affinity with other proteins. CheA is such a kinase protein in the chemotaxis network. Its activity is modulated by chemoreceptors, when it is active due to unbinding of chemoattractants or binding of chemorepellents, it auto-phosphorylates itself and transfers the phosphate group to two other chemotaxis proteins, CheY and CheB so they become CheY-P and CheB-P respectively. Phosphorylation can be reversed by dephosphorylation, where the phosphate group is either removed spontaneously, which is the case for CheB-P, or by another protein, which is the case for CheY-P. In the case of *E. coli*, the phosphate group on CheY-P is removed by the chemotaxis protein CheZ. The second type of protein-protein interaction is the methylation reaction involving methyltransferase and methylesterase. The former adds and the latter removes a methyl group to a target protein. In the chemotaxis network of *E. coli*, the methyltransferase CheR methylates the receptors at a constant rate, increasing the activity of CheA. On the other hand, the methylesterase CheB-P demethylates the receptors by removing the methyl group, thus decreasing the activity of CheA

In *E. coli*, the input of the signal transduction network is the activity of CheA, which is suppressed when attractant molecules bind to receptors but raised when repellent molecules bind. At equilibrium, phosphorylation of CheY is balanced by dephosphorylation of CheZ, maintaining a constant CheY-P concentration $[YP]_0$; methylation of the receptor by CheR is balanced by demethylation through CheB-P, so that receptors have a constant methylation level and CheA has constant activity. When the concentration of chemoattractant outside the cell suddenly increases, the equilibrium of chemotaxis network is broken due to the sudden decrease in CheA activity. As a result, [YP] decreases and the cell swims smoothly. At the same time, inactive CheA results in CheB-P level dropping, while CheR keeps methylating the receptors bringing up the activity of CheA. Finally, the network reaches a new equilibrium state, where activity of CheA and [YP] restores to the pre-stimulation level, but the methylation level reaches a new steady value higher than that before the stimulation.

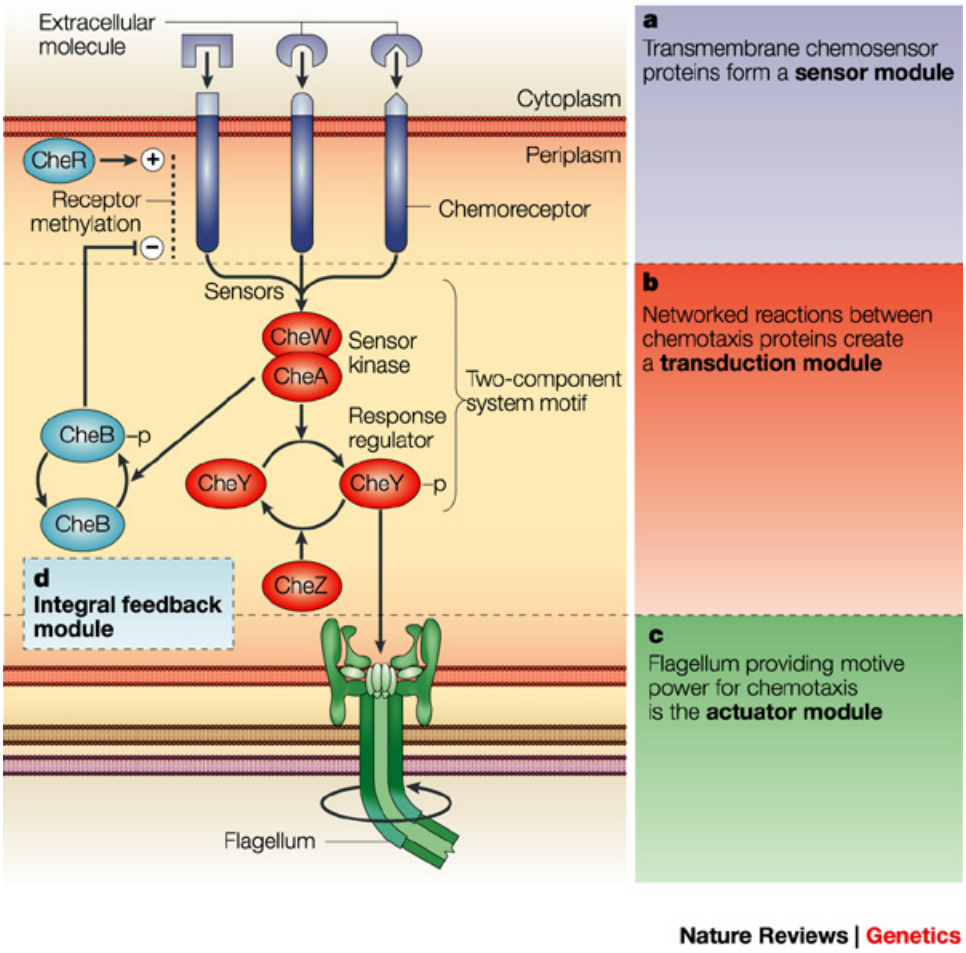

Figure 26: The figure illustrates the modular nature of the *E. coli* chemotaxis network. a. The sensor module includes several different chemoreceptors that are sensitive to different extracellular molecules. External molecules bind to receptors on the cell surface and activate the CheW/CheA sensor kinase. b. The transduction module comprises biochemical reactions between different chemotaxis molecules that create a pathway that communicates a signal to the distant flagella. This signal changes the frequency of reversal of the flagella motor (the actuator module, c) in a manner that causes the bacteria to swim generally towards attractive chemical sources and away from hazardous sources. d. The feedback loop within the sensor module, which involves methylation of the receptor, allows the network to operate over wide concentration ranges of the external molecule that is being sensed. The sensor kinase response regulator reaction, labeled as a TWO-COMPONENT SYSTEM motif, is part of the communication link that signals the status of the chemoreceptors to the motor. This figure is taken from Figure 1 in Ref. [53].

4.1.1 Measurements of *E. coli*'s chemotactic response

Since the flagellum rotation direction is regulated by the messenger protein CheY-P, the swimming behavior of the bacterium exhibits a similar transient response as [YP] does when subject to a sudden change in chemoeffector concentrations. This permits the study of bacterial responses to different chemicals by following the motor rotation states when subject to the chemical stimuli.

For *E.coli*, a well-developed method to monitor the rotation state of the flagellar motor is the tethering assay. In this assay the flagellum of the bacterium is tethered to a surface so that the rotation direction of the motor can be inferred from the rotation direction of the cell body. J. Segall et al. took advantage of this technique and are the first to investigate the transient response of *E. coli* to various chemical stimuli by measuring $\phi_{CCW}(t)$, the probability that a motor is rotating in the CCW direction at time t after the stimulation. When ϕ_{CCW} is close to 1, most flagella rotate CCW and *E. coli* would swim smoothly. When ϕ_{CCW} is close to 0, CW rotating flagella makes the cell tumble incessantly.

Given a physical system, its Green's function describes the system's response to an impulse stimulation and can be used to predict the system's output to any time-varying stimuli if the superposition principle can be applied. For the chemotaxis network, Green's function, or the response function $R(t)$, is proportional to the change in CCW bias as a function of time, $\Delta\phi_{CCW}(t)$, when the bacterium is subject to a pulse of chemoattractant at $t = 0$. Figure 27(A) (from Ref. [65]) showed $R(t)$ of wild type *E. coli*. A significant feature of this response is that $R(t)$ is biphasic: after a rapid rise, instead of returning to the baseline monotonically, $R(t)$ overshoots before recovers to the pre-stimulation level at a slower rate. Furthermore, the total area under the $R(t)$ curve is zero, i.e., $\int_0^\infty R(t)dt = 0$. This guarantees that the cell can always recover the pre-stimulation behavior after experiencing a step rise in attractant concentration, which is indeed observed as shown in Figure 27(B), where the ambient chemoattractant concentration stepped up at $t = 1$ s. The solid line is a prediction based on $R(t)$ measured in Figure 27(A) and the agreement is very satisfactory.

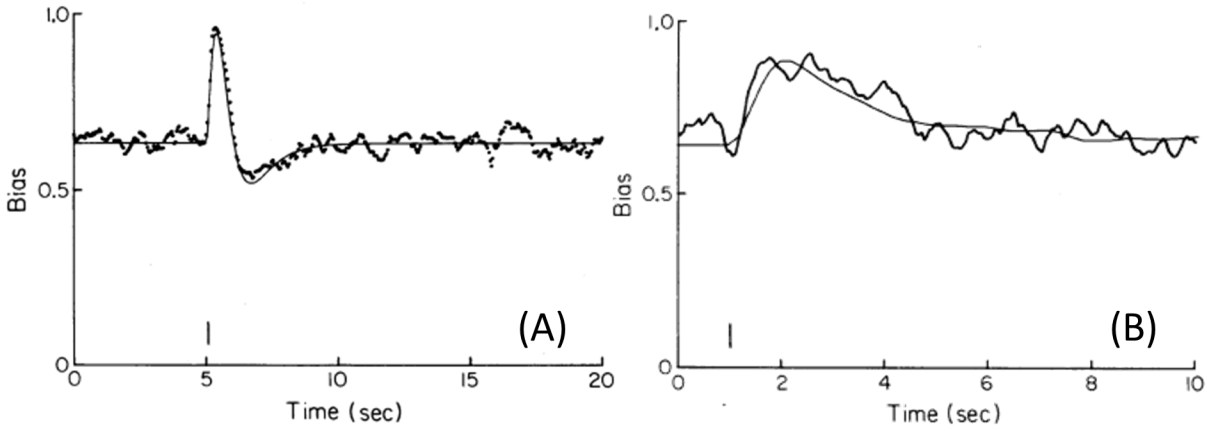

Figure 27: (A) Impulse response to attractant in wild-type *E. coli* cells. The dotted curve is the probability, determined from repetitive stimulation, that tethered cells of strain AW405 spin CCW when exposed to pulses of L-aspartate or α-methyl-DL-aspartate beginning at 5.06 sec (vertical bar). The smooth curve is a fit to a sum of exponentials. (B) Step response to attractant in wild-type *E. coli* cells. The thick curve is the probability that cells of strain AW405 spin CCW when exposed to steps of L-aspartate or α-methyl-DL-aspartate beginning at 1.00 sec (vertical bar). The thin line is the response predicted from the impulse response (the dotted curve in (A)). These two figures are taken from Figure 1 and 2 from Ref. [65] and only part of the captions are kept here to leave out irrelevant information. The Bias label on the y axis corresponds to ϕ_{CCW} in the main text.

4.1.2 Theoretical modeling on *E. coli*'s chemotactic response

As the knowledge of the interactions among different chemotaxis proteins accumulates, a coherent model has emerges to explain the experimental observations [77]. This model is described below and will be examined and modified to be applied to the chemotaxis network of *V. alginolyticus* in the next section. Taking into consideration the dependence of CheA's activity a on chemoeffector concentration c as well as the interdependence between a and the methylation level m, the model consists of two equations,

$$\frac{dm(t)}{dt} = F(a) \tag{4.1}$$

$$a = G(m, c) \tag{4.2}$$

Eq. 4.1 describes the kinetics of the feedback loop CheR-CheB. While CheR methylates the receptor at a constant rate, CheB needs to be phosphorylated by active CheA into CheB-P before it can remove methyl groups. Thus $F(a)$ should be a monotonically decaying function of a, since large a increases the concentration of CheB-P which counteract CheR, resulting in a reduced methylation rate. Eq. 4.2 basically describes that the activity of CheA is determined by the chemoeffector concentration as well as the methylation level of the chemoreceptor. When the chemotaxis network is at equilibrium at a given attractant concentration c_1, there exists an a_0 so that $dm/dt = F(a_0)$=0, $a_0 = G(m_1, c_1)$, where m_1 is the current methylation level. When the attractant suddenly increases by Δc, a, the activity of CheA would drop below a_0, so that $dm/dt > 0$, since methylation by CheR exceeds demethylation by CheB-P due to the sudden decrease in a. As m increases, a also increase until it reaches a_0 again, the system relaxes into a new equilibrium state, where again $dm/dt = F(a_0)$=0 but $a_0 = G(m_1 + \Delta m, c_1 + \Delta c)$ where the methylation level increased by Δm to balance Δc. Thus this model, although simple, can indeed describes the transient response observed in *E. coli*. In order to make quantitative comparison with experimental results, a two-state model is used to formulate Eq. 4.2:

$$a = \frac{\exp(-f(m, c))}{1 + \exp(-f(m, c))} \tag{4.3}$$

where $f(m,c)$ is the free energy between active CheA and inactive CheA. $f(m,c)$ is then decomposed into two terms $f(m,c) = N(f_m(m)+f_c(c))$, where f_m is the methylation-dependent free energy, f_c is the attractant-binding-dependent free energy and N is an amplification constant accounting for the cooperativity among chemoreceptors.

For f_m, since the activity of CheA increases as m increases, f_m is chosen to be a simple monotonically decaying linear function of m, $f_m = \alpha(m_0 - m)$, where α and m_0 are constants that can be inferred from experimental data. f_c is formulated by the MWC model, which is commonly applied to protein complex consisted of multiple identical subunits. The high sensitivity of receptor clusters to change in chemoeffector concentration is well captured by this model [67]. The MWC model has the following main gradients: (i) all receptors assume the same conformation, active or inactive. (ii) Chemoeffector molecules bind to active or inactive receptors with different affinities, characterized by different dissociation constants K_A and K_I, respectively. For binding of attractant molecules, $K_A \gg K_I$ so that an attractant molecule has a higher affinity to an inactive receptor than an active receptor, a mechanism underlying a lot of biochemical processes that exhibit high sensitivity. (iii) The probabilities of receptors being active or inactive are determined by the Boltzmann's factor. Take E to be the energy difference between active and inactive states in absence of chemoeffectors, the free energies under four different scenarios can be specified as below (k_BT is taken to be 1): the free energy is $E - \ln(c/K_A)$ for an active receptor that is bound by an attractant molecule, E for an active receptor that is unbound, $-\ln(c/K_I)$ for an inactive receptor that is bound and 0 for an inactive receptor that is unbound. Here $\ln(c/K_A)$ and $\ln(c/K_I)$ can be identified as chemical potentials. The free energy $f_c(c)$ between active and inactive receptors can then be written as $\exp(-f_c(c)) = \exp(-E)(1 + c/K_A)/(1 + c/K_I)$ or

$$f_c(c) = E + \ln(1 + c/K_I) - \ln(1 + c/K_A) \tag{4.4}$$

With this model, chemotaxis response to different time-varying stimuli can be obtained by solving the linearized Eq. 4.1-4.2 about the equilibrium state. Specifically, let a_0, m_1, and c_1 be the equilibrium activity of CheA, methylation level and external chemical concentration,

respectively. Write $a(t) = a_0 + \Delta a(t)$, $m(t) = m_1 + \Delta m(t)$ and $f_c(c(t)) = f_c(c_1) + \Delta f_c(t)$,

$$\frac{d\Delta m}{dt} = F'(a_0)\Delta a \tag{4.5}$$

$$\begin{aligned} \Delta a &= \left.\frac{\partial G(m,c)}{\partial f(m,c)}\right|_{m_1,c_1} (-\alpha\Delta m + \Delta f_c) \\ &= -Na_0(1-a_0)(-\alpha\Delta m + \Delta f_c) \end{aligned} \tag{4.6}$$

Solving Eq. 4.5-4.6 in the frequency space,

$$\widetilde{\Delta a} = \frac{i\omega c_a}{i\omega + 1/\tau_m}\widetilde{\Delta f_c} \tag{4.7}$$

where $\widetilde{\cdots} = \int \cdots \exp(-i\omega t)dt$, $c_a = -Na_0(1-a_0) < 0$, $1/\tau_m = \alpha F'(a_0)c_a > 0$ is a typical frequency determined by the the methylation rate thus τ_m is the typical methylation time.

The output of the chemotaxis network is the CheY-P concentration [YP], and its fluctuation around the equilibrium concentration $\Delta[YP] = [YP] - [YP]_0$ can be described as

$$\frac{d\Delta[YP]}{dt} = k_a\Delta a - \frac{\Delta[YP]}{\tau_Z} \tag{4.8}$$

where k_a is the rate of phosphorylation by CheA and $1/\tau_Z$ is the rate of dephosphorylation by CheZ. In the frequency space, $\widetilde{\Delta[YP]}$ can be solved as

$$\widetilde{\Delta[YP]} = \frac{i\omega c_a k_a}{(i\omega + 1/\tau_Z)(i\omega + 1/\tau_m)}\widetilde{\Delta f_c} \tag{4.9}$$

so that

$$\Delta[YP](t) \equiv [YP](t) - [YP]_0 = \int^t R_Y(t-t')\Delta f_c(t')dt' \tag{4.10}$$

where $R_Y(t)$ is the response function of [YP] and

$$R_Y(t>0) = R_0[\tau_z \exp(-t/\tau_m) - \tau_m \exp(-t/\tau_z)]/(\tau_m - \tau_z) \tag{4.11}$$

where τ_m and τ_z are the typical times of methylation and dephosphorylation respectively and $R_0 = -c_a k_a > 0$ is the gain of the response depending on the equilibrium activity of CheA before stimulation a_0. To relate the change in [YP] to the change in ϕ_{CCW}, recall Eq.

3.1 in Chapter 3 that describes the dependence of ϕ_{CW} on [YP]. In a small range around K_m Eq. 3.1 is approximately linear and

$$\phi_{CW}([YP]) = \frac{1}{2} + \frac{H}{4K_m}([YP] - K_m). \tag{4.12}$$

The response of *E. coli* to a time-varying attractant fluctuation is then

$$\begin{aligned} \Delta\phi_{CCW}(t) &= -\frac{H}{4K_m}\Delta[YP](t) = -\frac{H}{4K_m}\int^t R_Y(t-t')\Delta f_c(t')dt' \\ &= \int^t R(t-t')\Delta f_c(t')dt' \end{aligned} \tag{4.13}$$

where $R(t) = -\frac{H}{4K_m}R_Y(t)$. This compares well with the measured $R(t)$ in Ref. [65], from which the two time constants can be determined as $\tau_m \approx 3$ s and $\tau_z \approx 0.5$ s.

There are several remarks that worth making. First, For *E. coli*, it was measured that $K_I = 18$ μM and $K_A/K_I \approx 160 \gg 1$. Thus if the attractant concentration $c(t)$ is $K_I \ll c(t) \ll K_A$, $f_c(t) \approx E + \ln(c(t)/K_I)$. In other words, the response is proportional to $\ln c(t)$ instead of $c(t)$, which is known as Weber law and observed in sensory systems in higher organisms, such as the human vision [73]. Logarithm sensing enables the system to have a large dynamic range and respond even when $c(t)$ varies by orders of magnitude.

Second, consistent with the observation, $R_Y(t)$ or $R(t)$ is biphasic and the positive lobe and negative lobe have the same area so that $\int_0^\infty R(t)dt = 0$. This indicates that when the ambient chemical concentration steps up at $t = 0$ so that $\Delta f_c(t)$ is proportional to a Heaviside step function,

$$\Delta\phi_{CCW}(t \to \infty) = \Delta f_c \int_0^{t\to\infty} R(t-t')dt' = \Delta f_c \int_0^\infty R(t')dt' = 0, \tag{4.14}$$

or in other words, [YP] as well as the cell behavior recovers exactly to the pre-stimulation level, which is called perfect adaption. Perfect adaptation allows the cell to migrate in the favorable direction under a wide range of background chemical concentrations and eventually reach the peak of the nutrient concentration.

Third, as seen in Eq. 4.9, two typical time scales are involved, τ_Z and τ_m and $\tau_Z < \tau_m$. The initial rapid rise and decay in the measured $R(t)$ is due to the fast phosphorylation of CheY by CheA and fast dephosphorylation of CheY-P by CheZ, characterized by the

small τ_Z. After the overshoot, $R(t)$ recovers to 0, as a result of methylation by CheR and demethylation by CheB-P. This process happens more slowly with the time scale τ_m. CheR and CheB thus functions as a feedback loop in the chemotaxis, which resets the equilibrium so the network can adapt perfectly.

4.2 CHEMOTAXIS SYSTEM OF *V. ALGINOLYTICUS*

Compared to chemotaxis system of *E. coli*, much less physiological and biochemical data exist for *V. alginolyticus*. Fortunately, a lot of what is known about *E. coli* can still be applied to *V. alginolyticus*. Recently, the genome sequence of *V. alginolyticus* became available so that the function of a protein in *V. alginolyticus* can be hypothesized via sequence comparison. If the sequence of a protein in *V. alginolyticus* is very similar to the sequence of a certain protein in *E. coli*, these two proteins might function similarly.

Such sequence comparison reveals that while *E. coli* has only five chemoreceptors, *V. alginolyticus* has more than 20 putative receptors and their functions have not been systematically studied. However, locations of receptors in different species, bacteria and archaea, are conserved and clustered around the poles [29]. This indicates that in different species, receptors are likely to function similarly, forming arrays to interact each other to increase high sensitivity. In other words, the formulation of $f_c(c)$, or Eq. 4.4 for *E. coli* should also be reasonable for *V. alginolyticus*.

V. alginolyticus has all six chemotaxis proteins that *E. coli* has plus CheV, a chemotaxis protein that was also identified in other bacterial species [4]. The sequences of the six Che(ABRWYZ) proteins in these two bacteria are similar. For example, 64% amino acids of *V. alginolyticus*' CheY protein are identical to those of *E. coli*. Furthermore, these two CheY proteins have almost the same functional sites, suggesting that *V. alginolyticus*' CheY can be phosphorylated at the same position as well as interact with the motor switch complex to control the motor's rotation direction. We thus hypothesize that the chemotaxis network of *V. alginolyticus* should operate in the same way as *E. coli*. To confirm this hypothesis, behaviors of *E. coli* and *V. alginolyticus* mutants lacking a certain *che* gene were observed

to compare the role of this gene in these two bacteria.

In *E. coli*, [YP] is controlled by the activity of CheA. Thus deletion of a gene whose protein product increases CheA activity, such as *cheR*, results in lower [YP] than that of the wild type, and the cell swim smoothly most of the time. When genes whose product suppresses CheA activity are deleted, the cell tumbles most of the time. The swimming behaviors of *E. coli* mutants are listed in Table 4 [57].

	E. coli		*V.alginolyticus*	
Genotype	[YP]	swimming behavior	[YP]	swimming behavior
$\Delta cheA$	0	$\Delta_{CCW} = \infty$, $\Delta_{CW} = 0$	0	$\Delta_f = \infty$, $\Delta_b = 0$
$\Delta cheY$	0	$\Delta_{CCW} = \infty$, $\Delta_{CW} = 0$	0	$\Delta_f = \infty$, $\Delta_b = 0$
$\Delta cheZ$	high	short Δ_{CCW} and long Δ_{CW}	same	similar to wild type
$\Delta cheR$	low	long Δ_{CCW} and short Δ_{CW}	low	long Δ_f and short Δ_b
$\Delta cheB$	high	short Δ_{CCW} and long Δ_{CW}	high	short Δ_f and short Δ_b
$\Delta cheV$	NA		low	long Δ_f and short Δ_b

Table 4: Phenotype of different *E. coli* and *V. alginolyticus* mutants. $\Delta cheW$ is not investigated since CheW is a coupling protein between CheA and the chemoreceptors and is not involved in Eq. 4.1 and 4.2 directly.

In *V. alginolyticus*, CheY-P regulates the flagellar motor differently than in *E. coli*. As discussed previously in Chapter 3 (Figure 17), CheY-P regulates the switching rates of the motor. At low [YP], the flagellar motor of *V. alginolyticus* rotates CCW and the cell swim forward most of the time. On the other hand, at high [YP], the flagellar motor switches between CCW and CW states at a high rate, resulting in shorter intervals in both forward and backward swimming directions. The swimming behavior of mutant *V. alginolyticus* are also listed in Table. 4, from which [YP] is inferred. As can be seen, except *cheZ* , deletions of *che* genes have the same effect on [YP], indicating that CheA, CheR, CheB play the same role in both chemotaxis networks. *cheV* gene is not present in *E. coli*, but it was well characterized in other bacteria, such as *Bacillus subtilis*, and is involved in adaption. As shown in Table 4, deleting *cheV* results in the same phenotype as deleting *cheR*, indicating

that CheV might serve a similar function as CheR. Therefore, it appears that the chemotaxis network in *V. alginolyticus* operates similarly as that in *E. coli* and Eqs. 4.1-4.2 can describe the chemotaxis networks in both bacteria.

CheZ in *V. alginolyticus* seems to function differently than in *E. coli* since deletion of *cheZ* results in a phenotype similar to the wild type, as highlighted in Table 4. If *V. alginolyticus'* CheY-P does not get dephosphorylated by CheZ or through other means, Eq. 4.8 for *V. alginolyticus* should be modified as

$$\frac{d\Delta[YP]}{dt} = k_a \Delta a.$$

The resulting response function then should be $R_Y(t) = k_a c_a \exp(-t/\tau_m)$, indicating that the chemotaxis network of *V. alginolyticus* cannot adapt. This would be a great flaw and is unlikely considering the remarkable chemotaxis capacity displayed by *V. alginolyticus* as shown in Figure 2. We thus hypothesize that there must be a mechanism for dephosphorylation of CheY-P, either by an unknown protein or CheY-P dephosphorylates automatically, so that it has a typical life time of τ_Z and Eq. 4.8 is still valid.

4.2.1 Measuring response function of *V. alginolyticus*

To measure the chemotactic response of *V. alginolyticus* to chemical stimulations, we carried out the following stimulation experiment. In the setup, cells were suspended in the motility buffer and a certain concentration of attractant serine c_0 was applied during a period of time (100 ms) which is much less than the typical chemotaxis time scales (more details in Materials and Methods). The responses were quantified using the time-dependent switching rates $k_f(t)$ and $k_b(t)$, i.e., the probability per time that a bacterial flagellar motor makes the transition from CCW to CW rotation and from CW to CCW, respectively. Fig. 28 displays these time-dependent rates when the bacteria are stimulated with different c_0. For $t < 0$, both k_f and k_b fluctuate around the steady-state switching rates $k_{f0} \simeq 2.3 \pm 0.1$ s^{-1} and $k_{b0} \simeq 1.9 \pm 0.1$ s^{-1}, which are delineated by the blue dashed lines in the plots. Several features were observed: First, both k_f (Fig. 28(A-E)) and k_b (Fig. 28(F-J)) recover the pre-stimulation levels for a sufficiently long time. This shows that for the given range

of c_0, the chemotaxis network of *V. alginolyticus* adapts nearly perfectly to serine. Such a behavior is similar to *E. coli*'s response to aspartate but not to serine, the latter was found to be imprecisely adaptive at concentrations higher than 1 μM [14]. Second, shortly after stimulation, both k_f and k_b decrease as a result of exposure to serine, and the amplitude of the responses correlates strongly with c_0. For a relatively high-level serine stimulus, such as $c_0 = 20$ μM (see Figs. 28(E, J)), the decrease in the switching rates can be greater than their steady-state values. As a result k_f and k_b remain zero for some time ($\sim$ 1 s) before rising toward the pre-stimulation value. Finally, for a low-level stimulus, the responses in the forward and backward directions are not symmetrical. For example, in the case of $c_0 = 1$ μM, while $k_f(t)$ drops significantly by ˜1.5 Hz, little change is seen in $k_b(t)$. This suggests that the flagellar motor in the CW state is less sensitive to the change in the regulator protein (CheY-P) concentration than its CCW counterpart (see more discussion below). However, this asymmetry appears to disappear when the stimulation level is increased.

The above rate measurements reveal an important difference between *V. alginolyticus'* and *E coli*'s response to a chemoattractant stimulus: While both microorganisms reduce the motor switching rate when it is in the CCW state, the response of a CW-rotating motor is exactly opposite in the two organisms, i.e., while k_b is reduced in *V. alginolyticus*, the corresponding rate in *E. coli* is increased [15]. From the stand point of a microorganism, both responses make good sense. Since *V. alginolyticus* is a bi-directional swimmer and able to pursue chemoattractant in both forward and backward swimming directions, by extending the backward swimming interval when positively stimulated, the cell can migrate closer to the source of attractant. On the other hand, since CW state cannot produce displacement for *E. coli*, quickly switching out of that state upon positively stimulated so that the cell can pursue new "opportunities" also makes good biological sense. However, how the microorganisms use the essentially identical set of regulatory proteins to achieve this remarkable feat is fascinating and remains to be investigated.

To quantify chemotaxis response of *V. alginolyticus* to different stimuli, it is useful to measure $R(t)$ or $R_Y(t)$ in this bacterium. However, since CheY-P regulates the switching rates of the motor, $R(t)$ should be related to the change of rates, instead of change in bias. Recall the measured $k_f(t)$ and $k_b(t)$ as a function of I or [YP] in Chapater 3, linearize Eq.

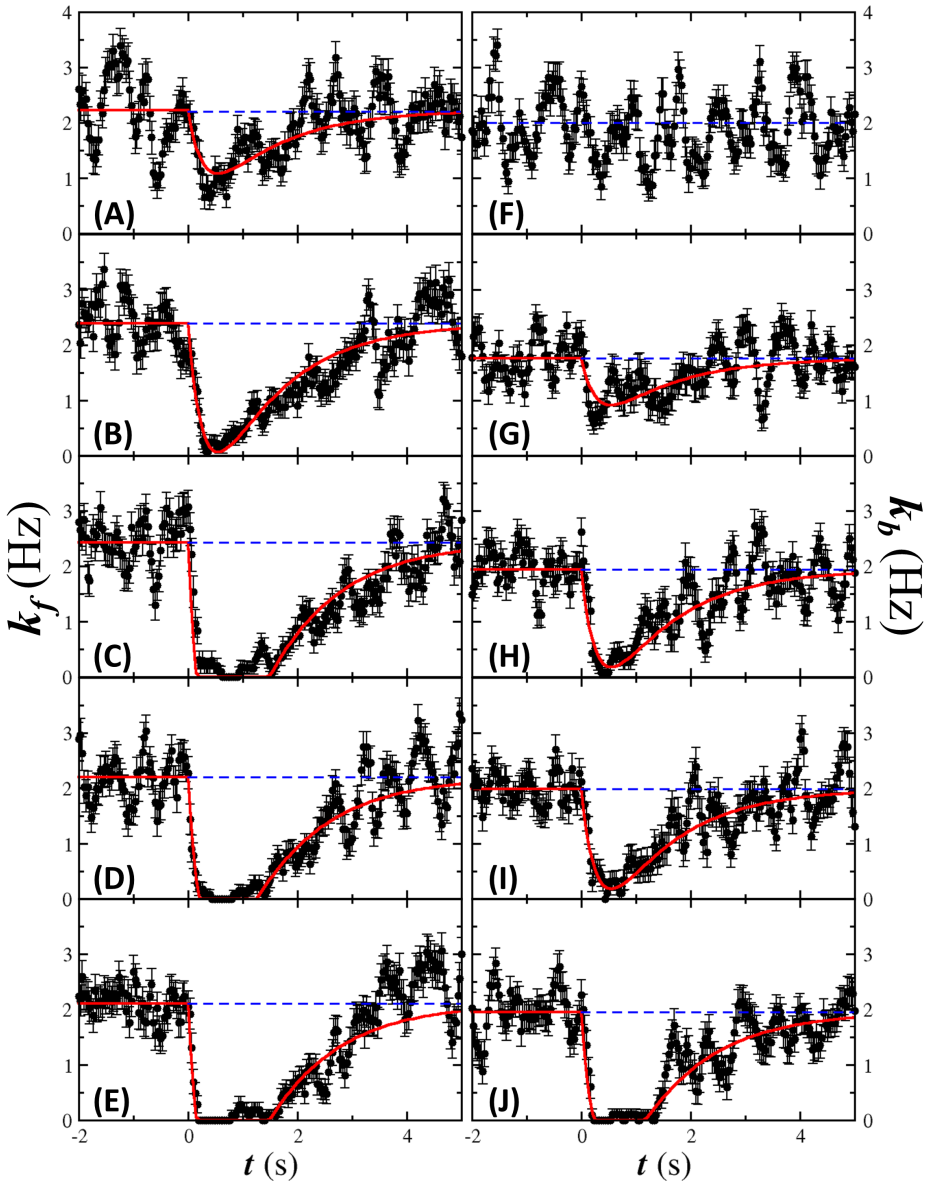

Figure 28: Flagellar motor switching rates $k_f(t)$ and $k_b(t)$ resulting from a stepwise stimulus. (A-E) show $k_f(t)$ before and after the ambient serine concentration jumps from 0 to c_0 =1, 2.5, 5, 10 and 20 μM, respectively. (F-J) show $k_b(t)$ before and after the ambient serine concentration jumps from 0 to c_0 =1, 2.5, 5, 10 and 20 μM, respectively. The blue dashed line marks the average pre-stimulation rates k_{f0} and k_{b0}, respectively. The red curves are fitting results using Eq. 4.17.

3.2 around physiological concentration $[YP]_0$, $k_f([YP])$ and $k_b([YP])$ can be described as

$$k_x([YP]) = k_{x0}\left(1 + \frac{H_x}{[YP]_0}([YP] - [YP]_0)\right), \tag{4.15}$$

where $x \in \{f, b\}$, and H_x is a gain factor of the motor. Combining Eq. 4.8 and 4.15, the response of k_f and k_b to a chemical stimulation can be written as

$$k_x(t) = k_{x0}\left(1 + \frac{H_x}{[YP]_0}\int^t R_Y(t-t')\Delta f_c(t')dt'\right). \tag{4.16}$$

In our experiment, because free serine was created over a sufficiently large area during a short interval of 0.1 s, we expect,

$$c(t) = \begin{cases} 0 & t \leq 0 \\ c_0 & t > 0, \end{cases}$$

which gives $\Delta f_c = \ln\left[(1 + c_0/K_I)/(1 + c_0/K_A)\right]$ for $t > 0$. Replacing this result in Eq. 4.16 yields,

$$k_x(t) = k_{x0}\left[1 - R_{x0}\frac{\tau_Z\tau_m}{\tau_m - \tau_Z}(\exp(-\frac{t}{\tau_m}) - \exp(-\frac{t}{\tau_Z}))\right], \tag{4.17}$$

where $R_{x0} = H_x R_{Y0}\Delta f_c/[YP]_0$ is the overall chemotaxis response amplitude.

To extract quantitative information of chemotactic network of *V. alginolyticus* using the above theoretical model, curves in Fig. 28 were fitted using Eq. 4.17. To minimize the number of free parameters, the steady-state switching rates k_{f0} and k_{b0} are assumed to be known, determined by averaging $k_f(t)$ and $k_b(t)$ from $t = -2$ s to $t = 0$ s. The remaining constants in Eq. 4.17, such as R_{x0}, τ_m and τ_Z, are treated as adjustable parameters. To account for the saturation in responses at $c_0 = 10$ μM and 20 μM where $k_f(t)$ or $k_b(t)$ remains zero for more than a second, parameters that cause $k_x(t)$ to be negative are allowed, but negative $k_x(t)$ is replaced by zero. Within the linear-response approximation, τ_m and τ_Z are expected to be independent of c_0 and should be treated as global fitting parameters. As shown by the red lines in Fig. 28, the quality of the fits is satisfying considering that effectively R_{x0} is the only local fitting parameter for each curve. The non-linear regression

procedure yields $\tau_m = 1.29 \pm 0.04$ s and $\tau_Z = 0.28 \pm 0.01$ s. These chemotactic time scales in the marine bacterium are considerably shorter compared to those observed in *E. coli* [65, 77].

As for the response amplitudes, it was found $R_{f0} = 2.8 \pm 0.6$, 5.2 ± 0.6, 8.8 ± 1.2, 7.5 ± 0.9 and 8.9 ± 1.2 Hz for the forward intervals (see Fig. 28(A-E)) corresponding to c_0 =1, 2.5, 5 10 and 20 μM, respectively and $R_{b0} = 2.6 \pm 0.6$, 4.9 ± 0.6, 4.9 ± 0.6, and 7.1 ± 0.9 Hz for the backward intervals (see Fig. 28(G-J)) corresponding to c_0 =2.5, 5 10 and 20 μM, respectively. In Fig. 29, the amplitudes of the responses, R_{f0} (green squares) and R_{b0} (red dots), are plotted for different serine concentrations c_0. Here both curves appear linear when c_0 is plotted on a semi-logarithmic scale, indicating that chemical sensing of the marine bacterium obeys Weber's law as many other biological systems [54]. Moreover, from these measured response amplitudes, the binding affinity (or the association constant) K_I between serine and the chemoreceptors can be estimated because R_{x0} is linear in $\Delta f_c = \ln\left[(1 + c_0/K_I)/(1 + c_0/K_A)\right]$ which can be approximated as $\Delta f_c \approx \ln(1+c_0/K_I)$ when $K_A \gg c_0$. By fitting the amplitudes to $R_{x0} = \ln(1 + c_0/K_I) \times H_x R_{Y0}/[YP]_0$ as shown in Fig. 29, the binding affinity is found to be $K_I \approx 0.39 \pm 0.25$ μM, $H_f R_{Y0}/[YP]_0 = 2.7 \pm 0.6$ Hz, and $H_b R_{Y0}/[YP]_0 = 1.6 \pm 0.4$ Hz. Since R_{Y0} and $[YP]_0$ are parameters of the chemotaxis network that are independent of the motor state, the ratio of the above slopes yields immediately $H_f \simeq 1.7 H_b$. Thus around the physiological $[YP]_0$, the gain of the motor in the CCW state is nearly twice of that in the CW state. The most likely possibility for this difference is that the motor switch has a higher sensitivity to the regulator protein CheY-P when in the CCW state than in the CW state.

While it is difficult to know exactly why there is an asymmetry in the response of the cell in the forward and backward swimming intervals, its motility pattern may provide some clue. In the presence of a chemical gradient, it may be more advantageous to break the symmetry. Note that due to the flick that randomizes cell orientations, a forward displacement cannot retrace the previous backward trajectory but when the cell switches from forward to backward swimming, the cell can backtrack the previous forward trajectory. As a result, if the cell moves down the gradient during a forward run it can revisit the more favorable "pasture" by reversing its motor. However, if the backward swimming is in the unfavorable direction a motor reversal is highly unlikely to orient the cell into the favorable direction. Therefore,

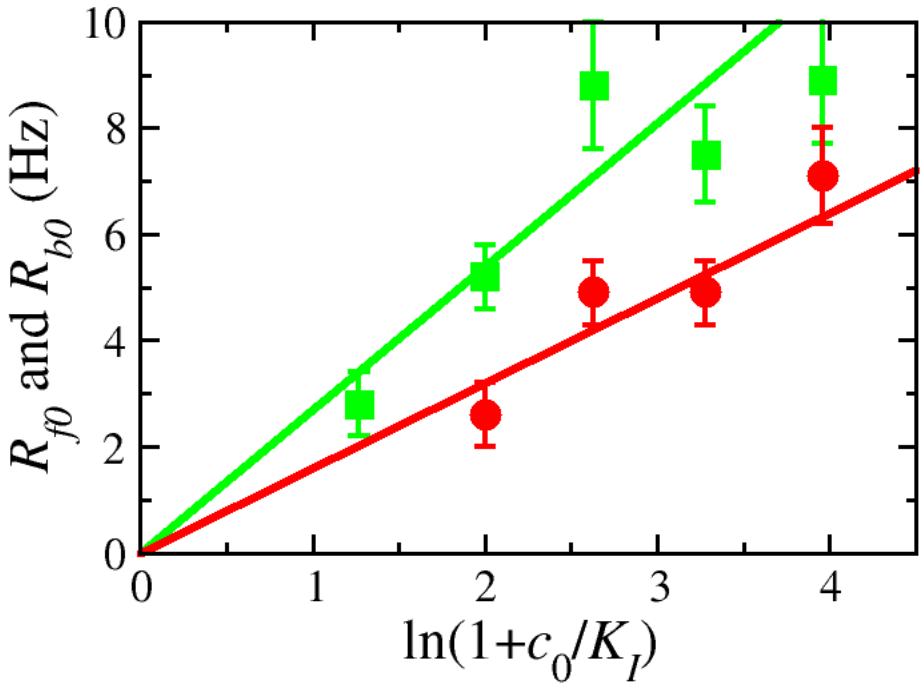

Figure 29: Response amplitudes R_{f0} and R_{b0} as a function of c_0. The measured R_{f0} (green squares) and R_{b0} (red dots) are fitted using $R_{x0} = \ln(1 + c_0/K_I) \times H_x R_{Y0}/[YP]_0$, and the results are displayed by the green and red lines.

forward and backward swimming intervals are not equivalent; the forward swimming is more suitable for exploration but the backward swimming is more suitable for exploitation or localization. Hence, when stimulated by an attractant, k_f should have a stronger response than k_b so that the cell can locate a nutrient source with a weak gradient. An alternative way to illustrate the advantage of the asymmetry is by analyzing the drift velocity v_d in a linear gradient. Combining Eq. 7 in Ref [6] with Eq. 4.17, it can be shown

$$v_d = \frac{v^2 \nabla f_c \tau_0^2 \tau_z \tau_m}{6(\tau_0 + \tau_z)(\tau_0 + \tau_m)} \left(R_{f0} - R_{b0} \frac{\tau_z \tau_m - \tau_0^2}{(\tau_0 + \tau_z)(\tau_0 + \tau_m)} \right), \tag{4.18}$$

when $k_{f0} \simeq k_{b0} \simeq \tau_0^{-1}$, which is a good approximation for YM4. In the above, v is the bacterial swimming speed, $\tau_0 \simeq 0.5$ s is the average swimming interval, $\tau_z \simeq 0.3$ s and $\tau_m \simeq 1.3$ s are the phosphorylation and methylation times according to our measurements. In the limit $K_I \ll c \ll K_A$, $\nabla f_c \simeq \nabla \ln(c) \simeq \nabla c/\bar{c}$, where $\bar{c}$ can be considered the local chemical concentration the bacteria adapt to. We note that since $\tau_z \tau_m - \tau_0^2 > 0$, the second term in the bracket is negative. This negative term results from the memory effect in chemosensing during backtracking, because the gradient sensed by the cell could be opposite to that it currently experiences [22, 6]. Therefore if a large v_d is desired for chemotaxis, Eq. 4.18 shows that a large R_{f0} and a relatively small R_{b0} is beneficial.

4.2.2 Comparing the chemotaxis system in *E. coli* and *V. alginolyticus*

By studying the response of *V. alginolyticus*' flagellar motor to changes in [YP] resulting from step stimuli, we have gained a general picture of how the chemotaxis system of *V. alginolyticus* work together with its motility pattern. Similar to *E. coli*, when a *V. alginolyticus* cell goes up an attractant gradient, increasing binding of the attractant to the receptor reduces CheA activity. This input signal results in a decrease in [YP] through a cascade of protein-protein interactions similar to those in *E. coli*. The decrease in [YP] led to a decrease in switching rates, so the cell can persist in the current swimming direction for a longer time. on the other hand, if the cell descends an attractant gradient, the above process reverses so that the cell is more likely to reverse the motor to change its swimming direction. Despite their contrasting motility patterns, the two bacteria achieves the same

chemotaxis strategy: extending runs in the favorable direction and cutting short those in the unfavorable direction, so that both of them are able to migrate toward an attractant source via a biased random walk.

To apply the same chemotaxis strategy through very different swimming devices, these two bacteria utilize a similar chemotaxis network but tweak the interaction between the output of the network and the flagellar motor to suit their different motility pattens. From the principle of minimum work, modifying the motor seems more practical than modifying the chemotaxis network. The latter involves half a dozen proteins that function collaboratively to optimize the performance. As a result, it might be more difficult to reform the chemotaxis network so that it is compatible with the motor switch than the other way around. These two bacteria descended from the same ancestor but at one point assumed different flagellar arrangements. However, both were able to come up with their own niche to achieve competent chemotaxis through precisely controlled biased random walk. For the marine bacterium *V. alginolyticus*, it has evolved the ability to randomize its swimming direction (by flicking), which at the outset appears to be impossible with a single flagellum. Although the chemotaxis strategy is the same for both bacteria, does it make any difference when the same strategy is applied to two different motility patterns? If so, how does this difference benefit one, the other, or both? In the next chapter, we will compare the chemotaxis behaviors of these two bacteria to address these questions.

5.0 CHEMOTAXIS STRATEGY

Cell motility comes with a big cost and is the reason its associated genes are tightly regulated [48, 35]. A high cost is usually accompanied by a high benefit, suggesting that motility is important for cell survival. The ultimate benefit of bacterial motility is that it allows a cell to sequester essential resources more efficiently in a competitive environment. Pelagic oceans are one of those habitats where the average nutrient level is very low, e.g. the concentration of amino acids is in the range of $\sim 10^{-9}$ M, and evidence suggests that for small bacteria, the availability of metabolizable carbons is the limiting factor for how fast these bacteria can swim [8]. Moreover, in oceans, nutrients appear and disappear in a sporadic fashion, demanding a swift chemical response, a fast swimming speed, and being able to localize near a nutrient patch once it is found. This raises an intriguing question about what motility pattern is well suited for such an environment.

In this chapter we analyze the effect of motility patterns on a cell's ability to migrate in a chemical gradient and to localize at the top of the gradient, the two most important characteristics of bacterial chemotaxis. We will focus on two motility patterns, run-tumble of the 2-step swimmer *E. coli* and run-reverse-flick of the 3-step swimmer *V. alginolyticus*, respectively. Despite different motility patterns used by these two bacteria, both carry out chemotaxis by a biased random walk toward an attractant source. This raises an interesting question about the benefit for a microorganism to adopt the 3-step run-reverse-flick motility pattern instead of the 2-step run-tumble pattern. In a more general sense, one may ask whether certain motility patterns are better suited for a given environment than others. These important questions are difficult to address by laboratory experiments because different microorganisms have different swimming speeds, chemical sensitivities, and intrinsic switching rates. Indeed our experiment presented below shows that *V. alginolyticus* can

migrate in an attractant gradient much faster than *E. coli*, which may be expected because its swimming speed is 2-3 times greater. However, the marine bacteria also form a tighter aggregate at the top of a gradient, which is not evident and appears at odds with its high swimming speed. Hence, unless the problem can be analyzed in an objective manner, there will be no satisfactory answer to these questions.

To overcome this impasse, we resort to mathematical modeling using master equations. A swimming bacterium is represented by a random walker obeying specific local dynamics in a chemical gradient. The 2-step and 3-step swimmers are identical in all aspects except their motility patterns. We found that for a microorganism executing the run-tumble cycles, the master equation is the standard convection-diffusion equation, or in the biological context it is known as the Keller-Segal (KS) equation [38]. On the other hand, for a microorganism executing the run-reverse-flick cycles, the master equation is not of the standard form. It contains an extra flux term, which we show to be negligible. A simple but surprising physical picture emerging from our calculation is that a microorganism can alter its microscopic motility pattern to significantly reduce its diffusivity without compromising the drift velocity in a chemical gradient. This suggests that in oceans, the motility pattern such as run-reverse-flick or for that matter run-reverse is selected for its localization or exploitative behavior rather than its exploration potential.

This chapter is organized in the following fashion. First, the 2-step and 3-step motility patterns, which may be viewed as the chemotactic strategies, are implemented at a microscopic level. This results in differential equations similar to diffusion equations of the telegraph model [63]. By specifying the switching rate $k(x)$ as a function of local chemical concentration $c(x)$, we show that the master equation is equivalent to the KS equation that contains two phenomenological constants, the bacterial diffusivity D and the chemotactic coefficient $\chi = v_d/|\vec{\nabla}c|$, where v_d is the drift velocity and $\vec{\nabla}c$ is the chemical gradient. The KS equation is thus a general description of bacterial chemotaxis, and different motility patterns result in different D and χ. Analytic solutions are then obtained approximately for the one-dimensional case and compared with numerical solutions without approximations. Finally the model calculations are compared with laboratory experiments, where evolution of bacterial profiles in a defined chemical gradient is quantitatively measured.

5.1 THE THEORETICAL MODEL

The movement of a bacterium is akin to that of a random walker. The cell swims with a constant velocity for a time Δ and turns to a new random direction, where Δ is exponentially distributed. A model describing a diffusing particle with a finite mass is thus appropriate for mimicking chemotactic behavior of a bacterium. Here, we are only interested in the long-time diffusive regime of particle dynamics. We define the probability density functions (PDFs) of particles moving in the $\hat{x}$ and $-\hat{x}$ directions as $P(\hat{x}, x, t)$ and $P(-\hat{x}, x, t)$, respectively [63]. These particles are subject to random collisions that occur at rates $k_+(x)$ and $k_-(x)$ when moving respectively in the $\hat{x}$ and $-\hat{x}$ directions. After a collision, the particles have an even chance of continuing in the same or opposite direction. The PDFs are then given by,

$$\frac{\partial P(\hat{x}, x, t)}{\partial t} = -v\frac{\partial P(\hat{x}, x, t)}{\partial x} - \frac{k_+(x)}{2}P(\hat{x}, x, t) + \frac{k_-(x)}{2}P(-\hat{x}, x, t), \tag{5.1}$$

$$\frac{\partial P(-\hat{x}, x, t)}{\partial t} = v\frac{\partial P(-\hat{x}, x, t)}{\partial x} + \frac{k_+(x)}{2}P(\hat{x}, x, t) - \frac{k_-(x)}{2}P(-\hat{x}, x, t). \tag{5.2}$$

In a homogeneous medium, the collision rates are expected to be constant, $k_\pm(x) = k_0$, independent of x. However, for chemotaxis, a bacterium follows chemical cues by modulating $k_\pm(x)$: If the bacterium swims up an attractant gradient, it lowers the switching rate, and if it swims down the gradient, it increases the switching rate.

Previous experiments have shown that a bacterium performs chemosensing by temporal comparison. In *E. coli* for example, the chemoreceptors average the receptor occupancy by chemoeffectors in the present one second and compare it with that of the previous three seconds [65]. The result of the comparison is used to alter the phosphorylation level of the regulator protein CheY that determines the flagellar motor switching probability. As discussed in the previous chapter, *V. alginolyticus* also perform temporal comparison, but the response time is shorter. Hence, even though bacterial chemotaxis is modeled as a random walk, the actual process is non-Markovian because $k_\pm(x)$ is determined by the history of a particular trajectory [28, 18]. Because of this memory effect, a rigorous treatment requires averaging over all possible trajectories, which is beyond the scope of this work. The bacterial sensory response can be significantly simplified if the chemoeffector, say an

attractant, $c(x)$ has a shallow gradient that does not change much during a swimming interval, $v|\partial^2 c/\partial x^2| \ll k_0|\partial c/\partial x|$. In this case, the switching rate is a linear function of the chemical gradient $k_\pm(x) \approx k_0 \mp \Delta k(x)$ [63] with $\Delta k(x) = gv\partial c(x)/\partial x$ and g being a gain factor. In an early work by Mesibov et al., it was shown that instead of linear sensing, bacteria actually use logarithmic sensing to respond to a chemical cue [54]. In this case, $\Delta k(x) = (g'v/c(x))\,\partial c(x)/\partial x$, where g' is a constant. A recent work showed that $c(x)$ in $g \equiv g'/c(x)$ can be replaced by $\bar{c}$, the average concentration experienced by the bacterium in an attractant profile if $\partial c(x)/\partial x \ll k_0 c(x)/v$ [34].

5.1.1 The master equation for 2-step swimmers

For the run-tumble motility pattern and in a shallow gradient, Eqs. 5.1 and 5.2 can be used directly by replacing $k_\pm$ with $k_0 \mp \Delta k$. This yields,

$$\frac{\partial P(\hat{x},x,t)}{\partial t} = -v\frac{\partial P(\hat{x},x,t)}{\partial x} - \frac{k_0 - \Delta k(x)}{2}P(\hat{x},x,t) + \frac{k_0 + \Delta k(x)}{2}P(-\hat{x},x,t), \tag{5.3}$$

$$\frac{\partial P(-\hat{x},x,t)}{\partial t} = v\frac{\partial P(-\hat{x},x,t)}{\partial x} + \frac{k_0 - \Delta k(x)}{2}P(\hat{x},x,t) - \frac{k_0 + \Delta k(x)}{2}P(-\hat{x},x,t). \tag{5.4}$$

Adding and subtracting Eqs. 5.3 and 5.4, the following equations are obtained,

$$\frac{\partial P(x,t)}{\partial t} = -\frac{\partial J(x,t)}{\partial x}, \tag{5.5}$$

$$\frac{\partial J(x,t)}{\partial t} = -v^2\frac{\partial P(x,t)}{\partial x} - k_0 J(x,t) + v\Delta k(x)P(x,t), \tag{5.6}$$

where $P(x,t) = P(\hat{x},x,t)+P(-\hat{x},x,t)$ is the the total probability and $J(x,t) = v(P(\hat{x},x,t)-P(-\hat{x},x,t))$ is the flux. Taking the time derivative of Eq. 5.5 and replacing $\frac{\partial J}{\partial t}$ by Eq. 5.6 gives,

$$\frac{\partial^2 P(x,t)}{\partial t^2} = -\frac{\partial}{\partial x}\left[-v^2\frac{\partial P(x,t)}{\partial x} - k_0 J(x,t) + v\Delta k(x)P(x,t)\right]. \tag{5.7}$$

Since only the long-time behavior ($k_0 t \gg 1$) of the bacterial population is of interest, it is justifiable to set $\partial^2 P(x,t)/\partial t^2 = 0$. This yields,

$$\frac{\partial J(x,t)}{\partial x} = -\frac{v^2}{k_0}\frac{\partial^2 P(x,t)}{\partial x^2} + \frac{v}{k_0}\frac{\partial\left(\Delta k(x) P(x,t)\right)}{\partial x}. \tag{5.8}$$

Inserting this equation into Eq. 5.5, we arrive at the master equation for the 2-step swimmer,

$$\frac{\partial P_E(x,t)}{\partial t} + \frac{\partial(v_E(x) P_E(x,t))}{\partial x} = D_E \frac{\partial^2 P_E(x,t)}{\partial x^2}, \tag{5.9}$$

where the subscript E stands for *E. coli*, $v_E(x) = v\Delta k(x)/k_0$ is the drift velocity and $D_E = v^2/k_0$ is the diffusivity. We observed that for the 2-step swimmer, the master (or KS) equation can be derived with the single assumption $k_0 t \gg 1$. As we shall see, this is insufficient for the 3-step swimmer.

5.1.2 The master equation for 3-step swimmers

The major difference between a 2-step and a 3-step swimmer is that the latter has motility even when the flagellar motor rotates in CW direction, backtracking its forward path. For the 3-step swimmer, therefore, there are four possibilities depending on the swimming direction and the state of motor rotation: $(\hat{x}, CCW)$, $(-\hat{x}, CCW)$, $(\hat{x}, CW)$, and $(-\hat{x}, CW)$. The corresponding PDFs evolve in time according to,

$$\begin{aligned}\frac{\partial P_{CCW}(\hat{x},x,t)}{\partial t} &= -v\frac{\partial P_{CCW}(\hat{x},x,t)}{\partial x} - (k_0 - \Delta k) P_{CCW}(\hat{x},x,t) \\ &+ \frac{k_0 - \Delta k}{2} P_{CW}(\hat{x},x,t) + \frac{k_0 + \Delta k}{2} P_{CW}(-\hat{x},x,t),\end{aligned} \tag{5.10}$$

$$\begin{aligned}\frac{\partial P_{CCW}(-\hat{x},x,t)}{\partial t} &= v\frac{\partial P_{CCW}(-\hat{x},x,t)}{\partial x} - (k_0 + \Delta k) P_{CCW}(-\hat{x},x,t) \\ &+ \frac{k_0 - \Delta k}{2} P_{CW}(\hat{x},x,t) + \frac{k_0 + \Delta k}{2} P_{CW}(-\hat{x},x,t),\end{aligned} \tag{5.11}$$

$$\frac{\partial P_{CW}(\hat{x},x,t)}{\partial t} = -v\frac{\partial P_{CW}(\hat{x},x,t)}{\partial x} - (k_0 - \Delta k) P_{CW}(\hat{x},x,t) + (k_0 + \Delta k) P_{CCW}(-\hat{x},x,t), \tag{5.12}$$

$$\frac{\partial P_{CW}(-\hat{x},x,t)}{\partial t} = v\frac{\partial P_{CW}(-\hat{x},x,t)}{\partial x} - (k_0+\Delta k)P_{CW}(-\hat{x},x,t) + (k_0-\Delta k)P_{CCW}(\hat{x},x,t). \tag{5.13}$$

In the above, the cyclic run-reverse-flick motility pattern is explicitly implemented, i.e., when a bacterium swims in a CCW state, a motor reversal simply makes the cell swim in the opposite direction, but when a bacterium swims in a CW state, a motor reversal causes the cell to flick and swim either in its current or opposite direction with equal probability.

Similar to the 2-step case, we define the total probability $P(x,t) = P_{CCW}(\hat{x},x,t) + P_{CCW}(-\hat{x},x,t)+P_{CW}(\hat{x},x,t)+P_{CW}(-\hat{x},x,t)$ and the flux $J = v(P_{CCW}(\hat{x},x,t)+P_{CW}(\hat{x},x,t) - P_{CCW}(-\hat{x},x,t)-P_{CW}(-\hat{x},x,t))$ for the 3-step swimmer. Summing up Eqs. 5.10-5.13 yields the equation of conservation of total number of bacteria,

$$\frac{\partial P(x,t)}{\partial t} = -\frac{\partial J(x,t)}{\partial x}, \tag{5.14}$$

which is expected. However, the flux equation is more complicated with the result,

$$\frac{\partial J(x,t)}{\partial t} = -v^2\frac{\partial P(x,t)}{\partial x} - 2k_0 J(x,t) + 2v\Delta k(x)P(x,t) + k_0\delta J_{CW}(x,t), \tag{5.15}$$

where $\delta J_{CW}(x,t) \equiv J_{CW}(x,t) - \frac{v\Delta k(x)}{k_0}P_{CW}(x,t)$ is the extra flux term, which makes this equation different from Eq. 5.6. Following the same procedure as above, i.e., taking the time derivative of Eq. 5.14 and replacing $\frac{\partial J}{\partial t}$ with Eq. 5.15, we found,

$$\frac{\partial P(x,t)}{\partial t} = \frac{v^2}{2k_0}\frac{\partial^2 P(x,t)}{\partial x^2} - \frac{v}{k_0}\frac{\partial\left(\Delta k(x)P(x,t)\right)}{\partial x} - \frac{1}{2}\frac{\partial\delta J_{CW}(x,t)}{\partial x}. \tag{5.16}$$

In the moving frame of bacteria, the steady state condition requires $\frac{d}{dt}... \equiv (\frac{\partial}{\partial t} \pm v\cdot\frac{\partial}{\partial x})... = 0$. It follows from Eqs. 5.10-5.13 that the following conditions must be satisfied: $P_{CW}(\hat{x},x,t) = P_{CCW}(\hat{x},x,t)$, $P_{CCW}(-\hat{x},x,t) = \frac{k_0-\Delta k}{k_0+\Delta k}P_{CCW}(\hat{x},x,t)$, and $P_{CW}(-\hat{x},x,t) = \frac{k_0-\Delta k}{k_0+\Delta k}P_{CCW}(\hat{x},x,t)$. Thus $P_{CW}(x,t)\,(\equiv P_{CW}(\hat{x},x,t)+P_{CW}(-\hat{x},x,t)) = \frac{2k_0}{k_0+\Delta k}P_{CCW}(\hat{x},x,t)$ and $\Delta P_{CW}(x,t)\,(\equiv P_{CW}(\hat{x},x,t)-P_{CW}(-\hat{x},x,t)) = \frac{2\Delta k}{k_0+\Delta k}P_{CCW}(+\hat{x},x,t)$. The above relations show (i) $J_{CW}\,(\equiv v\Delta P_{CW}) \propto \Delta k$ and (ii) $\delta J_{CW} = J_{CW} - v\frac{\Delta k}{k_0}P_{CW} \propto (\Delta k)^2$. Physically,

δJ_{CW} is a measure of the deviation from detail balance, and when $\Delta k/k_0 \ll 1$, it can be ignored. This is confirmed by numerical calculations in which all terms are included. Dropping the last term in Eq. 5.16, we obtained the master equation for the 3-step swimmer,

$$\frac{\partial P_V(x,t)}{\partial t} + \frac{\partial (v_V(x) P_V(x,t))}{\partial x} = D_V \frac{\partial^2 P_V(x,t)}{\partial x^2}, \tag{5.17}$$

where the subscript V stands for *V. alginolyticus*, $v_V(x) = v\Delta k(x)/k_0$, and $D_V = v^2/2k_0$. We note that by dropping the $\partial \delta J_{CW}/\partial x$ term the master equation for the 3-step swimmer is mathematically identical to that of the 2-step swimmer. Importantly, we found that the bacterial diffusivity of the 3-step swimmer is a factor of two smaller than the 2-step swimmer, $D_V = D_E/2$, but the drift velocity is the same for both, $v_V = v_E = v_d (\equiv v\Delta k/k_0)$. The latter is unexpected because due to backtracking, one anticipates $v_V < v_E$. The result is moreover counter-intuitive from a physics perspective: For a colloidal particle in an external field for example, diffusion and drift are related; when one increases the other must increase because both share the same frictional factor.

The above finding has important biological implications because it shows that by altering the motility pattern, a microorganism can reduce its diffusivity *without compromising* its drift velocity, a niche that can be exploited by the microorganism. Indeed, Eqs. 5.9 and 5.17 provide clues about how well a 2-step and 3-step swimmer can perform chemotaxis in a chemical gradient. It shows that for everything being equal, such as the swimming speed v, the switching rate k_0, and the gain factor g (or g'), the 3-step swimmer can aggregate around a source of an attractant more tightly than its 2-step counterpart, allowing a higher exposure to nutrients. Such a trait is very significant for competitive foraging in habitats where nutrients are scarce and localized. The high ability for the cell to localize evidently comes with a cost. It reduces the chance for the 3-step swimmer to explore habitats efficiently. However, it may be argued that in vast oceans searching is unproductive unless a chemical cue is present. In this case to follow closely and rapidly an existing chemical cue is more important. This exploitative behavior is encoded in the swimming pattern of *V. alginolyticus*.

5.1.3 Analytical and numerical solutions of the master equations

It is difficult to obtain analytical solutions to the master equation with an arbitrary drift velocity $v_d(x)$. However, when the chemical gradient is linear, Δk and hence v_d become constant and the problem is simplified. Below we attempt to find analytical solutions in the domain $[-L,\ L]$ with different initial conditions. Using the method of separation of variables, we found that the solution to the master equation is given by,

$$\begin{aligned} P(x,t) =& \frac{q'}{\sinh(2q'L)} \exp(2q'x) \\ &+ \exp(q'x) \left[\sum_{n=1,2,..} A_n \psi_n(x) \exp(-\lambda_n t) + \sum_{m=0,1,2,..} B_m \phi_m(x) \exp(-\lambda_m t) \right] \end{aligned} \tag{5.18}$$

where $q' = v_d/2D$ is the wavenumber characterizing the steady-state profile, $\psi_n(x)$ and $\phi_m(x)$ are the eigenfunctions, λ_n and λ_m are the corresponding decay rates. In terms of wavenumbers $q_n = \frac{\pi n}{L}$ and $q_m = \frac{\pi(2m+1)}{2L}$, they are given by,

$$\begin{cases} \psi_n(x) = \psi_{0n} \left(q_n \cos(q_n x) + q' \sin(q_n x) \right) & , \\ \phi_m(x) = \phi_{0m} \left(q' \cos(q_m x) - q_m \sin(q_m x) \right) & , \end{cases} \tag{5.19}$$

$$\begin{cases} \lambda_n = & \lambda_0 \left[1 + \left(\frac{q_n}{q'} \right)^2 \right], \\ \lambda_m = & \lambda_0 \left[1 + \left(\frac{q_m}{q'} \right)^2 \right], \end{cases} \tag{5.20}$$

where $\lambda_0 = Dq'^2 = v_d^2/4D$, $\psi_{0n} = \frac{1}{\sqrt{L(q'^2+q_n^2)}}$, $\phi_{0m} = \frac{1}{\sqrt{L(q'^2+q_m^2)}}$, and m and n are positive integers.

Consider the situation when the bacteria are released at $x = 0$, and we watch how they spread in space and time. The initial condition in this case is $P(x,0) = \delta(x)$, and it yields the Fourier amplitudes $A_n = \psi_n(0)$ and $B_m = \phi_m(0)$. Figure 30 displays our analytical solutions of $P(x,t)$ for the 2-step (blue lines) and 3-step (purple lines) swimmers, and the results are compared with the numerical solutions (green squares and red circles, respectively) using the full equations, Eqs. 5.3-5.4 and Eqs. 5.10-5.13. Because of the approximations made in deriving Eq. 5.9 and Eq. 5.17, specifically $\partial^2 P/\partial t^2 \simeq 0$ and $\delta J_{CW} \simeq 0$, the numerical

method provides a quantitative means to check their validity. In all numerical calculations (see Materials and Methods), we set $\Delta x = 0.1$ and $\Delta t = 1$ so that the bacterial swimming speed is $v = \Delta x/\Delta t = 0.1$, the switching rate $k_0 = 0.1/\Delta t$ (or the mean swimming interval $k_0^{-1} = 10\Delta t$), and the change in switching rate $\Delta k = k_0/10$. One observes that for the 2-step swimmer, the analytical and numerical solutions are nearly identical, indicating that the short-time, ballistic-like motion of bacteria does not contribute significantly to the evolution of the bacterial profile. For the 3-step swimmer, on the other hand, small discrepancies can be seen at the peak of bacterial profiles, indicating that in this region the extra flux term, $\partial \delta J_{CW}/\partial x$, in Eq. 5.16 has a small but discernible contribution. However, the overall good agreement between the analytic and the numerical solutions demonstrates that (i) our derivation of the the master equations is sound, and (ii) the approximations are reasonable.

Importantly, the numerical solutions support our analysis that the microscopic motility patterns do not affect the drift velocity v_d. They only modify the bacterial diffusivity D. This is illustrated by Figure 30, which shows that the two bacteria migrate up the chemical gradient with identical speed, but the bacterial pack for the 3-step swimmer is narrower than its 2-step counterpart. Our calculations also show that because of the spatial separation between the chemical source ($x = L$) and the initial bacterial position ($x = 0$), a waiting time of $t_v \sim L/v_d$ is required for the bacteria to aggregate around the top of the attractant concentration. As delineated by Figure 30 F, the steady state is reached when $t/t_v \simeq 2$.

For a better comparison with our experimental measurements, we also calculated evolution of bacterial profiles starting from a uniform distribution, $P(x, 0) = 1/2L$. The Fourier coefficients in this case are given by,

$$\begin{cases} A_n = & 2q' q_n \psi_{0n}^3 \sinh(q'L)\cos(q_n L), \\ B_m = & 2q' q_m \phi_{0m}^3 \cosh(q'L)\sin(q_m L). \end{cases} \tag{5.21}$$

The analytical and numerical results are plotted in Figure 31. We noticed that in this case the bacterial profiles develop near the boundaries first and then spread into the interior of the sample. The problem in hand involves multiple length scales, L, q'^{-1}, and $q_{m,n}^{-1}$, and it is useful to know their corresponding time scales in an experiment. Eq. 5.20 makes it clear that the relaxation rate for the attainment of a quasi-steady state is given by $\lambda_0 = Dq'^2 = v_d^2/4D$.

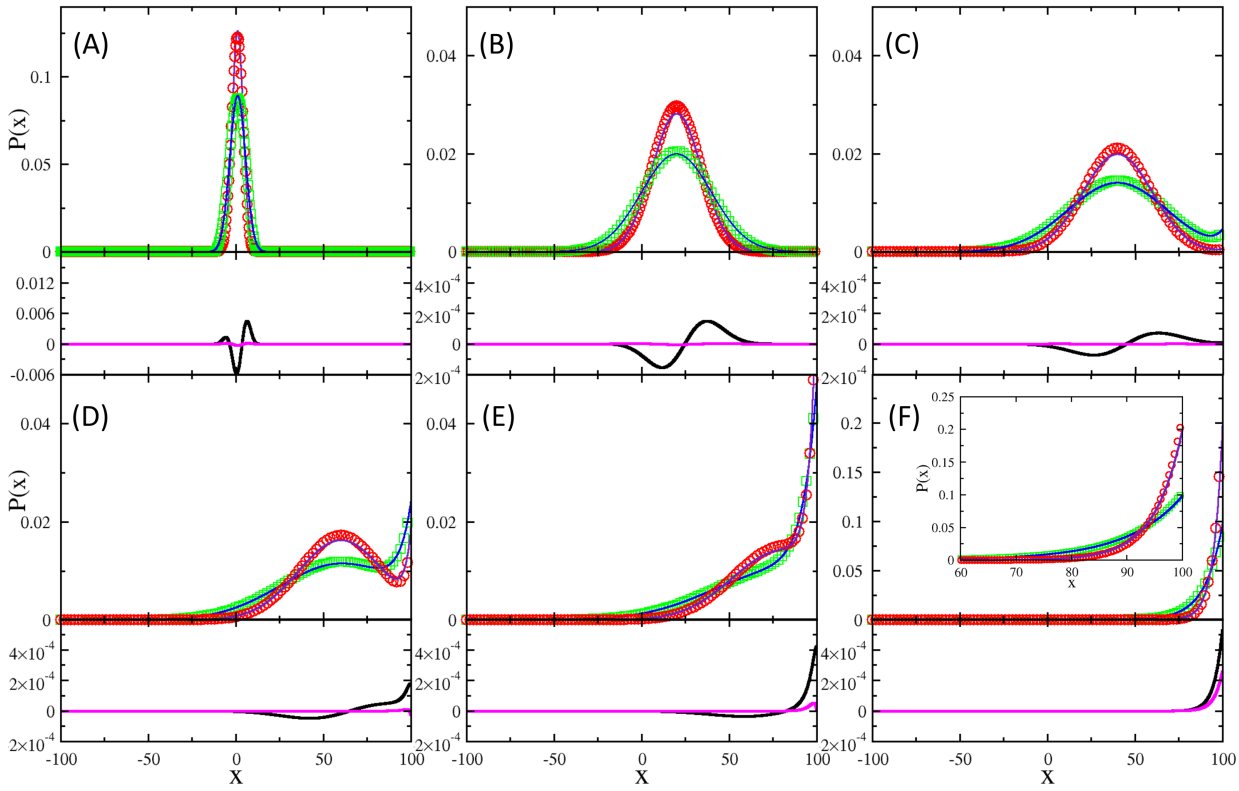

Figure 30: Evolution of $P(x,t)$ starting from the δ-distribution $P(x,0)=\delta(x)$. The bacterial profiles of the 2-step (blue line) and 3-step (purple line) swimmers, calculated based on Eq. 5.18 at reduced times $t/t_v = 0.01$, 0.2, 0.4, 0.6, 0.8, and 2, are plotted in (A-F) respectively. Here $t_v(\equiv L/v_d) = 10^4\Delta t$ and $\Delta t = 1$ is the computation step. As seen the steady-state exponential profiles are formed at $t/t_v \simeq 2$. The green squares and red circles are respectively the numerical solutions for Eqs. 5.3-5.4 and 5.10-5.13. The inset of (F) is the close-up for the steady-state profiles, where colored symbol and line designations are the same as above. Beneath each PDF, the first two terms $\frac{v^2}{2k_0}\frac{\partial^2 P}{\partial x^2} - v\frac{\Delta k}{k_0}\frac{\partial P}{\partial x}$ (black lines) and the last term $\frac{1}{2}\frac{\partial}{\partial x}\delta J_{cw}$ (magenta lines) on the right hand side of Eq. 5.16 are plotted based on the numerical solutions. As seen, the extra flux term is significant only for late times. However, the analytic calculation without this term still yields a quantitatively good result as demonstrated in the inset of (F).

Since $v_d = v(\Delta k/k_0)$ and $D = v^2/(\epsilon k_0)$, we found $\lambda_0 = \frac{\epsilon k_0}{4}\left(\frac{\Delta k}{k_0}\right)^2$, where $\epsilon = 1$ for *E. coli* and $\epsilon = 2$ for *V. alginolyticus*. This indicates that the profile formation time λ_0^{-1} is essentially independent of the bacterial swimming speed v but depends on the switching rate k_0, the sensitivity characterized by $\Delta k/k_0$, and the motility pattern specified by ϵ. Due to the relatively large system size in a typical experiment or in a natural habitat, $L \gg q'^{-1}$, the drift time L/v_d on the scale of the system size, or for that matter the diffusion time L^2/D, is irrelevant. For a large system, therefore, it is expected that a quasi-steady state with a defined profile develops near the peak of the chemical profile over the time scale λ_0^{-1}. For longer times, $\lambda_0^{-1} < t < L/v_d$, the profile increases in amplitude with its exponential form $\sim \exp(2q'x)$ more-or-less preserved. Our calculation displayed in Figure 31 is consistent with this picture, where $\lambda_0^{-1} = 4000\Delta t$ and $2000\Delta t$ for the 2-step and 3-step swimmer, respectively.

5.2 THE EXPERIMENTAL MEASUREMENTS

To assess how motility patterns affect the ability of bacteria to migrate and accumulate around a source of attractant, systematic measurements were conducted using *V. alginolyticus* and *E. coli* expressing yellow fluorescent proteins (YFP). Our aim is to extract the typical size of the bacterial profile q'^{-1}, the drift velocity v_d, and to use them to determine k_0 and Δk. In the measurement, a micropipette filled with serine solutions ($c_0 = 0.05$, 0.5, 5 and 50 mM) was used to create an attractant gradient [80]. Although the chemical profile decreases sharply close to the tip, its tail decays slowly and is approximately linear. At the beginning of the experiment, bacteria were stirred so that their density is uniform, $\sim 10^7$/mL. Images of the bacterial profile around the tip were then acquired at different times using a fluorescence microscope equipped with a CCD camera. Figure 32 displays the time-dependent bacterial profiles obtained with $c_0 = 0.5$ mM, which represents a nearly maximal response for both bacteria. In the plot, the normalized bacterial density $B(r,t)/B_0(0)$ is plotted as a function of radial distance r from the tip, where $B_0(r)$ is the steady-state bacterial profile. For convenience, each bacterial profile is color coded according to the bar at the right of

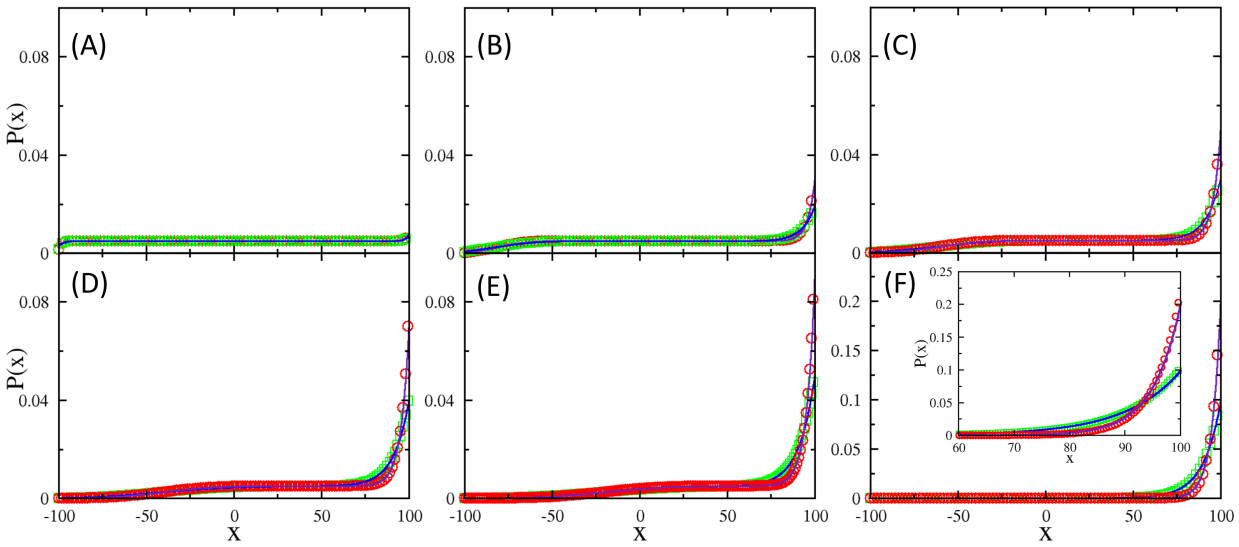

Figure 31: Evolution of $P(x,t)$ starting from the flat distribution $P(x,0) = 1/2L$. The bacterial profiles of the 2-step (blue lines) and 3-step (purple lines) swimmers, calculated based on Eq. 5.18 at reduced times $t/t_v = 0.01$, 0.2, 0.4, 0.6, 0.8, and 2, are plotted in (A-F) respectively. The numerical results based on Eqs. 5.3-5.4 and 5.10-5.13 are plotted using green squares and red circles for the 2-step and 3-step swimmers. The inset in (F) is the close-up view of the same figure. Note that the shapes of the bacterial profiles near the peak of the chemical concentration $x = L$ form at early t where $t/t_v \ll 1$. Afterward, the peak grows in height but the shapes of the profiles remain more-or-less the same.

the figures. Also displayed in Figure 32 are the normalized steady-state bacterial profiles $B_0(r)/B_0(0)$ (thick green lines) and the normalized serine profile $c(r)/c(0)$ (thick orange line). One observes that $B(r,t)$ evolves from a uniform distribution at $t = 0$ and gradually becomes peaked at $r = 0$ over time. Except near the tip, the bacterial distribution for large t can be well described by an exponential function, suggesting that it is reasonable to assume that the serine gradient at $r > 20$ μm is approximately linear. Below we attempt to draw *qualitative* information from the tail part of the serine distribution.

Figure 32 shows that even though *V. alginolyticus*' profile is broad compared to the chemical distribution, it is much narrower than *E. coli*'s, indicating that the marine bacterium can cluster around a small source much better. We also noticed that it takes much less time for *V. alginolyticus*' profile to reach the steady state than *E. coli* does. To quantify formation dynamics of the profiles we measured the half-height-radius $r_{1/2}(t)$ of $B(r,t)$ as a function of time, and the data is displayed in the insets of Figures 32(A, B) We found that this data can be adequately mimicked by the exponential function (red lines), $r_{1/2}(t) = r_0 \exp(-t/\tau) + r_\infty$, where $\tau = 107$ s and $r_\infty = 151$ μm for *E. coli* and $\tau = 31$ s and $r_\infty = 23$ μm for *V. alginolyticus*. The differences seen here are indeed striking.

The above measurements give the characteristic sizes r_∞ of the bacterial profiles for *V. alginolyticus* and *E. coli* that can be identified as $(2q')^{-1} = D/v_d$ in Eq. 5.18. From Eqs. 2.11 and 2.12 in Chapter 2, it was calculated that $D_E \simeq 180$ μm^2, and $D_V \simeq 66$ μm^2. The profile size r_∞ and the diffusivity D allow us to determine the drift velocity of the bacteria using the relationship $v_d \equiv 2q'D$ or D/r_∞. We found $v_d \simeq 2.8$ μm/s and 1.3 μm/s for *V. alginolyticus* and *E. coli*, respectively. To ascertain that these values are reasonable, we also estimated v_d using the conservation law $\frac{\partial P}{\partial t} = -\vec{\nabla} \cdot \vec{J}$, which upon integrating over a disk of area $A = \pi r_\infty^2$ yields (see Materials and methods),

$$v_d = -\left(\frac{\Delta \int_A P(r,t) dA}{\Delta t} - 2\pi r_\infty D \frac{\partial P(r,t)}{\partial r}|_{r=r_\infty}\right)/2\pi r_\infty P(r_\infty, t). \tag{5.22}$$

From measured $B(r,t)$ ($\propto P(r,t)$) in Figure 32, the amount of bacterial accumulation within A over a time interval Δt as well as the derivative $\partial P/\partial r$ can be evaluated. This procedure allows us to find the average drift velocities $v_d \simeq 2.4$ μm/s and 1.6 μm/s for *V. alginolyticus*

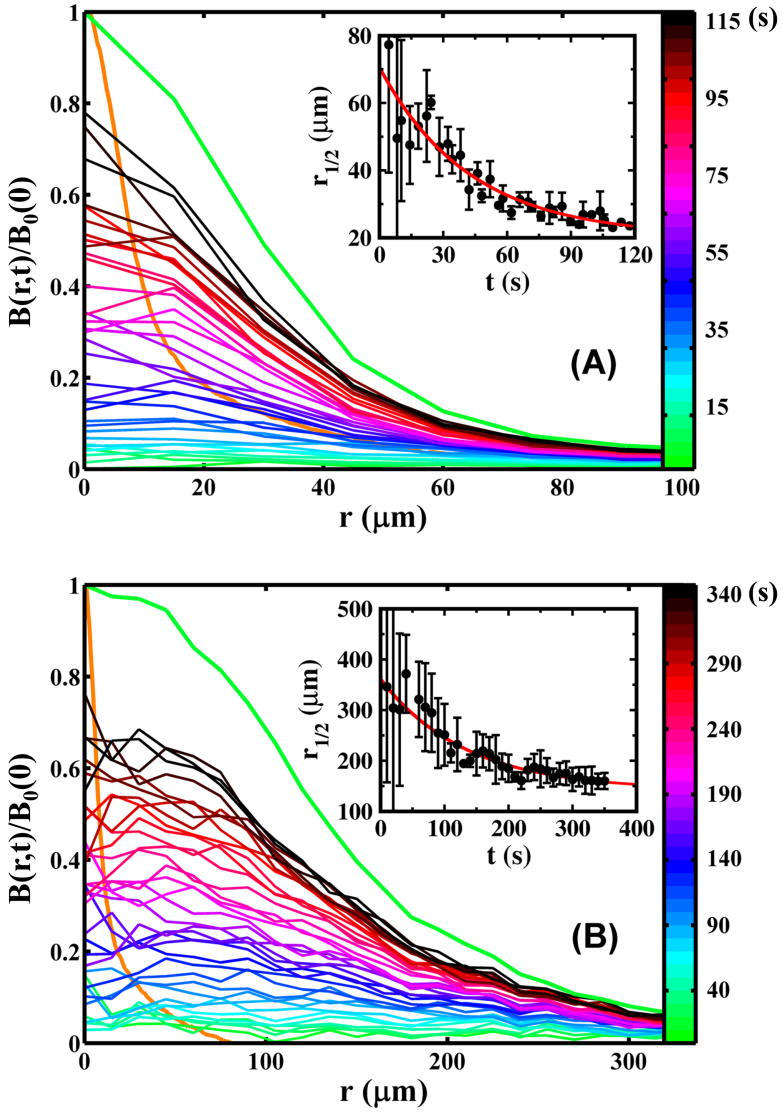

Figure 32: Normalized bacterial profile $B(r,t)/B_0(0)$ for *V. alginolyticus* (A) and *E. coli* (B). The individual runs are color coded according to the color bars. Note the significantly different spatial and temporal scales used in these plots, indicating that the swarm size and the aggregation time are quite different for the two bacteria. As a comparison, the steady-state bacterial $B_0(r)$ and the serine $c(r)$ profiles are displayed by the thick green and orange curves, respectively. The insets represent the half-height-radii $r_{1/2}(t)$ of the bacterial profiles $B(r,t)$. The red lines are exponential fits as described in the main text.

and *E. coli,* respectively, showing that the two methods are reasonably consistent with each other.

Based on our mathematical model, the relatively large v_d for *V. alginolyticus* could be due to its high swimming velocity v or its large chemical sensitivity $\Delta k/k_0$. To make an objective comparison, we need to know the sensitivity $\Delta k/k_0$ of the two bacteria. Since $\Delta k/k_0$ is given by the velocity ratio v_d/v, it can be determined from our measurement. Interestingly, for $c_0 = 0.5$ mM serine, we found $\Delta k/k_0 = v_d/v \simeq 0.06 \pm 0.01$ is about the same for both bacteria. This allows us to conclude that the large drift velocity v_d seen in *V. alginolyticus* is mostly due to its high swimming speed v.

We next investigated how bacterial aggregation is affected by the serine concentration c_0 in the micropipette. We focused on two important aspects of the bacterial chemotaxis, the formation time and the ability to localized near the source of the attractant. As shown in Figures 33 (A, B), *V. alginolyticus* (red circles) is able to respond to a wide range of c_0 with only little change in the aggregation time. On the other hand, *E. coli* (green squares) has a much stronger dependence on c_0 but the range of the response is narrower. Specifically, we found that (i) for $c_0 \leq 0.05$ mM, the bacterial density around the tip increased very little, suggesting that *E. coli* is not sensitive enough to localize at low serine concentrations. (ii) For $c_0 = 50$ mM, the bacterial profile is diffusive and evolves very slowly, resulting in a large uncertainty in the measured τ (the last data point in B). The observation suggests that *E. coli*'s sensory system may be saturated for $c_0 \geq 50$ mM. Figures 33 (C, D) displays the profile size r_∞ for *V. alginolyticus* and *E. coli*, respectively. We found again that for *V. alginolyticus*, r_∞ is weakly dependent on c_0, i.e. varying c_0 by three orders of magnitude, r_∞ changes by only about a factor of two. In contrast, for *E. coli*, the change in r_∞ is more noticeable as c_0 is varied. The data presented in Figures 33(A-D) shows a remarkable correlation between r_∞ and τ for both bacteria. Such correlation however is expected because r_∞/τ is proportional to v_d. These plots therefore suggest that for both bacteria v_d does not change significantly as c_0 varies.

An attractive feature of the master (KS) equation is its simplicity, consisting of only two phenomenological constants, D and χ. This suggests that microscopic dynamics, or details of bacterial motions, is irrelevant in long times. In other words given the chemical distribution

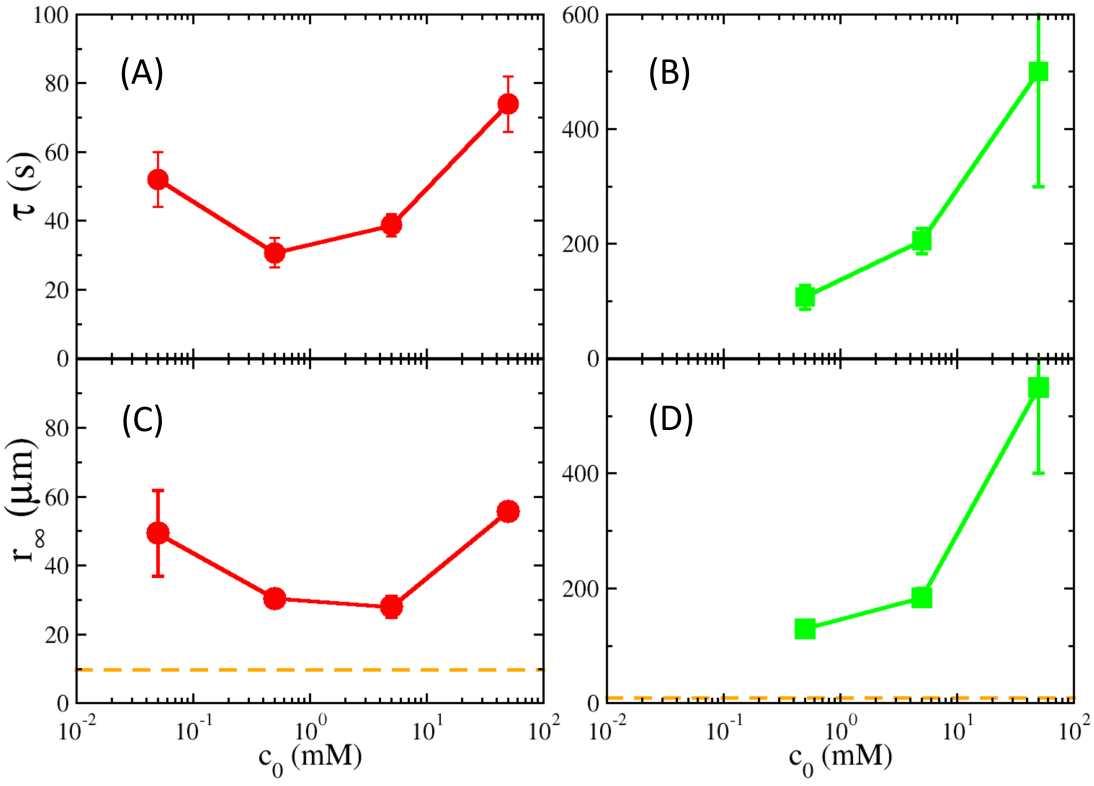

Figure 33: Bacterial aggregation behavior as a function of serine concentration c_0 in the micropipette. The profile formation time τ (A, B) and the steady-state half-height-radius r_∞ (C, D) vs. c_0 are presented for *V. alginolyticus* (red circles) and *E. coli* (green squares). The orange dashed line marks the half-height-radius, 9.7 μm, of the serine profile $c(r)$. Note the very different spatial and temporal scales used in (A, C) and (B, D). Note also that both bacteria are the most sensitive to $c_0 \sim 1$ mM, where the cluster sizes are small and their formation times short.

$c(r)$, the steady-steate bacterial profiles $B_0(r)$ should have the same mathematical form albeit the relevant spatial scales may be different. This difference should be accounted for by making r non-dimensional. In Figure 34, it is demonstrated that by rescaling the profile width, $r \to r/a$, the steady-state profiles for *V. alginolyticus* and *E. coli* (thick green lines) in Figure 32, can be collapsed, suggesting that bacteria with different motility patterns can be described by a single macroscopic equation. The above scaling procedure yields the profile width of *V. alginolyticus* to be ~ 5.3 times narrower than that of *E. coli*, which is consistent with the early analysis.

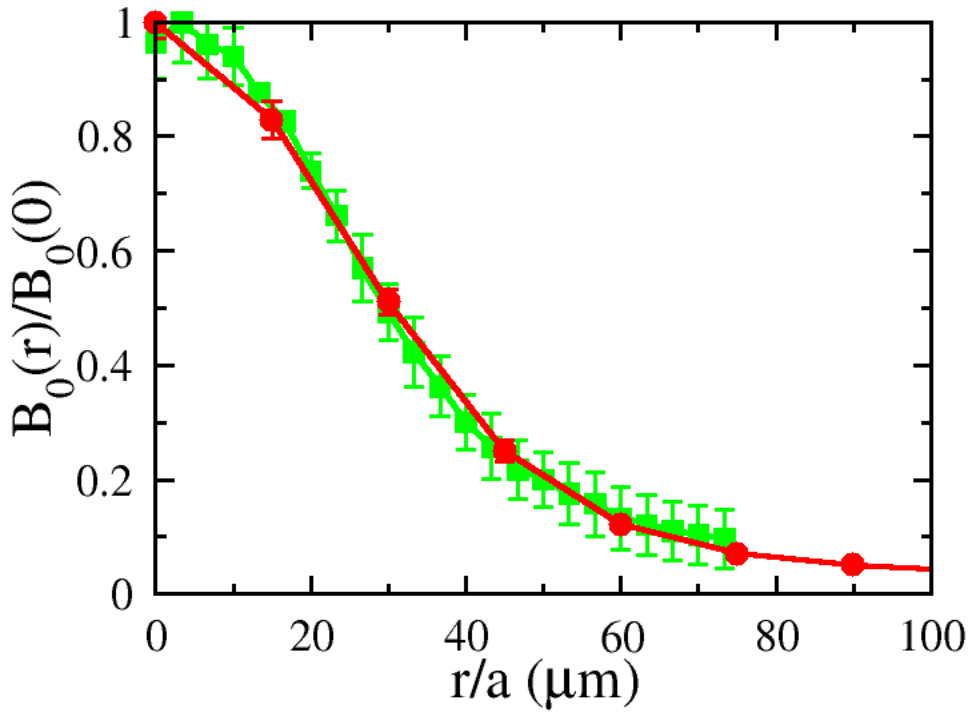

Figure 34: The rescaled steady-state bacterial profiles around a source of attractant. Here, $B_0(r)/B_0(0)$ for *V. alginolyticus* and *E. coli* are displayed by red circles and green squares, respectively. Here, a is a scaling factor for the horizontal axis. Using $a = 1$ for *V. alginolyticus* and $a = 5.3$ for *E. coli*, the steady-state profiles of both bacteria can be collapsed, showing that they belong to the same family of functions.

A more stringent test of the master (KS) equation is the accuracy by which the bacterial

concentration profile $B(\vec{r},t)$ can be predicted by the chemical profile $c(\vec{r})$. For simplicity, let us consider the steady-state distribution $B_0(\vec{r})$, which satisfies the condition $\vec{J} = -D\vec{\nabla}B_0 + \chi B_0\vec{\nabla}c = 0$. Two cases are of biological relevance: (i) χ is a constant and (ii) χ is a function of $c(\vec{r})$. For the first case, a straight forward integration yields the relation between $B_0(\vec{r})$ and $c(\vec{r})$ with the result, $B_0(\vec{r}) = B_\infty \exp[g(c(\vec{r}) - c_\infty)]$, where c_∞ and B_∞ are the chemical and bacterial concentrations at infinity, and $g \equiv \chi/D$ is the gain factor. This result suggests that for a given $c(\vec{r})$, the profiles for *V. alginolyticus* and *E. coli* should be the same when properly scaled according to $\frac{D}{\chi}\ln(B_0(\vec{r})/B_\infty) = c(\vec{r}) - c_\infty$. For the second case, we assume the logarithmic-sensing scheme, $\chi(c(\vec{r})) = \chi'/c(\vec{r})$, where χ' is a constant. Again by integration, we obtained $B_0(\vec{r})/B_\infty = (c(\vec{r})/c_\infty)^{g'}$, where $g' = \chi'/D$ is the dimensionless gain. We found that (i) is not consistent with our measurements because if $B_0(\vec{r})$ indeed depends exponentially on $c(\vec{r})$, when $c(\vec{r})$ changes by orders of magnitude, the bacterial concentration would increase much more rapidly than observed. For example in the experiment with *V. alginolyticus*, when c_0 increases from 0.05 mM to 0.5 mM, $B_0(0)$ increases by only a factor of $\sim$7, i.e., a linear rather than an exponential increase. For (ii), however, the scaling relation $B_0(\vec{r})/B_\infty = (c(\vec{r})/c_\infty)^{g'}$ appears to be more reasonable since $B_0(\vec{r})$ does not blow up exponentially with $c(\vec{r})$. However, we were unable to collapse $B_0(\vec{r})$ with $c(\vec{r})$ using the above scaling relationship over the entire range of r, suggesting that the master equation in its current form is incomplete.

5.3 DISCUSSIONS

The main point of this chapter is the demonstration that a microorganism can modify its motility pattern at microscopic scales to significantly reduce its diffusivity without compromising its drift velocity in a chemical gradient. This counter-intuitive effect, which violates the so-called fluctuation-dissipation theorem, can be exploited by microorganisms to improve their fitness in an environment. In the present study, it shows that by employing the 3-step motility pattern the marine bacterium can sequester nutrients more efficiently than its 2-step counterpart. We note that *V. alginolyticus* can swarm around the nutrient source so tightly

that the diameter of the profile is only about thrice of the free swimming distance $v\tau_{CCW} \simeq 23$ μm, which barely meets the long-time limit by which the master equation is derived. Our study also shows that the outstanding chemotactic ability of the marine bacterium is not due to its high sensitivity to chemicals, but rather owes to attributes such as (i) a high swimming speed v, (ii) a relatively large intrinsic switching rate k_0, and most importantly (iii) the 3-step motility pattern. In order to take the full advantage of these attributes, the bacterial chemotaxis network processes chemical information rapidly, as observed in Chapter 4. In the model for *V. alginolyticus*, for simplicity it was assumed that k_0 and Δk to be the same for both forward and backward swimming intervals. However, as shown in Chapter 3 and 4, the flagellar motor responds to CheY-P differently depending on the motor state and $\Delta k_f > \Delta k_b$. This asymmetry is speculated to be related to the asymmetry between two swimming intervals and may further improve the efficiency of its chemotaxis. Studies on the effect of these fine tunings on the chemotaxis system and how they are implemented on a molecular level can reveal more novel properties in the chemotaxis system.

A concise and reliable macroscopic equation that relates bacterial concentration fluctuations $B(\vec{r}, t)$ to local chemical concentration fluctuations $c(\vec{r}, t)$ is important for modeling and understanding how bacteria interact with their environment. This can provide convenient and quantitative means to characterize chemical distributions in different microbial communities. However, this goal is only partially realized. Evidently for an accurate description of the bacterial distribution given the chemical distribution more study is needed.

6.0 MATERIALS AND METHODS

6.1 BACTERIA STRAINS AND GROWTH CONDITIONS

The bacterial strains used in the experiment are listed in Table 5 and 6.

For experiments in Chapter 2, *V. alginolyticus* was grown following the protocols in Ref. [68]. Strains YM4 (with or without the pZA3R-YFP plasmid), VIO5, and 138-2 were grown at 30 ^{o}C with vigorous shaking at 200 revolutions per minute (rpm) overnight in VC medium (0.5% polypeptone, 0.5% yeast extract, 0.4% K_2HPO_4, 3% NaCl, 0.2% glucose, supplemented with 2.5 μg/ml chloramphenicol when needed) [41]. The overnight was diluted 1:100 into VPG medium (1% g polypeptone, 0.4% K_2HPO_4, 3% NaCl, 0.5% glycerol, supplemented with 2.5 μg/mL chloramphenicol when needed) and grown to late-exponential phase. Cells were spun down and resuspended in TMN motility medium (50 mM Tris-HCl (pH 7.5), 5mM $MgCl_2$, 5 mM glucose, 30 mM NaCl, 270 mM KCl) and incubated for at least half an hour at 30 ^{o}C, while being shaken at 200 rpm. For experiments in Chapter 3 and 4, were grown at 30 ^{o}C with vigorous shaking at 200 rpm overnight in LBS medium (1% polypeptone, 0.5% yeast extract, 3% NaCl, supplemented with 2.5 μg/ml chloramphenicol when needed). The saturated overnight culture was diluted 1:100 into minimum medium [74](0.3 M NaCl, 10 mM KCl, 2 mM K_2HPO_4, 0.01 mM $FeSO_4$, 15 mM $(NH_4)_2SO_4$, 5 mM $MgSO_4$, 1% glycerol and 50 mM Tris-HCl (pH 7.5), supplemented with 1 μg/ml chloramphenicol when needed) and grown to an O.D. of 0.2 (the O.D. is always measured at 600 nm). 1.5 ml culture were harvested and spun down at 2000 $\times$ g for 3 minutes. After removing the supernatant, 1 ml TMN was used to resuspend the culture followed by a 5-minute centrifuging at 500 $\times$ g. 300-400 μL supernatant was then carefully diluted into 2 ml TMN and shaken at 200 rpm at room temperature.

V. alginolyticus Strain	Genotype/Phenotype	Parent strain	Reference
138-2	Wild Type	NA	([41])
VIO5	Pof$^+$ Laf$^-$	138-2	([36])
YM4	Pof$^+$ Laf$^-$	138-2	([36])
NMB102	CW motor	138-2	([37])
YM4-Δ*cheY*	Δ*cheY*	YM4	This work
YM4-Δ*cheZ*	Δ*cheZ*	YM4	This work
YM4-Δ*cheA*	Δ*cheA*	YM4	This work
YM4-Δ*cheR*	Δ*cheR*	YM4	This work
YM4-Δ*cheB*	Δ*cheB*	YM4	This work
YM4-Δ*cheV*	Δ*cheV*	YM4	This work

Table 5: *V. alginolyticus* strains and references.

E. coli RP437 with pZA3R-YFP plasmid were grown overnight in M9 medium supplemented with 30 μg/ml chloramphenicol at 30 ^{o}C to reach an O.D of 0.2. The cells were then carefully washed and resuspended with motility buffer (10 mM potassium phosphate, 0.1 mM EDTA, 10 mM sodium-L-lactate, 1 μM L-methionine, pH 7.0). *P. haloplanktis* were grown overnight in 1% tryptic soy broth at room temperature shaking at 200 rpm. The culture was diluted 1:200 into filtered sea water and starved at room temperature for 5 hours before observation [70].

Organism	Strain	Genotype/Phenotype	Reference
E. coli	RP437	Wild Type	[57]
Pseudoalteromonas haloplanktis	ATCC700530	Wild Type	ATCC

Table 6: Other strains and references.

6.2 PHASE CONTRAST MICROSCOPY FOR TRACKING EXPERIMENTS

To obtain the bacterial swimming trajectories, different sample chambers were used. To observe the bacterial motion far from the surface, a deep sample chamber was made by sandwiching a 1.2 mm thick silicon gasket between two cover slips. The position of the objective was adjusted so that the focus was ˜600 μm from both surfaces. To track cells for a longer time, a shallow counting chamber with a 10-μm gap(Hawksley, Z3BC1B) was used so the cell stays in the focal plane. The chamber was filled with bacteria culture and observed under an inverted microscope (Nikon, TE-300) with a 20× objective, which has a depth of field ˜6 μm. Videos were taken at 30 frames per second (fps) by a CCD camera (Hamamatsu, EM-CCD C9100) and then analyzed by ImageJ (National Institutes of Health) and Matlab (The Mathworks, Inc.).

Since *V. alginolyticus* swim at a high speed, with an average swimming speed ∼45 μm/s, their positions can be accurately determined by video microscopy operating at 30 fps. For instance, with a 20× objective, the bacterium moves ˜1.5 μm between two frames, corresponding to a displacement of 2 pixels on the CCD camera and can be readily resolved. However, due to fluctuations in the bacterial swimming speed, particularly during the transitions from forward to backward or vice versa, the spatial and temporal resolutions are somewhat compromised, resulting in the uncertainty of Δ_f and Δ_b to be ˜0.07 s or 2 frames.

To obtain$P(\Delta_f)$ and $P(\Delta_b)$ for individual cells, the observation chamber was placed on a motorized stage (SD instrument, MC2000 controller, 200 Cri motorized linear stage) controlled by a joystick to keep the cell in the field of view. Because of the shallow chamber and low magnification objective, we were able to track a single *V. alginolyticus* cell for 10 minutes. The tracking videos were analyzed using ImageJ (National Institution of Health) and Matlab (The Mathworks, Inc.) to extract pairs of (Δ_f, Δ_b). Using this method, the resolution limit ofΔ_f and Δ_b are ˜0.067 s, which is two frames.

6.3 DETERMINING SWITCHING RATES UNDER DIFFERENT [YP]

To study the motor behavior under different CheY concentration, YM4-Δ*cheY* harboring a plasmid with *cheY* gene under the control of *lac* were grown at 30 ^{o}C with vigorous shaking at 200 rpm overnight in LBS medium supplemented with 2.5 μg/ml chloramphenicol. The saturated overnight culture was diluted 1:100 into minimum medium [74] supplemented with 1 μg/ml chloramphenicol and grown at 30 ^{o}C with vigorous shaking at 200 rpm to an O.D. of 0.1. Different amounts of IPTG ranging from 0-3 μM were added to the culture and the culture is grown to an O.D. of 0.2. 3.5 mL culture was then spun down at 1500 $\times$ g for 15 minutes. After the removal of supernatant, the culture was resuspended in 3 mL TMN and shaken at room temperature at 200 rpm for another 3 hours. The culture was then adjusted to an O.D. of 0.15 before its fluorescence was measured in a fluorometer (Bio-rad, VersaFluor) with an 480±10 nm excitation filter and an 510 $\pm$ 5 nm emission filter.

To calculate k_f and k_b for a randomly picked individual cell, the cell is tracked for 5 forward and backward swimming intervals or as long as it stays in the field of view. At medium or high induction levels, Δ_f and Δ_b are usually around a couple of seconds. The cell is tracked to obtain 5 Δ_f and their average is taken to be $1/k_f$. k_b is obtained in the same way. At a low induction level, however, some cells swim forward for tens of seconds, and we cannot tell when the the forward interval starts or ends because it gets out of the field of view, resulting in a partial forward interval $\Delta_{f,partial}$. If such partial intervals are dropped and only those complete ones are kept, k_f would be over-estimated. To incorporate these partial intervals into the statistics, we used the following simple criteria: for a certain cell, if its partial forward interval is longer than the longest complete forward interval found in the track of this cell, this partial forward interval is counted as a full forward interval and used for calculating k_f. As a result, k_f at low induction level is slightly over-estimated. To completely remove this bias, a better technique that allows long observation of a cell needs to be developed.

6.4 FLUORESCENCE MICROSCOPY FOR SWARMING EXPERIMENTS

For fluorescence microscopy to observe the position of the flagellum, cells were labeled with Nano Orange dye (Invitrogen) and observed using a 100× oil-immersion objective. The fluorescence images were taken close to the surface for a better image quality. The fast-video images were acquired in a phase contrast mode using the 100× oil-immersion objective and a Phantom V digital camera. The focal plane was set at 100 μm above the cover slip.

In the swarming experiments using fluorescent bacteria, the bacterial density $B(r,t)$ is determined from the fluorescence intensity $I(r,t)$ of RP437-YFP or YM4-YFP. The fluorescent microscopy was performed on an inverted Nikon (TE-300) microscope with a 10× objective. The fluorescent bacteria were imaged by a Hamamatsu camera (EM-CCD C9100) and analyzed by ImageJ (National Institutes of Health) and Matlab (The MathWorks). At the beginning of the experiment, the bacteria were homogenized by stirring, and subsequent aggregation behaviors were measured at different time intervals using a video camera. To minimize possible photo-damage due to intense excitation light (λ = 488 nm), a computer-controlled shutter was introduced between the arc lamp and the collimator of the epi-fluorescence attachment of the microscope. The shutter was interfaced via a data acquisition board (National Instruments, PCI-6601) and Labview (National Instruments). The bacteria were exposed to the excitation light for 0.1-0.2 s every few seconds so that snapshots of the bacterial profile were acquired.

Using the images at the end of the swarming experiment, the swarm center (x_0, y_0) was determined: $(x_0, y_0) = \sum(x_i I_i, y_i I_i)/\sum I_i$ where x_i and y_i are the coordinates of pixels, and $I_i(x_i, y_i)$ is the background subtracted intensity and $I_i(x_i, y_i) \propto B(x_i, y_i)$. To reduce the noise in the intensity, the time-dependent $I_i(x_i, y_i, t)$ was circularly averaged in a circular band, r to $r + \Delta r$, where $\Delta r = 15$ μm to obtain $I(r,t)$ or $B(r,t)$.

In our experiment, the serine-filled micro-pipette was placed 200-300 μm above the bottom surface of a chamber. Within this hundred-micron region, the injected serine forms a plume with a cylindrical symmetry. The axially symmetric distribution of serine allows calculations to be simplified. We estimated the drifting velocity v_d using the bacterium

conservation equation,

$$\frac{\partial P(\overrightarrow{r},t)}{\partial t} = -\overrightarrow{\nabla} \cdot \overrightarrow{J}(\overrightarrow{r},t). \tag{6.1}$$

Because of the cylindrical symmetry, we have $P(\overrightarrow{r},t) = P(r,t)$ and $\overrightarrow{J}(\overrightarrow{r},t) = J(r,t)\hat{r}$. The original 3D problem is thus reduces to a 2D problem. Integrating both sides of Eq. 6.1 over a disk A of radius R, we found,

$$\frac{\partial \int_A P(r,t)dA}{\partial t} = -\int_A \overrightarrow{\nabla} \cdot \overrightarrow{J}(\overrightarrow{r},t)dA = -J(R,t) \cdot 2\pi R. \tag{6.2}$$

Since the flux is composed of a drifting and a diffusion term, $J(R,t) = -D\frac{\partial P(r,t)}{\partial r}|_{r=R} + v_d P(R,t)$, we can write v_d as,

$$v_d = -(\frac{\partial \int_A P(r,t)dA}{\partial t} - 2\pi RD\frac{\partial P(r,t)}{\partial r}|_{r=R})/2\pi RP(R,t). \tag{6.3}$$

To calculate v_d for *E. coli* and *V. alginolyticus* from the experiment, $I(r,t)$ or $B(r,t)$ calculated above is used for$P(r,t)$.

Disk sizes $R = 30$ μm and $R = 150$ μm were chosen for *V. alginolyticus* and *E. coli* respectively, and were used to calculate the quantities in Eq. 6.3:

$$\int_A P(r,t)dA = \sum_{r=0}^{r=R-\Delta r} P(r,t)\pi[(r+\Delta r)^2 - r^2], \tag{6.4}$$

$$\partial P(r,t)/\partial r|_{r=R} = (P(R+\Delta r) - P(R-\Delta r))/2\Delta r. \tag{6.5}$$

To improve the accuracy of v_d measurement, four different times t_1, t_2, t_3, t_4 were chosen to compute $\int_A P(r,t_i)dA$ and $\Delta P(r,t_i)/\Delta r|_{r=R}$. From these, three values of v_d were then calculated

$$v_d^i = -(\frac{\int_A P(r,t_{i+1})dA - \int_A P(r,t_i)dA}{t_{i+1}-t_i} - 2\pi RD\frac{\partial P(r,t_i)}{\partial r}|_{r=R})/2\pi RP(R,t_i) \tag{6.6}$$

and averaged. For *E. coli*, $t_i = 110 + 60i$ s and for *V. alginolyticus*, $t_i = 36 + 20i$ with $i = 1,2,3,4$. The above procedure yields the average value $v_d = 1.6$ μm/s for *E. coli* and $v_d = 2.4$ μm/s for *V. alginolyticus*.

6.5 CREATION OF SERINE CONCENTRATION GRADIENT

For the tracking and the swarming measurements in a chemical gradient, we used an open chamber, which has a diameter of ˜2 cm and allows a micropipette to be inserted from top. The chamber was mounted on the inverted microscope for observation. The micropipette was prepared by a glass pipette puller (Narishige, PP-830), then filled with serine solution at different concentrations to a height that balanced the capillary effect. This tip was inserted into a micropipette adaptor (World Precision Instrument, 5430-15), and could be precisely positioned by a motorized 3D micromanipulator (SD instruments, MX7630L). The tip of the micropipette was adjusted to ˜200-300 μm above the surface of the open observation chamber. Pressurized by a 22-mm-high water column, the serine solution was injected slowly at a rate of 6×10^{-12} Liter/s, creating a gradient in its neighborhood. Using a fluorescein dye, we found that this injection scheme allowed a steady-state concentration profile to be established rapidly, within 0.1 s, and the tail of the serine profile decays slowly and is approximately linear [5].

6.6 CREATION OF A STEP INCREASE IN SERINE CONCENTRATION

To probe the response of *V. alginolyticus* to well-defined positive stimuli, we used a chemical called NPE-caged-serine, which is synthesized by attaching a photosensitive group to serine [39]. Because of this group, the NPE-caged-serine cannot be recognized by the bacteria until it gets uncaged by near-UV light of wavelength 340-380 nm. The NPE-caged-serine used in the experiments was synthesized by Dr. Chunliang Lu and Professor Paul Floreancig from the chemistry department of University of Pittsburgh. In our experiments, cells were mixed with motility buffer containing NPE-caged-serine and put into a narrow chamber with a 10 μm depth. The 340-380 nm light was introduced from the epifluorescence microscopy attachment on the Nikon TE-300 microscope through a 20×objective and illuminated a circular area of ˜ 2.5 mm diameter. A shutter was placed in the light path and controlled by computer, as shown in Figure 35. In a typical experiment, we recorded the swimming of

the bacteria for ˜4 seconds before a 0.1 s 340-380 nm near-UV pulse was applied. The video continued through the next 6 seconds. Since the diffusion constant of serine is ˜900 $\mu m^2/s$, and the imaging area is ˜400 μm×400 μm at the center of the illuminated area, we consider the serine concentration in our imaging area to be constant during the 6 seconds after the near-UV pulse. The bacteria trajectories were analyzed as described above to identify motor reversal times and calculate $k_f(t)$ and $k_b(t)$.

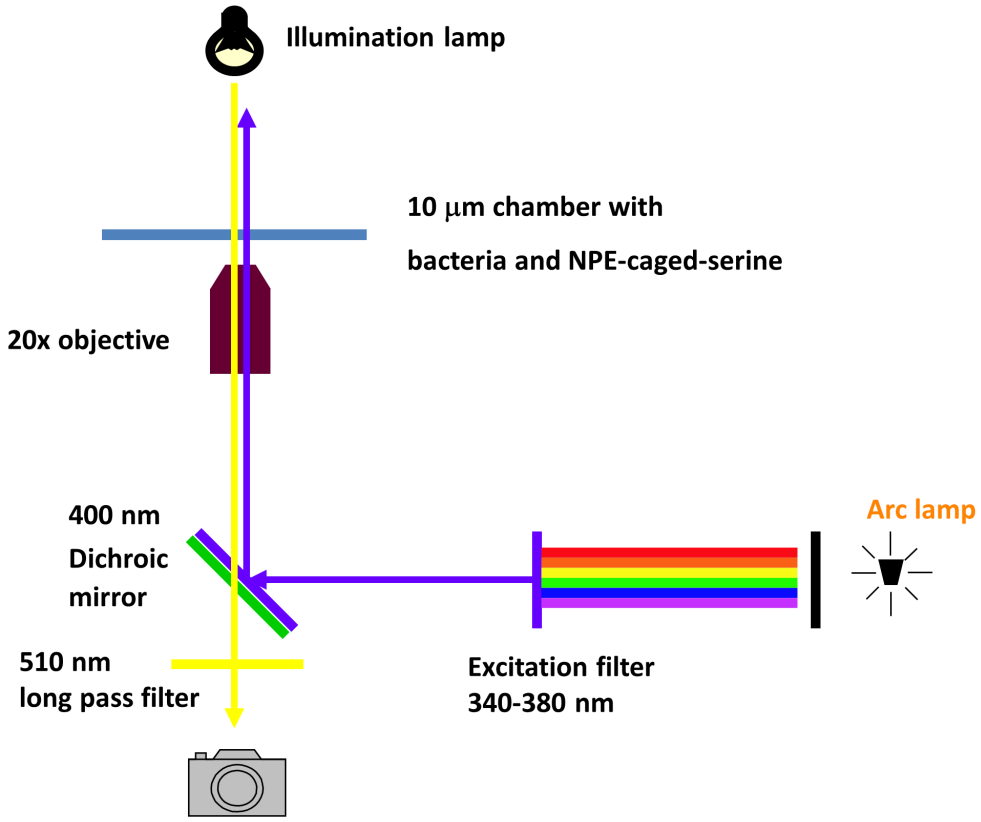

Figure 35: Set up of the experiment in which a certain amount of serine is released in $\sim$ 100 ms.

NPE-caged-HPTS is used to calibrate the amount of serine released in each experiment [33]. HPTS is a fluorescent dye and when it is in the caged form, NPE-caged-HPTS, it is not fluorescent. When NPE-caged-HPTS was exposed to near-UV light, free HPTS is released and can be excited by light with wavelength 340-380 nm and emit fluorescence peaked around 520 nm [33]. To measure the uncaging efficiency of NPE-caged-HPTS, 0.2

μL of 20 μM NPE-caged-HPTS in TMN was mixed with heavy mineral oil by pipetting before introduced into the chamber with a 10 μm depth. A droplet of the NPE-caged-HPTS solution with a diameter of 100-300 μm was chosen under the microscope. Since this droplet is trapped in the mineral oil, it does not evaporate of move over the period of experiment. A video was then taken at 1 frame per second for 15 minutes while the sample is continuously irradiated by arc lamp light filtered through a 340-380 nm bandpass filter with the same setup as described above and in Figure 35, except that the light intensity is reduced by half. The video started at the same time when the droplet started to be irradiated. The 340-380 nm light uncages the NPE-caged-HPTS as well as excites free HPTS. The fluorescence of HPTS was passed through a 510 nm long pass filter and detected by a CCD camera (EM-CCD C9100). The average fluorescence of a region inside the droplet I_{HPTS} is then analyzed using Matlab. The concentration of HTPS c_{free} inside the droplet uncaged from NPE-caged-HPTS with an initial concentration of c_{caged} can be described as

$$\frac{dc_{free}}{dt} = k(c_{caged} - c_{free}) \tag{6.7}$$

with the initial condition $c_{free}(t = 0) = 0$. Thus $c_{free} = c_{caged}(1 - \exp(-kt))$ and $I_{HPTS} \propto c_{free}$. Since HPTS is rather photostable, a photobleaching term is not included in Eq. 6.7. Figure 36 shows the normalized fluorescence intensity $I_N = I_{HPTS}/I_{HPTS}^{max}$ as a function of time. As shown, I_N increases rapidly from $t = 0$ and reaches 1 around $t = 500$ s when the NPE-caged-HPTS is depleted. At $t > 500$ s, I_{HPTS} drops due to photobleaching. However, it drops by about 2% at $t = 900$ s. It is thus reasonable to neglect photobleaching in our analysis. By fitting I_N to $I_N = 1 - \exp(-kt)$, it was found that $k = 1.07 \times 10^{-2}$/s. The above procedure is repeated twice and $k = 1.00 \times 10^{-2}$ and $k = 9.92 \times 10^{-3}$ were obtained. Thus the uncaging rate of the NPE-caged-HPTS is k =0.01/s

The uncaging efficiency is proportional to the product of the extinction coefficient of the caged chemical and quantum yield. The extinction coefficient is a measurement of how strongly a chemical species absorbs light at a given wavelength and has the dimension of $M^{-1}{\cdot}m^{-1}$. It is mainly determined by the cage group. In our case since both serine and HPTS are caged by the NPE group, their extinction coefficients are considered to be the same. The quantum yield is the probability of uncaging after absorption of a photon. According to Ref.

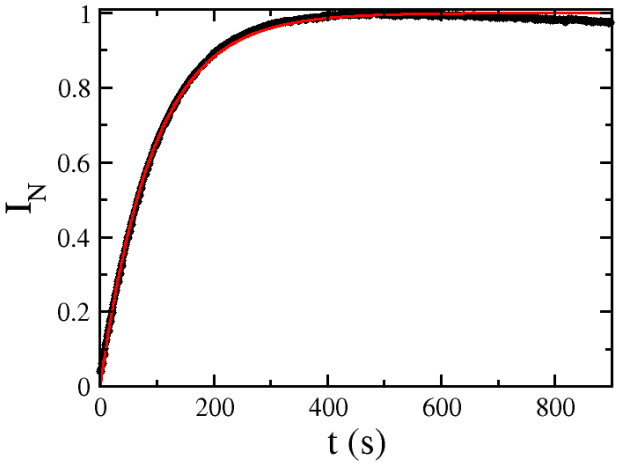

Figure 36: The normalized fluorescence intensity $I_N = I_{HPTS}/I_{HPTS}^{max}$ as a function of time t. The black dots are the experimental value and the red line is the fitting result to $I_N = 1 - \exp(-kt)$ where $k = 1.07 \times 10^{-2}$/s.

[33], the quantum yield of the NPE-caged-HPTS is $20\% \pm 4\%$ of that of the NPE-caged-ATP, and the quantum yield of the NPE-caged-ATP is about the same as that of NPE-caged-serine [39]. Considering that the light intensity used in the calibration is half of that used in the experiment described above, when the sample is exposed to 340-380 nm light for 0.1 second, $1\% \pm 0.2\%$ serine is released into the medium.

6.7 NUMERICAL SOLUTION TO MASTER EQUATIONS

Discretized versions of of the master equations for the 2-step and 3-step swimmer are developed below, and they are used for the numerical calculations. In the continuum limit these equations are consistent with Eqs. 5.3-5.4 and Eqs. 5.10-5.13. All of our computations were done with Matlab (The MathWorks).

We divided space into segments of equal size Δx located at $\{x_i\}$, and divided time into

equal intervals Δt at $\{t_i\}$. For the 2-step case, the conservation of probability demands,

$$\begin{aligned} P(\hat{x}, x_i, t_i) =& P(\hat{x}, x_{i-1}, t_{i-1}) - \frac{1}{2}\left(k_0 - \Delta k(x_i)\right)\Delta t P(\hat{x}, x_{i-1}, t_{i-1}) \\ &+ \frac{1}{2}\left(k_0 + \Delta k(x_i)\right)\Delta t P(-\hat{x}, x_{i+1}, t_{i-1}) \end{aligned} , \tag{6.8}$$

$$\begin{aligned} P(-\hat{x}, x_i, t_i) =& P(-\hat{x}, x_{i+1}, t_{i-1}) - \frac{1}{2}\left(k_0 + \Delta k(x_i)\right)\Delta t P(-\hat{x}, x_{i+1}, t_{i-1}) \\ &+ \frac{1}{2}\left(k_0 - \Delta k(x_i)\right)\Delta t P(\hat{x}, x_{i-1}, t_{i-1}) \end{aligned} . \tag{6.9}$$

Physically, $P(\hat{x}, x_i, t_i)$ (or $P(-\hat{x}, x_i, t_i)$) is the probability of finding a cell swimming in $\hat{x}$ (or $-\hat{x}$) direction at x_i and t_i. If a cell reaches x_i at time t_i, it must be either at x_{i-1} swimming along the $\hat{x}$ direction or at x_{i+1} swimming along the $-\hat{x}$ direction at time t_{i-1}. Among cells arriving from x_{i-1}, which is $P(\hat{x}, x_{i-1}, t_{i-1})$, $1 - (k_0 - \Delta k(x_i))\Delta t$ of them will continue in the current swimming direction $\hat{x}$, and $(k_0 - \Delta k(x_i))\Delta t$ of them will randomize their swimming direction. Upon direction randomization, 50% of the this sub-population swims in $\hat{x}$ and the other 50% in $-\hat{x}$ direction. Together, $1 - \frac{1}{2}(k_0 - \Delta k(x_i))\Delta t$ of $P(\hat{x}, x_{i-1}, t_{i-1})$ contributes to $P(\hat{x}, x_i, t_i)$, which corresponds to the first two terms in Eq. 6.8. Likewise, the same argument shows that $\frac{1}{2}(k_0 + \Delta k(x_i))\Delta t$ of $P(-\hat{x}, x_{i+1}, t_{i-1})$ also contributes to $P(\hat{x}, x_i, t_i)$, which corresponds to the last term in Eq. 6.8. Similar conservation equations can be derived for the sub-population $P(-\hat{x}, x_i, t_i)$, yielding Eq. 6.9. Expanding terms in the above equations around x_i and t_i, we recovered the continuous master equations, Eqs. 5.3-5.4, in the limits $\Delta x \to 0$, $\Delta t \to 0$, and $\Delta x/\Delta t \to v$.

The derivation for the 3-step case is more tedious, but the idea is the same. The four equations are given by,

$$\begin{aligned} P_{CCW}(\hat{x}, x_i, t_i) = &\left[1 - \left(k_0 - \Delta k(x_i)\right)\Delta t\right] P_{CCW}(\hat{x}, x_{i-1}, t_{i-1}) \\ &+ \frac{1}{2}\left(k_0 - \Delta k(x_i)\right)\Delta t P_{CW}(\hat{x}, x_{i-1}, t_{i-1}) \\ &+ \frac{1}{2}\left(k_0 + \Delta k(x_i)\right)\Delta t P_{CW}(-\hat{x}, x_{i+1}, t_{i-1}) \end{aligned} , \tag{6.10}$$

$$\begin{aligned} P_{CCW}(-\hat{x}, x_i, t_i) = &\left[1 - \left(k_0 + \Delta k(x_i)\right)\Delta t\right] P_{CCW}(-\hat{x}, x_{i+1}, t_{i-1}) \\ &+ \frac{1}{2}\left(k_0 + \Delta k(x_i)\right)\Delta t P_{CW}(-\hat{x}, x_{i+1}, t_{i-1}), \\ &+ \frac{1}{2}\left(k_0 - \Delta k(x_i)\right)\Delta t P_{CW}(\hat{x}, x_{i-1}, t_{i-1}) \end{aligned} \tag{6.11}$$

$$P_{CW}(\hat{x}, x_i, t_i) = [1 - (k_0 - \Delta k(x_i))\,\Delta t]P_{CW}(\hat{x}, x_{i-1}, t_{i-1}) + (k_0 + \Delta k(x_i))\,\Delta t P_{CCW}(-\hat{x}, x_{i+1}, t_{i-1}) \quad (6.12)$$

$$P_{CW}(-\hat{x}, x_i, t_i) = [1 - (k_0 + \Delta k(x_i))\,\Delta t]P_{CW}(-\hat{x}, x_{i+1}, t_{i-1}) + (k_0 - \Delta k(x_i))\,\Delta t P_{CCW}(\hat{x}, x_{i-1}, t_{i-1}). \quad (6.13)$$

In the calculation, we assigned $\Delta x = 0.1$, $2L = 200$ or $2000\Delta x$, $\Delta t = 1$, and $v = \Delta x/\Delta t = 0.1$. Using the computational step Δt as the basic time unit, we defined the transition rates, $k_0 = 0.1$ and $\Delta k = 0.01$, giving the drift velocity $v_d = v\Delta k/k_0 = 10^{-2}$. The equations are solved using the reflective boundary conditions at $x = \pm L$. To generate the numerical solutions in Figure 30, Eqs. 6.8-6.9 and Eqs. 6.10-6.13 were solved using the initial conditions $P(\pm\hat{x}, x_i, 0) = \exp(-x_i^2/2\sigma^2)/2\sqrt{2\pi\sigma^2}$ and $P_{CCW}(\pm\hat{x}, x_i, 0) = P_{CW}(\pm\hat{x}, x_i, 0) = \exp(-x_i^2/2\sigma^2)/4\sqrt{2\pi\sigma^2}$, respectively. Here, $\sigma = 5\Delta x$ was used. To obtain the numerical solutions in Figure 31, the initial conditions $P(\pm\hat{x}, x_i, 0) = 1/(4L/\Delta x)$ and $P_{CCW}(\pm\hat{x}, x_i, 0) = P_{CW}(\pm\hat{x}, x_i, 0) = 1/(8L/\Delta x)$ were used for the 2-step and 3-step swimmers, respectively.

BIBLIOGRAPHY

[1] Julius Adler. Chemotaxis in escherichia coli. *Cold Spring Harbor Symp. Quant. Biol.*, 30:289–292, 1965.

[2] Julius Adler. Chemoreceptors in bacteria. *Science*, 166:1588–1597, 1969.

[3] Julius Adler. A method for measuring chemotaxis and use of the method to determine optimum conditions for chemotaxis by escherichia coli. *J Gen Microbiol*, 74:77–91, 1973.

[4] Roger P. Alexander, Andrew C. Lowenthal, Rasika M. Harshey, and Karen M. Ottemann. Chev: Chew-like coupling proteins at the core of the chemotaxis signaling network. *Trends in Microbiology*, 18:494–503, 2010.

[5] Tuba Altindal, Suddhashil Chattopadhyay, and Xiao-Lun Wu. Bacterial chemotaxis in an optical trap. *PLoS ONE*, 6:e18231, 2011.

[6] Tuba Altindal, Li Xie, and Xiao-Lun Wu. Implications of three-step swimming patterns in bacterial chemotaxis. *Biophysical Journal*, 100(1):32–41, 2011.

[7] J.P. Armitage and R.M. Macnab. Unidirectional, intermittent rotation of the flagellum of rhodobacter sphaeroides. *J Bacteriol*, 169:514–518, 1987.

[8] G.M. Barbara and J.G. Mitchell. Bacterial tracking of motile algae. *FEMS Microbiol Ecol*, 44:79–87, 2003.

[9] N. Barkai and S. Leibler. Robustness in simple biochemical networks. *Nature*, 387:913–917, 1997.

[10] B.K. Batchelor. Small-scale variation of convected quantities like temperature in turbulent fluid, part1. general discussion and the case of small conductivity. *J. Fluid Mech.*, 5:113–133, 1959.

[11] H.C. Berg. *Random Walks in Biology.* Princeton University Press, Princeton, 1993.

[12] H.C. Berg. *E. coli in Motion.* Springer-Verlag, NY, 2004.

[13] H.C. Berg and Robert A. Anderson. Bacteria swim by rotating their flagellar filaments. *Nature*, 245:380–382, 1973.

[14] H.C. Berg and Douglas A. Brown. Chemotaxis in escherichia coli analysed by three-dimensional tracking. *Nature*, 239:500–504, 1972.

[15] Steven M. Block, Jeffrey E. Segall, and Howard C. Berg. Impulse responses in bacterial chemotaxis. *Cell*, 31(1):215–226, 1982.

[16] Dennis Bray, Matthew D. Levin, and Carl J. Morton-Firth. Receptor clustering as a cellular mechanism to control sensitivity. *Nature*, 393:85–88, 1998.

[17] Anat Bren and Michael Eisenbach. How signals are heard during bacterial chemotaxis: Protein-protein interactions in sensory signal propagation. *J Bacteriol*, 182:6865–6873, 2000.

[18] Antonio Celani and Massimo Vergassola. Bacterial strategies for chemotaxis response. *Proc. Natl. Acad. Sci. USA*, 108:1391–1396, 2009.

[19] S. Chattopadhyay and X.L Wu. The effect of long-range hydrodynamic interaction on the swimming of a single bacterium. *Biophys J*, 96:2023–2028, 2009.

[20] P. Cluzel, M. Surette, and S. Leibler. An ultrasensitive bacterial motor revealed by monitoring signaling proteins in single cells. *Science*, 287:1652–1655, 2000.

[21] D.A. Darling. *The first passage problem for a continous Markoff process*. Rand Corporation, Pennsylvania, 1953.

[22] P.G. de Gennes. Chemotaxis: the role of internal delays. *Eur. Biophys. J.*, 33:691–693, 2004.

[23] M. Demir and H. Salman. Bacterial thermotaxis by speed modulation. *Biophys J*, 103:1683–1690, 2012.

[24] T. A. J. Duke, N. Le. Novere, and D. Bray. Conformational spread in a ring of proteins: A stochastic approach to allostery. *J. Mol. Biol.*, 308:541–553, 2001.

[25] Michael Eisenbach. Control of bacterial chemotaxis. *Molecular Microbiology*, 20(5):903–910, 1996.

[26] Michael Eisenbach and Julius Adler. Bacterial cell envelopes with functional flagella. *J Biol Chem*, 256:8807–8814, 1981.

[27] Peter Engstrom and Gerald L. Hazelbauer. Methyl-accepting chemotaxis proteins are distributed in the membrane independently from basal ends of bacterial flagella. *Biochimica et Biophysica Acta (BBA) - Biomembranes*, 686(1):19 – 26, 1982.

[28] Radek Erban and Hans G. Othmer. From individual to collective behavior in bacterial chemotaxis. *SIAM J. Appl. Math*, 65:361–391, 2006.

[29] Jason E. Gestwicki, Allison C. Lamanna, Rasika M. Harshey, Linda L. McCarter, Laura L. Kiessling, and Julius Adler. Evolutionary conservation of methyl-accepting chemotaxis protein location in bacteria andarchaea. *Journal of Bacteriology*, 182(22):6499–6502, 2000.

[30] R.J. Glauber. *Quantum Optics and Electronics (eds C. DeWett, A. Blandin, and C. Cohen-Tannoudji)*. Gordon and Breach, New York, 1965.

[31] T. Goto, S.Y. Masuda, T. Kazumasa, and Y. Takano. Comparison between observation and boundary element analysis of bacterium swimming motion. *JSME Intl J, Ser C*, 44:958–963, 2001.

[32] Gerald L. Hazelbauer and Julius Adler. Role of the galactose binding protein in chemotaxis of escherichia coli toward galactose. *nature new biology*, 230:101–104, 1971.

[33] Ravi Jasuja, Jinsoo Keyoung, Gordon P. Reid, David R. Trentham, and Shahid Khan. Chemotactic responses of escherichia coli to small jumps of photoreleased l-aspartate. *Biophysical Journal*, 76(3):1706–1719, 1999.

[34] Yevgeniy V. Kalinin, Lili Jiang, Yuhai Tu, and Mingming Wu. Logarithmic sensing in escherichia coli bacterial chemotaxis. *Biophys J*, 96:2439–2448, 2009.

[35] S. Kalir, J. McClure, K. Pabbaraju, C. Southward, M. Ronen, S. Leibler, M.G. Surette, and U. Alon. Ordering genes in a flagella pathway by analysis of expression kinetics from living bacteria. *Science*, 292:2080–2083, 2001.

[36] I. Kawagishi, Y. Maekawa, T. Atsumi, M. Homma, and Y. Imae. Isolation of the polar and lateral flagellum-defective mutants in vibrio alginolyticus and identification of their flagellar driving energy sources. *J Bacteriol*, 177:5158–5160, 1995.

[37] Ikuro Kawagishi, Miho Imagawa, Yasuo Imae, Linda McCarter, and Michio Homma. The sodium-driven polar flagellar motor of marine vibrio as the mechanosensor that regulates lateral flagellar expression. *Molecular Microbiology*, 20(4):693–699, 1996.

[38] Evelyn F. Keller and Lee A. Segel. Model for chemotaxis. *J Theor Biol*, 30:225–234, 1971.

[39] Shahid Khan, Fred Castellano, John L. Spudich, James A. McCray, Roger S. Goody, Gordon P. Reid, and David R. Trentham. Excitatory signaling in bacteria probed by caged chemoeffectors. *Biophys J*, 65:2368–2382, 1993.

[40] Masaru Kojima, Rumi Kubo, Toshiharu Yakushi, Michio Homma, and Ikuro Kawagishi. The bidirectional polar and unidirectional lateral flagellar motors of vibrio alginolyticus are controlled by a single chey species. *Mol Microbiol*, 64:57–67, 2007.

[41] S. Kojima, T. Atsumi, K. Muramoto, S. Kudo, I. Kawagishi, and M. Homma. Vibrio alginolyticus mutants resistant to phenamil, a specific inhibitor of the sodium-driven flagellar motor. *J Mol Biol*, 265:310–318, 1997.

[42] S.C. Kuo and D.E. Koshland Jr. Multiple kinetic states for the flagellar motor switch. *J Bacteriol*, 171:6279–6287, 1989.

[43] Steven H. Larsen, Robert W. Reader, Edward N. Kort, Wung-Wai Tso, and Julius Adler. Change in direction of flagellar rotation is the basis of the chemotactic response in escherichia coli. *Nature*, 249:74–77, 1974.

[44] G.L. Li, L.K. Tam, and J.X. Tang. Amplified effect of brownian motion in bacterial near-surface swimming. *Proc Natl Acad Sci USA*, 105:18355–18359, 2008.

[45] J.T. Locsei and T.J. Pedley. Bacterial tracking of motile algae assisted by algal cell's vorticity field. *Micob Ecol*, 58:63–74, 2009.

[46] R.H. Luchsinger, B. Bergersen, and J.G. Mitchell. Bacterial swimming strategies and turbulence. *Biophys. J.*, 77:2377–2386, 1999.

[47] R.M. Macnab. Bacterial flagella rotating in bundles: a study in helical geometry. *Proc Natl Acad Sci USA*, 74:221–225, 1977.

[48] R.M. Macnab. How bacteria assemble flagella. *Annu. Rev. Microbiol.*, 57:77–100, 2003.

[49] Robert M. Macnab and D. E. Koshland. The gradient-sensing mechanism in bacterial chemotaxis. *Proc Natl Acad Sci USA*, 69:2509–2512, 1972.

[50] Y Magariyama, S Sugiyama, K Muramoto, I Kawagishi, Y Imae, and S Kudo. Simultaneous measurement of bacterial flagellar rotation rate and swimming speed. *Biophys J*, 69:2154–2162, 1995.

[51] Yukio Magariyama, Makoto Ichiba, Kousou Nakata, Kensaku Baba, Toshio Ohtani, Seishi Kudo, and Tomonobu Goto. Difference in bacterial motion between forward and backward swimming caused by the wall effect. *Biophys J*, 88:3648–3658, 2005.

[52] Randall B. Marx and Michael D. Aitken. Bacterial chemotaxis enhances naphthalene degradation in a heterogeneous aqueous system. *Environ Sci Technol*, 34:3379–3383, 2000.

[53] Harley H. McAdams, Balaji Srinivasan, and Adam P. Arkin. The evolution of genetic regulatory systems in bacteria. *Nature Reviews Genetics*, 5:169–178, 2004.

[54] R. Mesibov, G.W. Ordal, and J. Adler. The range of attractant concentrations for bacterial chemotaxis and the threshold and size of response over this range. weber law and related phenomena. *J. Gen. Physiol.*, 62:203–223, 1973.

[55] J.G. Mitchell. The influence of cell size on marine bacterial motility and energetics. *Microb. Ecol.*, 22:227–238, 1991.

[56] H. Naber. Two alternative models for spontaneous flagellar motor switching in halobacterium salinarium. *J. Theor. Biol.*, 181:343–358, 1996.

[57] J.S Parkinson. Complementation analysis and deletion mapping of escherichia coli mutants defective in chemotaxis. *J Bacteriol*, 135:45–53, 1978.

[58] E.M. Purcell. Life at low reynolds number. *Am J Phys*, 45:3–11, 1977.

[59] Hong Qian. Open-system nonequilibrium steady state: Statistical thermodynamics, fluctuations, and chemical oscillations. *J. Phys. Chem. B*, 110:15063–15074, 2006.

[60] J. Saragosti, V. Calvez, N. Bournaveas, B. Perthame, A. Buguin, and P. Silberzan. Directional persistence of chemotactic bacteria in a traveling concentration wave. *Proc Natl Acad Sci USA*, 108:16235–16240, 2011.

[61] Mayukh K. Sarkar, Koushik Paul, and David Blair. Chemotaxis signaling protein chey binds to the rotor protein flin to control the direction of flagellar rotation in escherichia coli. *Proceedings of the National Academy of Sciences*, 107(20):9370–9375, 2010.

[62] Birgit E. Scharf, Karen A. Fahrner, Linda Turner, and Howard C. Berg. Control of direction of flagellar rotation in bacterial chemotaxis. *Proc Natl Acad Sci USA*, 95:201–206, 1998.

[63] M.J. Schnitzer. Theory of continuum random walks and application to chemotaxis. *Phys Rev E*, 48:2553–2568, 1993.

[64] M.J. Schnitzer, S. M. Block, H.C. Berg, and E.M. Purcell. Strategies for chemotaxis. *Symp Soc Gen Microbiol*, 46:15–34, 1990.

[65] J.E. Segall, S. M. Block, and H. C. Berg. Temporal comparison in bacterial chemotaxis. *Proc Natl Acad Sci USA*, 83:8987–8991, 1996.

[66] M. Silverman and M. Simon. Flagellar rotation and the mechanism of bacterial motility. *Nature*, 249:73–74, 1974.

[67] Victor Sourjik. Receptor clustering and signal processing in e. coli chemotaxis. *Trends in Microbiology*, 12:569–576, 2004.

[68] Y. Sowa, H. Hotta, M. Homma, and A. Ishijima. Torque-speed relationship of the na+-driven flagellar motor of vibrio alginolyticus. *J Mol Biol*, 327:1043–1051, 2003.

[69] J L Spudich and D E Koshland. Quantitation of the sensory response in bacterial chemotaxis. *Proc Natl Acad Sci USA*, 72:710–713, 1975.

[70] Roman Stocker, Justin R. Seymour, Azadeh Samadani, Dana E. Hunt, and Martin F. Polz. Rapid chemotactic response enables marine bacteria to exploit ephemeral microscale nutrient patches. *Proc Natl Acad Sci USA*, 105:4209–4214, 2008.

[71] Hendrik Szurmant and George W. Ordal. Diversity in chemotaxis mechanisms among the bacteria and archaea. *Micro Mol Biol Rev*, 68:301–309, 2004.

[72] B.L. Taylor and D.E. Koshland. Reversal of flagellar rotation in monotrichous and peritrichous bacteria: generation of changes in direction. *J Bacteriol*, 119:640–642, 1974.

[73] R. F. Thompson. *Foundations of Physiological Psychology*. Harper and Row, New York, 1967.

[74] Hajime Tokuda, Tatsunosuke Nakamura, and Tsutomu Unemoto. Potassium ion is required for the generation of ph-dependent membrane potential and .delta.ph by the marine bacterium vibrio alginolyticus. *Biochemistry*, 20:4198–4203, 1981.

[75] N. Tsang, R. Macnab, and D.E. Koshland Jr. Common mechanism for repellents and attractants in bacterial chemotaxis. *Science*, 181:60–63, 1973.

[76] Wung-Wai Tso and Julius Adler. Negative chemotaxis in escherichia coli. *Journal of Bacteriology*, 118(2):560–576, 1974.

[77] Y Tu, T S Shimizu, and H C Berg. Modeling the chemotactic response of escherichia coli to time-varying stimuli. *Proc Natl Acad Sci USA*, 105:14855, 2008.

[78] George H. Wadhams and Judith P. Armitage. Making sense of it all: bacterial chemotaxis. *Nat Rev Mol Cell Biol*, 5:1024–1037, 2004.

[79] William B. Whitman, David C. Coleman, and William J. Wiebe. Prokaryotes: The unseen majority. *Proceedings of the National Academy of Sciences*, 95(12):6578–6583, 1998.

[80] Li Xie, Tuba Altindal, Suddhashil Chattopadhyay, and Xiao-Lun Wu. Bacterial flagellum as a propeller and as a rudder for efficient chemotaxis. *Proc Natl Acad Sci USA*, 108:2246–2251, 2011.